Final Technical Report

Project Title: A Systems Approach to Bio-Oil Stabilization

Award Number: DE-FG36-08GO18205

Recipient: Iowa State University, 1138 Pearson Hall, Ames, IA 50011

Project Location(s):

Iowa State University (Campus Locations)
-Black Engineering Building
-Biorenewables Research Laboratory
-Metals Development Building
-Sweeney Hall
Ames, IA 50011

BioCentury Research Farm
1327 U Avenue
Boone, IA 50036

Project Period: 9/30/2008 – 9/30/2011 (Granted 12 month no cost extension)
Date of Report: 12/23/11
Written by: Robert C. Brown and Ryan Smith
Program Manager: Robert C. Brown
Principal Investigators: Robert C. Brown

Subcontractors:

Cost-Sharing Partners: ConocoPhillips Company

DOE Project Team
DOE-HQ contact: Paul Grabowski
DOE Field Project Officer: Renae Binstock
DOE Contract Specialist: Melissa Wise
DOE Project Engineer: Trevor Smith

Acknowledgment: This material is based upon work supported by the Department of Energy under Award Number DE-FG36-08GO18205.

A Systems Approach to Bio-Oil Stabilization

Final Scientific/Technical Report

Iowa State University

Table of Contents

Project Information

Project Title: A Systems Approach to Bio-Oil Stabilization
Award Number: DE-FG36-08GO18205
Recipient: Iowa State University, 1138 Pearson Hall, Ames, IA 50011
Principal Investigator: Robert Brown
Cost-Sharing Partner: ConocoPhillips Company

The following report contains business sensitive, proprietary information.

Executive Summary

The objective of this project is to develop practical, cost effective methods for stabilizing biomass-derived fast pyrolysis oil for at least six months of storage under ambient conditions. The U.S. Department of Energy has targeted three strategies for stabilizing bio-oils: (1) reducing the oxygen content of the organic compounds comprising pyrolysis oil; (2) removal of carboxylic acid groups such that the total acid number (TAN) of the pyrolysis oil is dramatically reduced; and (3) reducing the charcoal content, which contains alkali metals known to catalyze reactions that increase the viscosity of bio-oil.

Ash content, more specifically alkali and alkaline earth metals (AAEM), are known to catalyze decomposition reactions of biomass carbohydrates to produce light oxygenates that destabilize the resulting bio-oil as opposed depolymerization of the biomass carbohydrates to anhydrosugars. Methods envisioned to prevent the AAEM from reaction with the biomass carbohydrates include washing the AAEM out of the biomass with water or dilute acid or infusing an acid catalyst to passivate the AAEM.

Micropyrolysis results from washing biomass proved washing to be an effective technique, however the large quantity of water required to wash the feedstock that must then be dried from the feedstock deems the process impractical to be useful on commercial scale.

Infusion of acids into the feedstock to convert all of the AAEM to salts which are stable at pyrolysis temperatures proved to be a much more technoeconomically feasible process. A correlation with an R^2 of greater than 0.99 was found which shows that titrating AAEM in biomass to a thermally stable phosphate or sulfate salt which prevents the AAEM from reacting with the biomass carbohydrates increases the yield of anhydrosugars by greater than 300% while greatly reducing the yield of light oxygenates that are known to destabilize bio-oil. The process proved to be scalable when pyrolysis of the acid infused feedstocks on the 2 kg/hr. auger reactor

led to bio-oil with similar yields as unreacted feedstock, higher anhydrosugar content, lower light oxygenate content, lower water insoluble content, and a lower modified acid number all leading to a bio-oil with superior properties in comparison to the untreated feedstock. The correlation found is easily applied to any feedstock to produce the highest yield of anhydrosugars and superior properties for upgrading to fuels and chemicals.

Particulate matter can interfere with combustion or catalytic processing of either syngas or bio-oil. It also is thought to catalyze the polymerization of bio-oil, which increases the viscosity of bio-oil over time. High temperature bag houses, ceramic candle filters, and moving bed granular filters have been variously suggested for syngas cleaning at elevated temperatures. High temperature filtration of bio-oil vapors has also been suggested by the National Renewable Energy Laboratory although there remain technical challenges to this approach.

The fast pyrolysis of biomass yields three main organic products: condensable vapors, non-condensable gases, and liquid aerosols. Traditionally these are recovered by a spray quencher or a conventional shell and tube condenser. The spray quencher or condenser is typically followed by an electrostatic precipitator to yield 1 or 2 distinct fractions of bio-oil. The pyrolyzer system developed at Iowa State University incorporates a proprietary fractionating condenser train. The fast pyrolysis system is currently configured as shown in Figure 3.1. The system collects the bio-oil into five unique fractions.

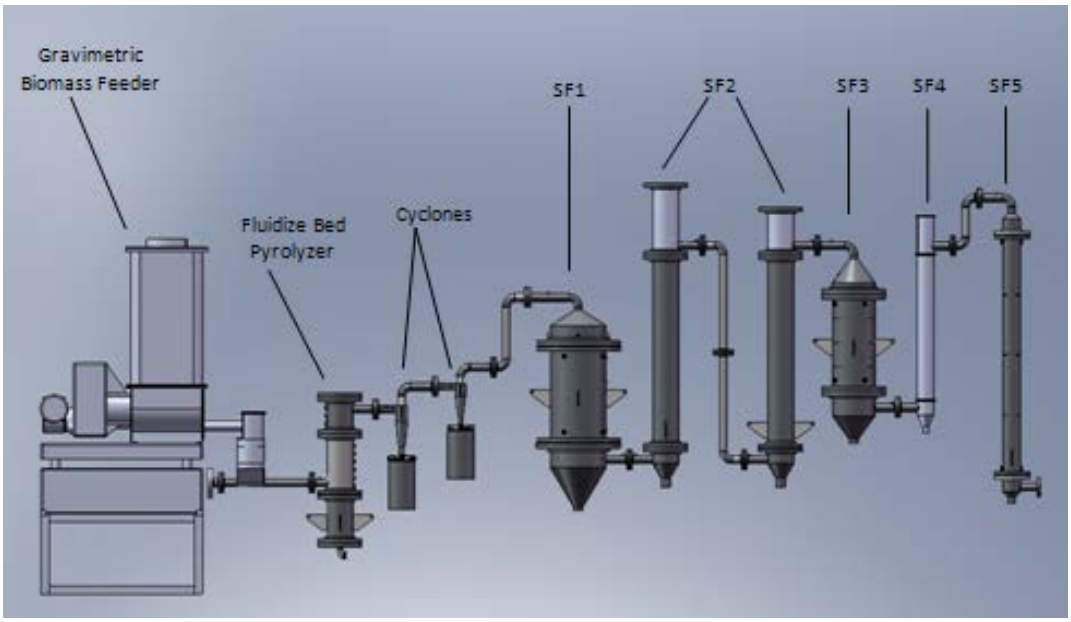

Figure 3.1. Process Development Unit (8 kg/hr) for stable bio-oil production

For conditions typical of fluidized bed pyrolyzers, stage fractions have been collected that are carbohydrate-rich (anhydrosugars), lignin-rich, and an aqueous solution of carboxylic acids and aldehydes. One distinguishing feature of this method is the

production of stage fractions of bio-oil that contain very little water. Another important feature is that most of the water normally found in bio-oil appears in the last stage fraction along with several water-soluble components that are thought to be responsible for bio-oil aging (low molecular weight carboxylic acids and aldehydes). An optimization study has been conducted on this system, and well as miscellaneous upgrades that will improve the repeatability and reliability of the system.

Research work on laser diagnostics for hot-vapor filtration and bio-oil recovery centered on development of analytical techniques for in situ measurements during fast pyrolysis, hot-vapor filtration, and fractionation relative to bio-oil stabilization. The information provided by these techniques is important for understanding the complex, multiphase flow environment consisting of submicron-scale aerosols, micron-scale particulates, and a wide range of condensable and non-condensable vapors. This understanding furthermore enables optimization of filtration and condensation to separate energy-rich hydrocarbons from inorganics and water, thereby improving the storage, handling, and subsequent upgrading of bio-oil to practical transportation fuels. The methods developed in this work include laser-induced breakdown spectroscopy (LIBS), laser-induced incandescence (LII), and laser scattering for elemental analysis (N, O, H, C), detection of particulates, and detection of aerosols, respectively. These techniques were utilized in simulated pyrolysis environments and applied to a small-scale pyrolysis unit. The current report presents an evaluation of these techniques, with LIBS being the most effective techniques for quantitative analysis, and LII and scattering being useful for qualitative imaging. While further work is necessary to characterize performance in large-scale pyrolysis units, the diagnostics developed in this work have been shown to be effective at identifying constituents of pyrolysis during difference phases of bio-oil recovery and differentiating these constituents by their physical and chemical characteristics.

Stability of Bio-oils is adversely affected by the presence of particulates that are formed as a consequence of thermal pyrolysis, improving the CFD simulations of moving bed granular filter (MBGF) is useful for improving the design of MBGF for bio-oil production. However, these CFD calculations cannot resolve the flow past individual-granules and they represent the filter efficiency approximately using mathematical models. Existing models for fine particle filtration are restricted to low speed flows (Stokes regime). The current work uses fully resolved direct numerical simulation (where the flow past each granule is accurately represented) to calculate the filter efficiency that is used in the CFD model at all flow speeds.
This study shows that fully-resolved direct numerical simulation (DNS) is successful in calculating the filter efficiency at all speeds. The data from this simulation effort is used to develop a filter efficiency model that is valid at all speeds. Beyond the direct benefit to improved production of stable bio-oil. The development of advanced simulation capabilities has a broad impact on several related problems such as:

- In thermal power plants: Deposition of particulate on heat exchangers and exhaust emission filtration;
- Chemical looping combustion;
- Water filtration.

Aldehydes and acids are thought to play key roles in the stability of bio-oils, so the catalytic stabilization of bio-oils (Task 6) was focused on whether a reaction approach could be employed that simultaneously addressed these two types of molecules in bio-oil. Our approach to post treatment was simultaneous hydrogenation and esterification using bifunctional metal/acidic heterogeneous catalyst in which reactive aldehydes were reduced to alcohols, creating a high enough alcohol concentration so that the carboxylic acids could be esterified. While we demonstrated that this combined reaction was feasible, we were not able to identify a bifunctional catalyst with sufficient activity for accomplishing the conversion at an acceptable reaction temperature.

Comparison of Accomplishments with Project Objectives

The goal of this project set forth by the DOE guidelines was to develop practical and cost effective methods for stabilizing biomass-derived fast pyrolysis oil for at least six months of storage under ambient conditions. Many of the stability issues come from phase separation of bio-oil, reactions of carboxylic acids and aldehydes leading to polymerization and water formation, and reduction of char and alkali/alkaline earth metal (AAEM) content that is thought to catalyze secondary reactions that lead to the unstable bio-oil products.

The goal of this project set forth by the DOE guidelines was to develop practical and cost effective methods for stabilizing biomass-derived fast pyrolysis oil for at least six months of storage under ambient conditions. Many of the stability issues come from phase separation of bio-oil, reactions of carboxylic acids and aldehydes leading to polymerization and water formation, and reduction of char and alkali/alkaline earth metal (AAEM) content that is thought to catalyze secondary reactions that lead to the unstable bio-oil products.

Methods envisioned for pretreatment included: water wash to remove AAEM, dilute acid wash also to remove AAEM content, and infusion of a homogeneous acid catalyst which is thought to encourage cellulose depolymerization to anhydrosugars rather than decomposition to light oxygenated species.

Three feedstocks including red oak, switchgrass, and cornstover were chosen to be used for experiments due to their variety of cellulose, hemicellulose, lignin, and ash contents to cover a vast array of feedstock properties to experiment with.

Approaches outlined were to test pretreated biomass with the Micropyrolyzer/GC/MS to down select the best pretreatments followed by trials in a bench scale fluidized bed reactor to confirm the pretreatment is scalable.

All three pretreatment approaches were tested over the course of funding. Water wash and dilute acid wash were shown to increase stability of the bio-oil somewhat however were deemed impractical due to the large volume of water required to wash the AAEM from the biomass and then be dried from the biomass. The acid infusion pretreatment was shown to dramatically improve the yield of anhydrosugars from cellulose thus decreasing the yield of carboxylic acids and aldehydes which are known lead to instabilities in the bio-oil. Little water was needed to infuse the acid, thus little drying was required. Phosphoric and sulfuric acids were found to give the best results and an equation with a correlation with an R^2 of 0.99 was developed to determine the amount of acid that must be infused into any feedstock. The amount of acid needed for the infusion was found to be just enough to convert all of the AAEM in the biomass to a thermally stable salt that will not decompose at pyrolysis temperatures, i.e. phosphates or sulfates.

The original guiding hypothesis for Task #2 of the project was that the removal of particulate matter from bio-oil precursors through hot gas filtration will reduce percent solids in the resulting bio-oil and produce a product with increased stability. Through the work detailed below, it was determined that he moving bed granular filter (MBGF) was able to remove primary charcoal entrained in the pyrolysis product stream. However, due to the complexity of the system, a full mass balance on outgoing particulate was not completed and therefore quantitative reduction in percent solids could not be assessed. Accelerated aging trials of the resulting bio-oil concluded the particulate removal did not reduce aging of the oil due to the confirmed entrainment and subsequent collection of filtration media derived “rock dust” which is high in alkali content. The entrainment of the “rock dust” can be corrected with a simple geometry change to the exit area of the filter resulting in lower face velocities and reduced tendency to carry dust. Additional alternatives include changes to the filtration media used such as the transition to a less frangible media that would eliminate dust creation or to an inert media that did not contain the alkali metal contamination. Implementation of one or more of these solutions would result in the ability to quantify reduction in bio-oil solids content through traditional mass measuring techniques or the ability to quantify changes in aging effects due to reduced bio-oil alkali content.

The objective of Task #3 was to produce a stable bio-oil through fractionation. As described in the executive summary, a proprietary bio-oil fractionation system was used to separate the carboxylic acids, aldehydes, and water from the rest of the bio-oil, thereby producing a more stable bio-oil.

Two sub-tasks were originally highlighted for Task #3. The first sub-task, 3a, was to perform fractionating condenser trials with biomass specified by the DOE. The specified biomass was to be pyrolyzed in order to generate bio-oil samples needed to optimize the pyrolyzer and fractionating condenser operating parameters for maximum bio-oil stability. The second sub-task, 3b, was to perform fractionating condenser trials with selected pretreatments. The most promising pretreatments selected from Task 1 were to be used to generate whole fractionated bio-oil samples using a process development fluidized bed pyrolyzer unit at standard conditions of temperature and sweep gas velocities. Two milestones accompanied each sub-task. Milestone I was to identify optimized fast pyrolyzer and fractionating condenser operating conditions. Milestone II was to complete production of bio-oil fractions needed for stability testing.

Task 3a was completed. The bio-oil samples were generated using the specified biomass. Experiments were performed on an 8 kg/hr fast pyrolysis unit coupled with a fractionating condenser train as mentioned above. After construction, an optimization of the system was conducted. The original independent variables included biomass type; biomass particle size and moisture content; ratio of biomass feed rate to fluidizing gas flow rate; pyrolysis temperature; temperature of each condenser tube and voltage applied to each electrostatic precipitator (ESP). The original dependent variables included the amount of bio-oil collected in each condenser and ESP; the water content, particulate matter content, and chemical composition of each bio-oil fraction; and the viscosity of each bio-oil fraction as determined in the aging tests subsequently described. The scope of the optimization study was later changed to study the effect of the reactor temperature on the composition of the bio-oil. During this study, the sweep gas velocity was varied to keep the apparent residence time in the pyrolyzer approximately constant. The dependent variables of the study included: yield of bio-oil, biochar, and non-condensable gases, yield of sugars and carboxylic acids, yield of sugars and phenolic compounds, modified acid number (MAN) of the bio-oil, and moisture content of the bio-oil. The bio-oil was also subjected to accelerated aging tests using the procedure specified by the DOE. The molecular weight of the bio-oil served as the main dependent variable in the aging tests. Task 3b was not completed as planned because the pretreated biomass was not successfully tested on a smaller scale.

The goals of Task 4 were to implement advanced laser diagnostics for in situ characterization of hot vapor filtration and bio-oil recovery, including condensation processes for bio-oil fractionation. The actual accomplishments in this task included demonstrations of several laser-based techniques in small-scale test rigs intended to simulate these environments, including calibration measurements and proof that the different phases can be separated within the pyrolysis products. Experiments in small-scale test rigs were necessary because the pilot-scale pyrolysis facility underwent frequent modification and testing for other tasks and this was not conducive to diagnostics development. Hoswever, insertion rigs were also designed,

constructed, and tested in a preliminary fashion for use within the pilot-scale pyrolysis system in this task. The laser diagnostic system was proven to be capable of operating in this environment, although further investigation is needed for these techniques to overcome limitations on optical access due to window fouling over time.

Task 5a was to develop a CFD model for the MBGF using FLUENT. A CFD model for 3-D simulation of particle laden gas flow through a packed bed filter using ANSYS-FLUENT was developed. Task 5b was to validate the CFD model against experimental pressure drop and flow rate data. The pressure gradient in the packed bed obtained from the CFD model gave an excellent match with pressure gradient in a packed bed obtained from Ergun's equation (Macdonald, 1979). The amount of char trapped in the filter with time gave an excellent match when compared with experimental data from El-Hedok, 2009. Task 5c was to develop a direct numerical simulation (DNS) char particle tracking code through an array of spheres. Granular filtration of char/fly ash is simulated by Lagrangian tracking of char/fly ash particles in a flow field obtained from direct numerical simulation (DNS) of Navier-Stokes equations governing flow past an assembly of granules. The code developed to simulate granular filtration of char/fly ash particles was validated by comparing the filter efficiency with published empirical correlation (D'Ottavio and Goren 1982). Task 5d was to use DNS to develop a char trapping efficiency model. DNS data was used to understand filtration mechanism of fine particles in a granular bed. DNS code was further extended to filter polydisperse char/fly ash particles in a granular bed (Ravi et al., 2010). Task 5e was to implement the char trapping efficiency model in the CFD model. The CFD model developed using ANSYS-FLUENT was validated by comparing the char accumulation rate with the experimental results with Jung et al. (1989) and Qin (2010) models implemented in the CFD model. Task 5f was to use the CFD model to investigate the MBGF design options for maximizing char removal. Observations of the DNS data showed that filtration rates are different for interfacial and downcomer region, which was also observed by I. El-Hedok (2009). Hence, CFD simulations need to be performed with different filtration rates for interfacial and downcomer region in the granular bed.

Task 6a was to synthesize and characterize bifunctional heterogeneous catalysts: We established an optimized synthesis procedure for making a catalyst with both metal and organosulfonic acid functionalities. As part of optimizing the synthesis procedure, we performed extensive characterization, which allowed us to establish the properties needed to maximize catalyst activity for the one-step hydrogenation/esterification reaction system. Task 6b was to test the bifunctional catalysts with model bio-oil compounds: We tested the reaction performance of mixtures of acetic acid and acetaldehyde and used these results to guide improved catalyst synthesis procedures Task 6c was to determine optimal reaction conditions with model bio-oil and best bifunctional catalysts: We determined appropriate reaction conditions to screen catalyst candidates. These reaction conditions were used

to determine the order in which the metal and organosulfonic acid needed to be introduced in the catalyst synthesis as well as the appropriate way to activate the metal functionality to maximize its hydrogenation activity. Task 6d was to conduct reaction studies with real bio-oil samples produced from Task 3: We did not run reactions with real bio-oil samples as the optimized bifunctional catalyst still required a reaction temperature of >130°C, which was too high for bio-oil stabilization. At this elevated temperature oligomerization occurred in the bio-oil leading to large viscosity increases. Task 6e was to produce sufficient quantities of catalytically treated bio-oils for aging studies: This goal was not accomplished since an adequate catalyst was not identified.

Summary of Project Activities

Task #1: Role of Biomass Pretreatments

Pretreatment of biomass by washing with water and dilute acid as well as infusion of homogeneous acid catalysts has been covered extensively in literature however many of the conclusions were qualitative and offered no clear quantitative conclusions. Several researches have indicated that the ash contained in the biomass, and more specifically the alkali and alkaline earth metals (AAEM) found in the ash, catalyze the decomposition biomass carbohydrates to light oxygenates and water, which are known to destabilize the bio-oil, rather than depolymerization to anhydrosugars. Switchgrass was the first feedstock to be experimented with since its content of AAEM and cellulose/hemicellulose/lignin fall somewhere in the middle of common feedstocks.

The first step was to calibrate the Micropyrolyzer/GC/MS system for compounds commonly found in bio-oil, especially those that are known to effect bio-oil stability. Compounds calibrated for were summarized into several groups including: light oxygenates consisted of hydroxyacetaldehyde, carboxylic acids, aldehydes, and ketones; anhydrosugars consisting of levoglucosan and levoglucosenone; furans, such as furan, furfural, and 5-hydroxymethylfurfural; and phenols, such as phenol, guaiacol, and syringol. Many of several hundred bio-oil compounds could not be calibrated for or could not be detected using GC/MS thus a mass balance on detectable compounds was determined and is indicated as “total” in the figures and tables to follow. Since pyrolysis of switchgrass typically results in bio-oil yields of around 60% and the overall mass balance found from GC/MS detectable compounds during micropyrolysis of switchgrass was found to be anywhere from 15-28%, the GC/MS is accounting for approximately 25-50% of the bio-oil compounds. Bio-oil also typically contains up to 25 % water and up to 25% lignin oligomers, neither of which are detectable by GC/MS, thus the GC/MS method employed accounts for a good portion of the volatile bio-oil compounds.

Water and dilute acid wash were the first pretreatments to be experimented with. A dilute acid wash was prepared by mixing 5wt% acid and 95wt% deionized water. A dilute acid wash to biomass mass ratio of 10:1 was used. The biomass was then washed again with deionized water to remove any remaining acid and was then dried to a consistent moisture content of around 5 wt.% . Figure 1 shows results from micropyrolysis/GC/MS analysis of the washed switchgrass samples.

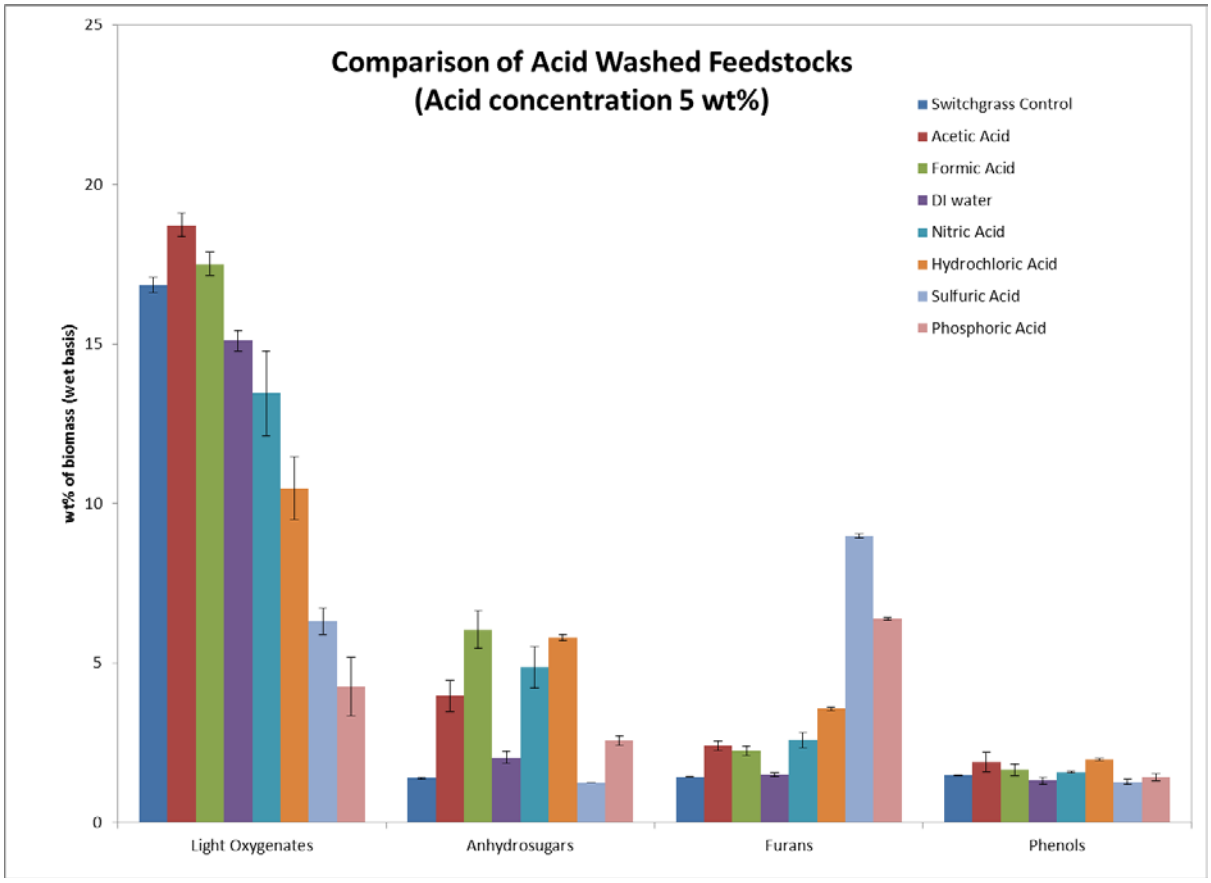

Figure 1: Product distributions from Micropyrolysis/GC/MS of switchgrass washed with deionized water and dilute acid.

As shown in Figure 1, the light oxygenates decreased in overall yield with increasing thermal stability of the anion associated with the acid where sulfuric and phosphoric acids decreased light oxygenates the most, followed by hydrochloric acid, followed by nitric acid and deionized water which had little effect. Acetic and formic acids increased the light oxygenates most likely due to residual acid.

Anhydrosugar yield increased with washing with several of the acids; however no clear correlation could be concluded. Yield of furans increased with stronger acids, which is expected to result from the acid catalyzed dehydration of anhydrosugars. Phenols were not significantly affected by any of the acid washes.

After performing the water and dilute acid washes and gaining perspective on the quantity of water required for the process and the corresponding amount of drying required, we deemed the washing process impractical at a commercial scale and instead focused attention on the acid infusion process.

Acid infusions were performed simultaneous with the acid washes. Since no quantitative conclusions were found in literature on how much acid should be used for infusion, rates of 0-10% mass of acid to mass of dry switchgrass were first tried in attempt to downselect the optimum amount of acid that must be infused. As mentioned above, a decrease in the amount of light oxygenates is thought to coincide with an increase in the yield of anhydrosugars since anhydrosugars result from the depolymerization of cellulose whereas light oxygenates are thought to results from the decomposition of cellulose, thus they come from competing pathways. All acids used for washing experiments were also used for infusions where phosphoric and sulfuric acids proved to work much better in preliminary trials and were therefore used for further testing. Figures 2 and 3 show the results from micropyrolysis of switchgrass infused with varying concentrations of phosphoric and sulfuric acids respectively.

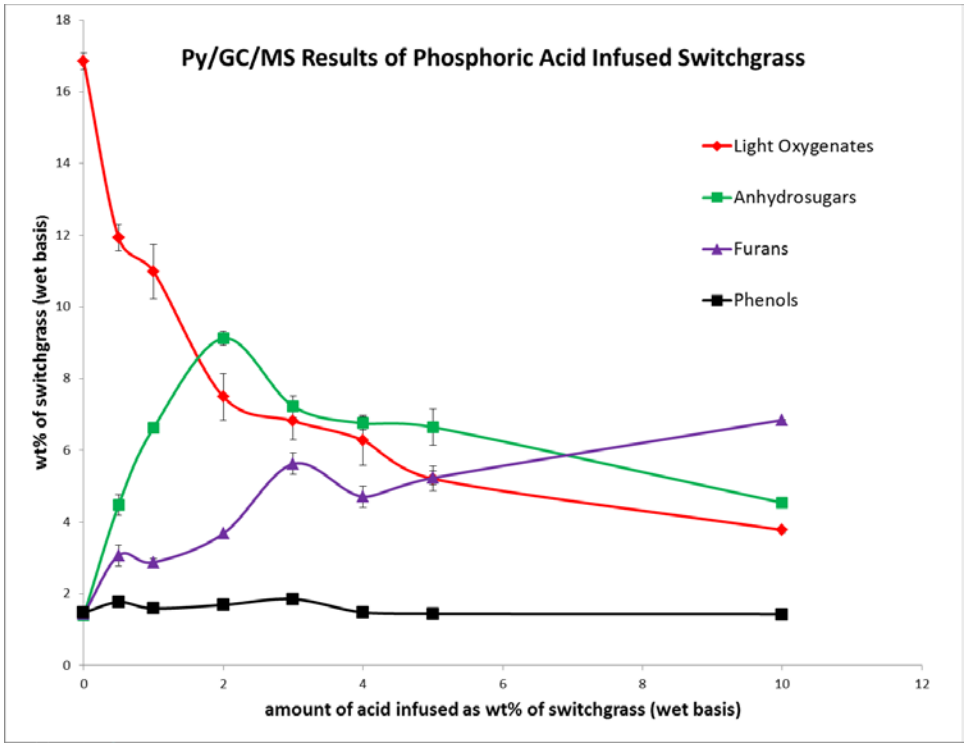

Figure 2: Product distribution from Micropyrolysis/GC/MS of switchgrass infused with varying concentrations of phosphoric acid.

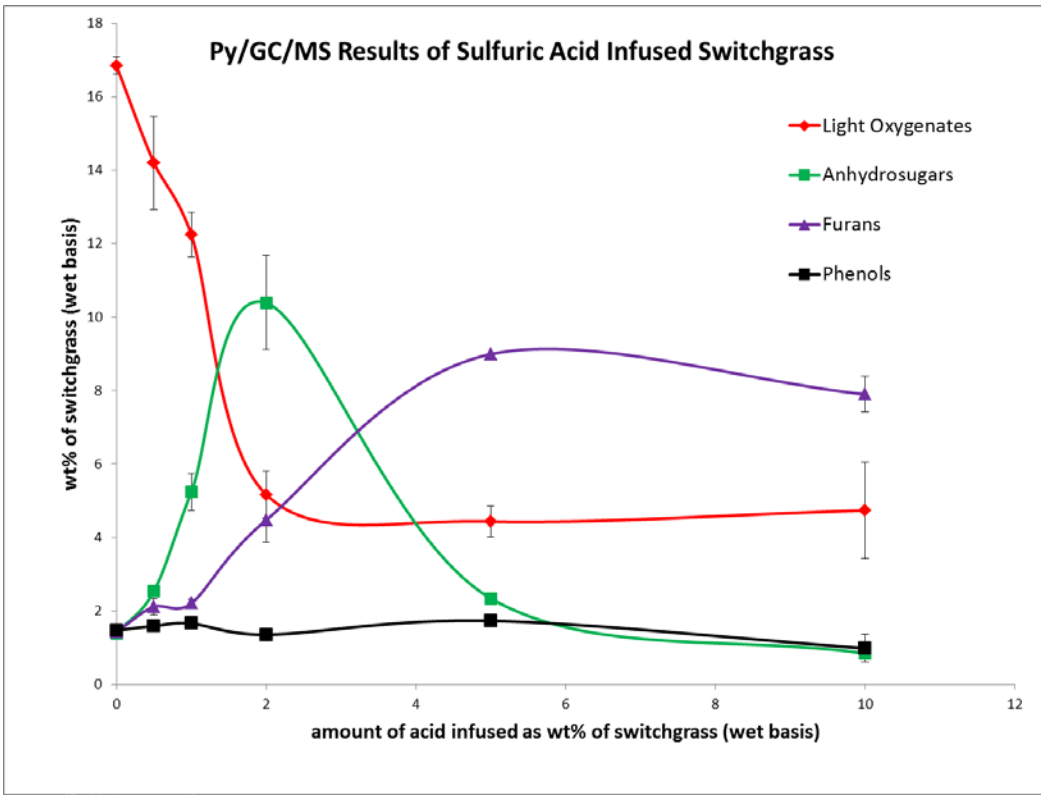

Figure 3: Product distribution from Micropyrolysis/GC/MS of switchgrass infused with varying concentrations of sulfuric acid.

As shown in Figures 2 and 3, a clear peak in anhydrosugar yield occurred with an infusion of 2wt% phosphoric or sulfuric acid where the light oxygenates also showed a drastic decrease. Anhydrosugars were shown to decrease after the peak at 2wt% acid infusion which coincided with an increase in furans which is thought to result from the acid catalyzed dehydration of the carbohydrates. Phenols were minimally affected. The total mass balance is also shown to decrease with increasing acid concentration, which is likely to result from the high acid concentrations leading to more char or non-condensable gases.

Since the 2wt% acid infusion was shown to be optimum, each acid was infused at that rate and the micropyrolysis/GC/MS results are shown in Figure 4.

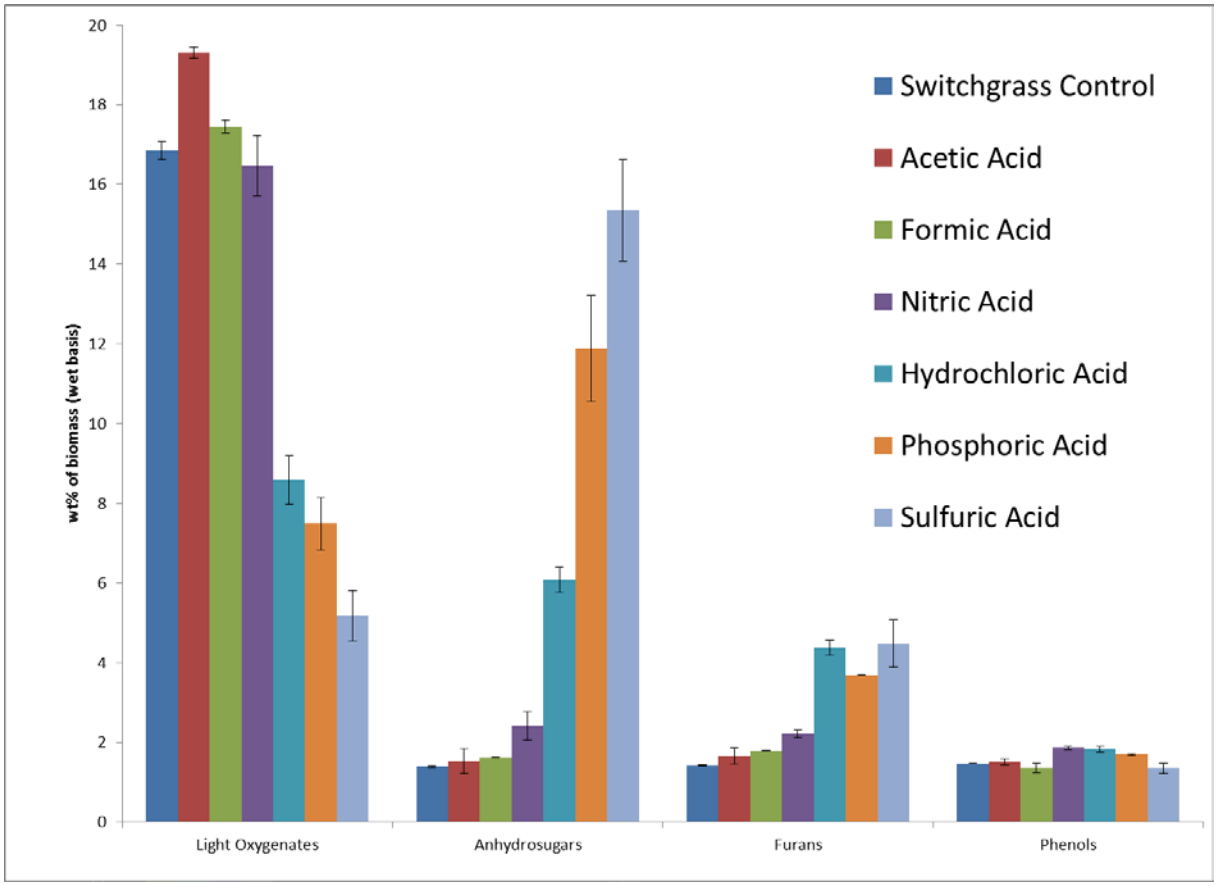

Figure 4: Product distribution from Micropyrolysis/GC/MS of switchgrass infused with various acids.

As mentioned above, phosphoric and sulfuric acids were proven to work best in decreasing light oxygenates and increasing anhydrosugars. Thermally stable anions were then hypothesized to passivate AAEM in the biomass leading to the increase in anhydrosugars where sulfates, phosphates and chlorides were thought to bind up the AAEM and prevent it from reacting with the carbhydrates during pyrolysis, whereas the nitrates, formates, and acetates are thought to decompose during pyrolysis leading to an active form of AAEM that catalyzes the decomposition of biomass carbohydrates. Although the chlorides are thermally stable at pyrolysis temperatures they didn't have as significant of an effect on passivating the AAEM as the phosphates and sulfates, which is thought to come from steric hinderance effects where the sulfate and phosphate anions are much larger than the chloride anion and engulf the AAEM cation, preventing it from reacting during pyrolysis. The much smaller chloride anion leaves more surface area for the AAEM to react with the biomass carbohydrates although the salt itself is stable.

Sulfuric and phosphoric acids were shown to lead to the greatest increase in anhydosugars and greatest decrease in light oxygenates, thus were used for further optimization of the acid infusion pretreatment process. A 2wt% acid to biomass ratio was found to work best for switchgrass, however the next step was to determine if a similar ratio would apply to other feedstocks with different AAEM concentrations.

The peak in anhydosugar yield from other feedstocks were found to occur at different acid to biomass ratios. Concentration of moles of valence charge, where alkali metals such as potassium and sodium have one valence charge per mole and alkaline earth metals such as magnesium and calcium have two valence charges per mole, resulting from AAEM found in each biomass type were plotted against moles valence charge from the acid used for pretreatment, where an acid such as sulfuric acid would have two valence charges per mole and an acid such as nitric acid would have one valence charge per mole. Figure 5 shows results from correlations found.

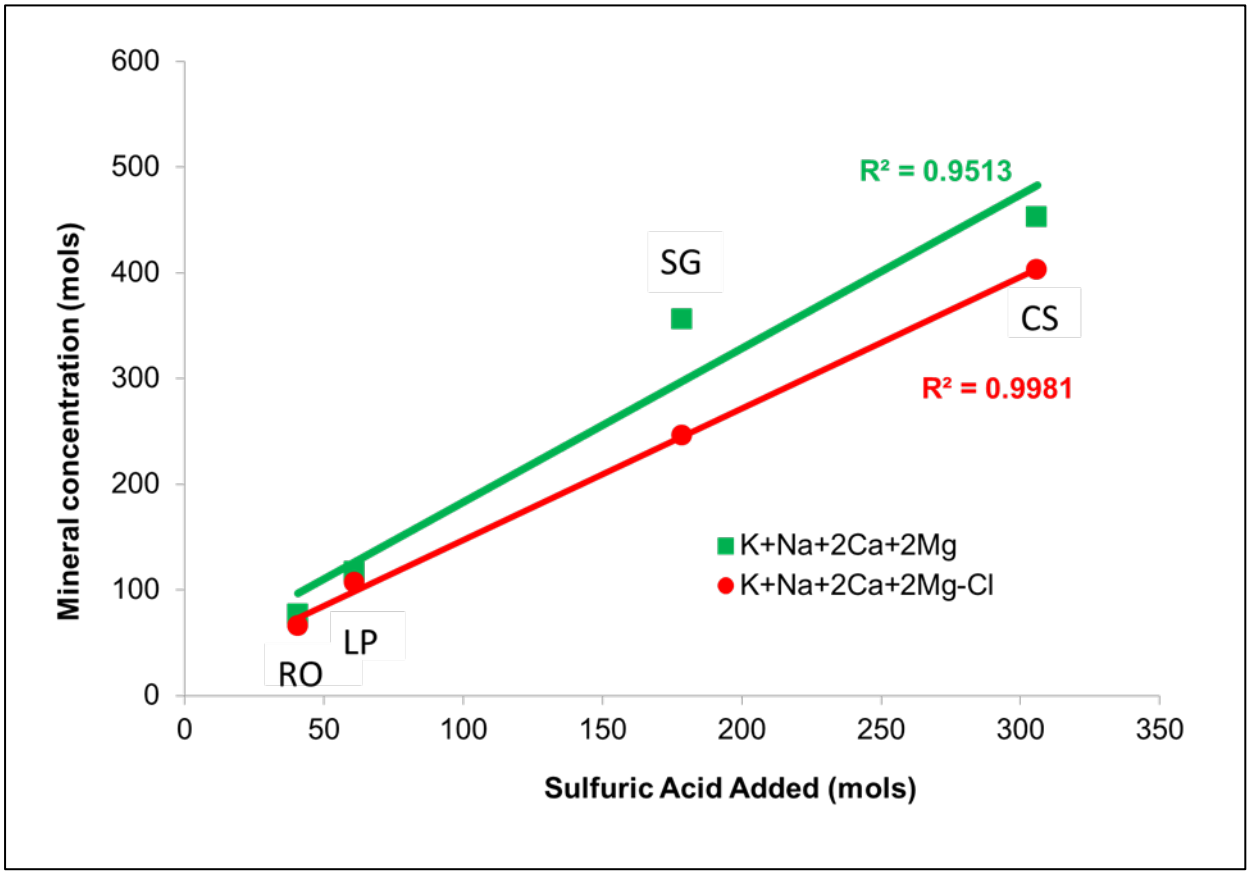

Figure 5: Correlation of valence charge from alkali and alkaline earth metals found in biomass to the overall valence of acid needed to achieve maximum potential yield of levoglucosan from biomass pyrolysis.

As shown in Figure 5, by plotting the moles of sulfuric acid valence charge vs. the moles of AAEM valence charge a correlation with an R^2 of 0.9513 resulted indicating strong correlation between the AAEM valence and amount of acid needed. The AAEM already bound with a chloride anion is not expected to convert to a sulfate or phosphate based on equilibrium calculations thus the valence of chloride anion found in each of the feedstocks was subtracted from the valence of AAEM since it would not be converted and a correlation with an R^2 of 0.9981 was found in that case indication a very strong correlation. The correlation found was also proven to work for a variety of feedstocks with a variety of AAEM concentrations, thus this

correlation can be applied to any cellulosic biomass feedstock to produce the highest yield of anhydrosugars and lowest yield of light oxygenates.

Although the highest yield of anhydrosugars was found from each feedstock it was also important to find how this yield compared to the maximum potential yield of anhydrosugars from the feedstock. Micropyrolysis of pure cellulose and pure hemicellulose were found to produce 57wt% and 5wt% anhydrosugars respectively, thus these values were used with the compositional analysis of the feedstock to determine the percentage of the potential yield that was achieved with the pretreatment process. Table 1 summarizes results from pretreatment of switchgrass, cornstover, red oak, and loblolly pine with the optimum amount of sulfuric and phosphoric acids found with the correlation found in Figure 5.

Table 1: Comparison of acid infusion levels that yield maximum levoglucosan production from various feedstocks.

Feedstock	Composition		LG Yield after Acid Infusion (wt%)		Potential LG Yield (wt%)	% of Potential Yield Phosphoric Acid Infused		% of Potential Yield Sulfuric Acid Infused	
	Cellulose	Hemicellulose	Phosphoric	Sulfuric		Mean	Std Dev	Mean	Std Dev
Switchgrass	33.3	35.3	11.9	15.4	20.7	**64.5**	1.7	**83.4**	2.0
Corn Stover	28.9	39.3	9.0	17.9	18.4	**43.4**	1.9	**86.3**	7.2
Red Oak	41.0	31.8	19.1	23.4	25.0	**76.6**	4.8	**94.0**	3.6
Loblolly Pine	32.1	42.7	15.6	19.6	20.4	**79.6**	4.3	**99.7**	8.8

As shown in Figure 5, sulfuric acid infusion lead to highest potential maximum yield from each of the feedstocks achieving 100% of the maximum potential yield from loblolly pine and high potential yield from the other three feedstocks as well.

The correlations worked great on micropyrolysis trials, however to prove scalability of the concept the correlations had to be tested on the bench scale pyrolyzer. A 100 gram per hour fluidized bed reactor was first used to attempt scaled trials of pretreated biomass. Several kilograms of switchgrass and red oak were pretreated with the optimum amount of acid found by the correlation. The concentrated acid was diluted with deionized water where just enough water was used to ensure all of the biomass was dampened to ensure homogeneous mixing, however the water was limited to prevent the need for a lot of drying. Trials on the fluidized bed reactor started out favorably producing a significant quantity of bio-oil; however the rate at which bio-oil accumulated in the collection bottles gradually slowed down and eventually nearly stopped although the biomass continued to feed. Upon examination of the system after cool down a vitreous agglomerated char was found in the fluidized bed that was not able to escape the reactor as shown in Figure 6.

Figure 6: Char resulting from pyrolysis of red oak infused with 0.4wt% sulfuric acid.

As shown in Figure 6, the resulting char appeared as if it was molten at one time and tended to agglomerate the sand from the fluidized bed as well. This char is expected to be resulting from molten lignin and polymerized carbohydrates that are released during pyrolysis. Lignin pyrolysis is thought to be negatively affected by the thermally stable salts resulting from the pretreatment process where the lignin pyrolysis may have been catalyzed by the active AAEM resulting in the release of lignin monomers that are unable to depolymerize without the active AAEM leading to build up of lignin oligomers in the reactor. The dramatic increase in anhydrosugars is also expected to lower their dew point preventing all of them from vaporizing and leaving the reactor. Anhydrosugars are known to polymerize at temperatures above 200 C to oligomers with no vapor pressure that are unable to escape the reactor and instead accumulate in the reactor and dehydrate to form char.

The stationary bed in the fluidized bed reactor and the charring of the pretreated biomass lead agglomeration of the sand bed, thus the fluidized bed reactor couldn't be run continuously to get an accurate mass balance from pyrolysis of the pretreated feedstock. The auger reactor was chosen to be used for additional trials since the bed in the auger rector is continuously being renewed and the bed agglomeration would not be a problem. The results from analysis of bio-oil resulting from pyrolysis of the acid infused feedstock on the auger reactor are shown in Table 2 below.

Table 2: Summary of bio-oil analyses performed on feedstocks infused with acid for the maximum levoglucosan yield.

Sample	Average Bio-oil Yield (wt% wet basis)	Sugar Yield (wt% of dry biomass)	Bio-oil Sugar Concentration (wt% of bio-oil wet basis)	Moisture Content (wt% of bio-oil wet basis)	Water Insoluble Content (wt% of bio-oil wet basis)	Modified Acid Number (MAN)
Red Oak Control	67.0%	5.0%	7.4%	28.8%	12.7%	91
Red Oak - 0.4% H2SO4	65.8%	16.9%	25.7%	28.7%	10.8%	71
Switchgrass Control	61.1%	2.9%	4.4%	36.0%	14.1%	87
Switchgrass - 2.0% H2SO4	58.9%	10.0%	16.0%	39.0%	10.0%	77
Switchgrass - 2.0% H3PO4	62.3%	6.3%	9.3%	35.0%	13.8%	92

As shown in Table 2, bio-oil yields from acid infused feedstocks were comparable to yields from the control feedstock. Sugar yields were increased by over 300% in several cases and moisture content remained approximately constant. The water

insoluble content decreased slightly in the pretreated feedstocks which is expected to result from less depolymerization of lignin leading to a higher char yield, however difficulty in separating char from heat carrier on the auger reactor prevented calculation of an accurate char yield. The modified acid number (MAN) was shown to decrease slightly with sulfuric acid infusion. Many of the reactions occurring during the aging of bio-oil are expected to be acid catalyzed (reference), thus a reduction in the MAN should lead to a more stable bio-oil.

In conclusion washing biomass with water or dilute acid can lead to increased yield of anhydrosugars at the expense of light oxygenates, thus producing a more stable bio-oil, however the washing process was deemed impractical due to the large volume of water required to wash the biomass and the corresponding amount of water that must be dried from the biomass. The drying process is energy intensive and would very negatively affect the economics of the process.

Converting all of the AAEM in the biomass to a thermally stable salt such as phosphate or sulfate by infusing phosphoric or sulfuric acid was found to significantly increase the yield of anhydrosugars and decrease the yield of light oxygenates, thus leading to a more stable bio-oil due the decrease of light oxygenates. A correlation with an R^2 of greater than 0.99 was obtained suitable for determining the amount of acid needed for any cellulosic biomass feedstock. The minimal amount of water, thus drying, required with the acid infusion process leads it to be the most promising method for producing a bio-oil with high concentrations of sugars and much higher stability.

Task #2: Hot Vapor Filtering of Particulate Matter

After extensive preliminary testing and design, the MBGF PDU moved from concept to reality in the construction phase of the project. Design features included roll away filtration assembly for easy servicing, second level access for feed access, provisions for continuous operation, full instrumentation, detailed control system and hardware for significant automation of the process. The finished PDU is depicted in Figure 7.

Figure 7: Moving Bed Granule Filter Process Development Unit

The following paragraphs detail the analysis of products generated during testing performed with the MBGF PDU under pyrolysis conditions.

Mass Balance

Table 3 contains mass data for all of the tests performed including bio-oil yields, char yields, and mass closure information. Good mass closures were obtained for the system, resulting in an overall mass closure of 99% ± 4% as calculated using a 95% confidence interval overall all of the testing data. Bio-oil yield data is very similar with and without the use of the filter; statistical analysis will be performed to see if a significant difference between yields can be detected. The major anomaly present in the yield data occurs with the cyclone collected char. Steady-state pyrolyzer conditions yielded between 16 and 25% while MBGF operation yielded between 13 and 18% by mass. A majority of this difference in collection can be attributed to the elutriation of the fluid bed material into the cyclone collectors. The PDU tends to elutriate material until the expanded bed height is short enough to reside under the reactor exit, a process which takes several hours. Since the steady-state oil is collected near the beginning of the test day (approximately 30 minutes after operating temperatures are reached) and the MBGF steady-state oil is collected at the end of the test (between 2.5 and 5 hours into the test) the fluid bed has most likely stopped elutriating material during MBGF oil collection, accounting for the mass difference.

In order to keep operating conditions the same, the fluid bed material was topped off between tests for consistency.

Table 3: Mass Balance Data for Baseline Operation (PDU S.S.) without MBGF and with MBGF at 3 Granule Flow Rates

Test #	Cyclone Char	Filter Char	SF1	SF2	SF3	SF4	SF5	NCG	Closure
1-20101026 PDU SS	24.5%	N/A	12.5%	19.3%	4.3%	1.4%	25.6%	18.3%	105.9%
1-20110210 PDU SS	16.4%	N/A	12.3%	21.3%	3.6%	1.8%	26.8%	22.8%	104.9%
Average	20.5%	N/A	12.4%	20.3%	3.9%	1.6%	26.2%	20.5%	105.4%
1-20110120 GR8	13.5%	0.9%	10.9%	18.5%	3.8%	1.7%	23.0%	20.9%	93.3%
1-20110202 GR8	13.8%	0.7%	10.6%	17.7%	3.8%	1.8%	26.3%	22.2%	96.8%
Average	13.7%	0.8%	10.8%	18.1%	3.8%	1.8%	24.7%	21.5%	95.1%
1-20110124 GR16	15.6%	1.2%	10.7%	17.0%	3.7%	1.8%	27.1%	22.5%	99.7%
1-20220127 GR16	13.1%	1.1%	9.2%	16.9%	3.9%	1.7%	25.4%	21.5%	92.9%
1-20110221 GR16	13.3%	1.0%	9.3%	16.4%	3.3%	1.6%	28.4%	24.0%	96.3%
Average	14.0%	1.1%	9.7%	16.7%	3.6%	1.7%	27.0%	22.7%	96.3%
1-20101210 GR24	17.6%	0.8%	11.7%	19.2%	3.3%	1.6%	28.2%	22.6%	105.0%
1-20110204 GR24	14.4%	1.9%	10.8%	17.0%	3.2%	1.6%	26.7%	24.2%	99.8%
Average	16.0%	1.3%	11.2%	18.1%	3.3%	1.6%	27.5%	23.4%	102.4%

Moisture Content

The moisture content measurement was replicated between 4-6 times for each fraction in order to obtain statistically significant results. The following model was used to estimate the mean and standard error of the collected data:

Equation 1: Statistic Model

$$y_{ijk} = \mu_k + r_i + \varepsilon_{ijk}$$

where y_{ijk} is equal to the mean of analysis j, on run i, under condition k. The actual mean of the sample is defined as μk. The error between replicated runs is designated as ri while the analytical error between individual measurements is designated as ε_{ijk}; the combination of these two error sources is defined as the standard error. The statistical analysis was conducted using SAS JMP™ software. The upper and lower 95% confidence intervals are then calculated according to the following pair of equations:

Equation 2: 95% Confidence Limits

$$Upper\ 95\%\ Limit = \mu_k + (Standard\ Error)(1.96)$$
$$Lower\ 95\%\ Limit = \mu_k - (Standard\ Error)(1.96)$$

The resulting means and confidence limits shown as error bars are displayed in Figure 8. A general trend of increasing moisture content with decreasing condenser temperatures is apparent and is consistent with previous results from Sherwood-

Pollard.[1] However, no significant conclusions are apparent when comparing the baseline PDU moisture contents with that of any of the MBGF operating conditions.

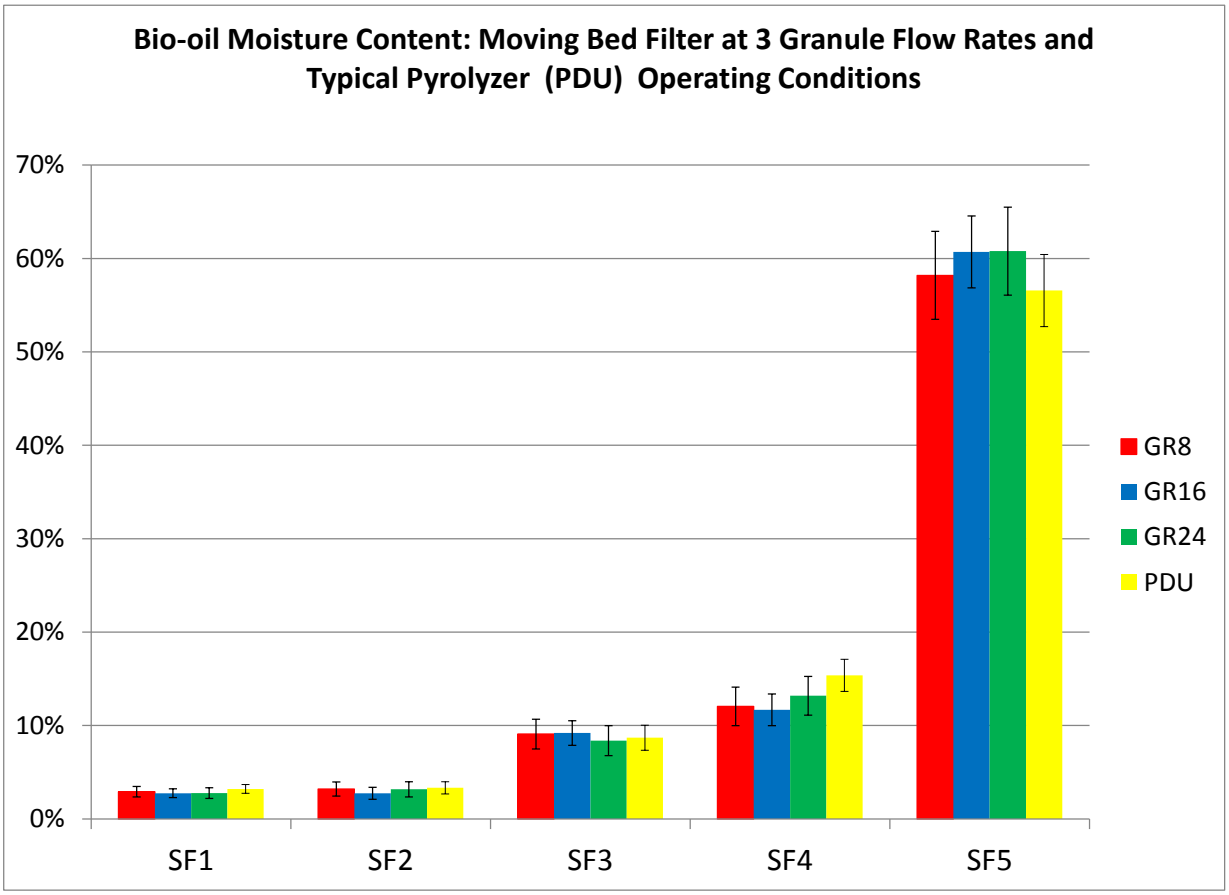

Figure 8: Bio-oil Moisture Content

The moisture content was mass averaged by fraction yield and compared on a whole oil basis using Equation 3. Figure 9 shows that the PDU baseline case produced bio-oil with a moisture content typically found with whole oil. However, when modifying the process with the MBGF in situ, the resulting bio-oil moisture content increased by 2-5% depending on filter operating conditions. The majority of these increases took place in SF5 with the moisture content of the first four fractions remaining relatively constant.

Equation 3: Mass Averaged Moisture Content

$$\left(\frac{\%moisture}{100\%}\right)\left(\frac{g\ H_2O}{g\ \ Bio-oil}\right)\left(\frac{g\ Bio-oil}{g\ Whole\ Bio-oil}\right)$$

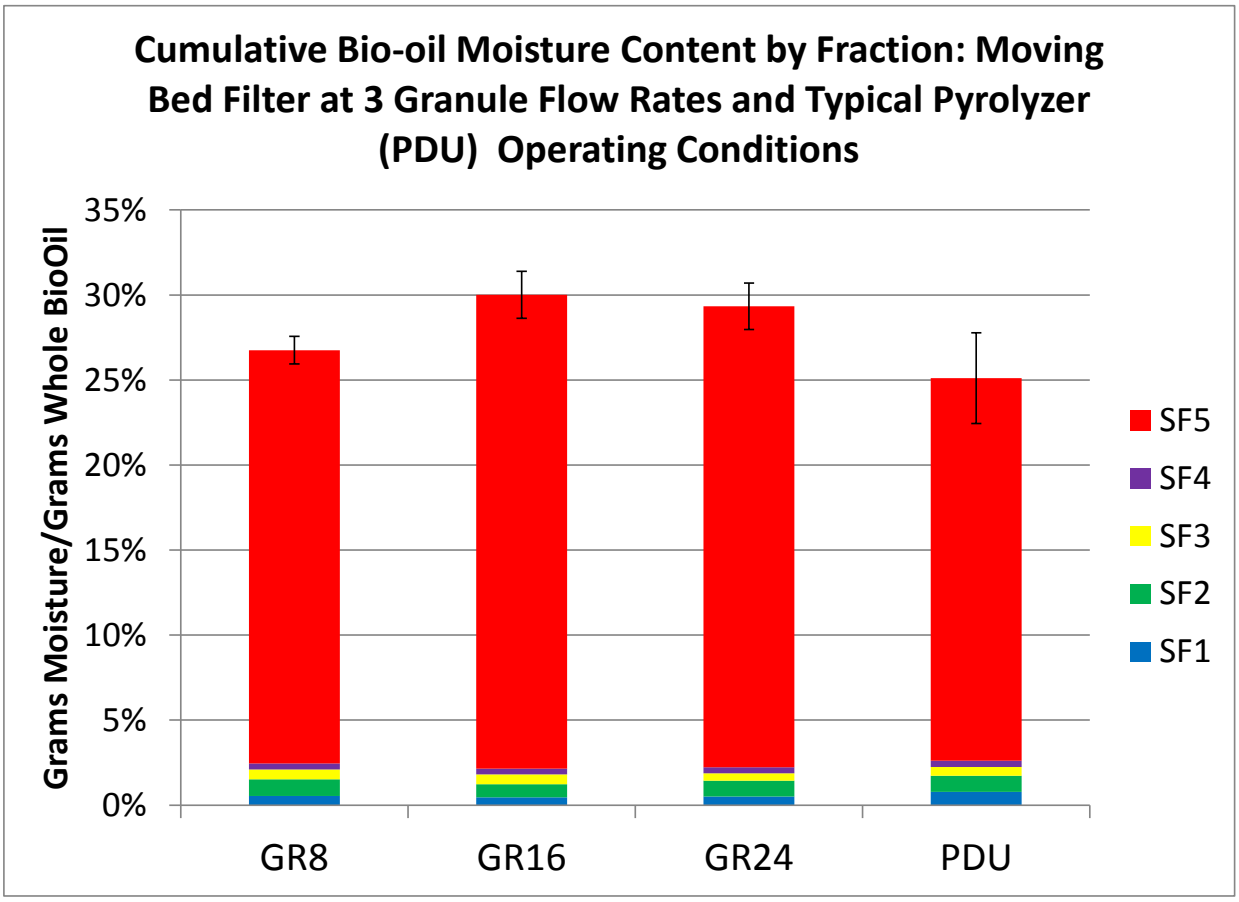

Figure 9: Mass Averaged Moisture Content

The increase in moisture content of MBGF derived bio-oils over baseline samples is a clear indication of the occurrence of secondary reactions within the filter. The 8 kg/h test resulted in a smaller increase in moisture content than either of higher flow rate tests. This operating condition is characterized by longer residence time of collected char in the filter due to the slower granule throughput. Both the 16 and 24 kg/h tests resulted in similar increases in water content over baseline oil. These operating conditions are characterized by shorter char residence time in the filter but with increased surface area for cracking to take place.

Water Insoluble Content

A similar statistical model was applied to the water insoluble content data resulting in the error bars associated with Figure 10. A general trend of decreasing water insoluble content with decreasing stage fraction collection temperature is observed and consistent with Sherwood-Pollard's previous results. However, an interesting trend is present within the insoluble data. Operating the MBGF at granule flow rates of 8 and 24 kg/h resulted in similar bio-oil water insoluble content in the first two fractions, while operation at 16 kg/h and baseline PDU conditions yielded as much as 10% higher water insoluble content. This phenomenon may indicate an optimum MBGF operating condition if the primary goal is to maintain similar water insoluble content as baseline pyrolysis. Although less pronounced, the mass averaged water insoluble

content shown in Figure 11 displays a similar trend. The water insoluble content of the bio-oil under each operating condition amounted to approximately 20% of total bio-oil yield, which is similar to previously reported results by Sherwood-Pollard.

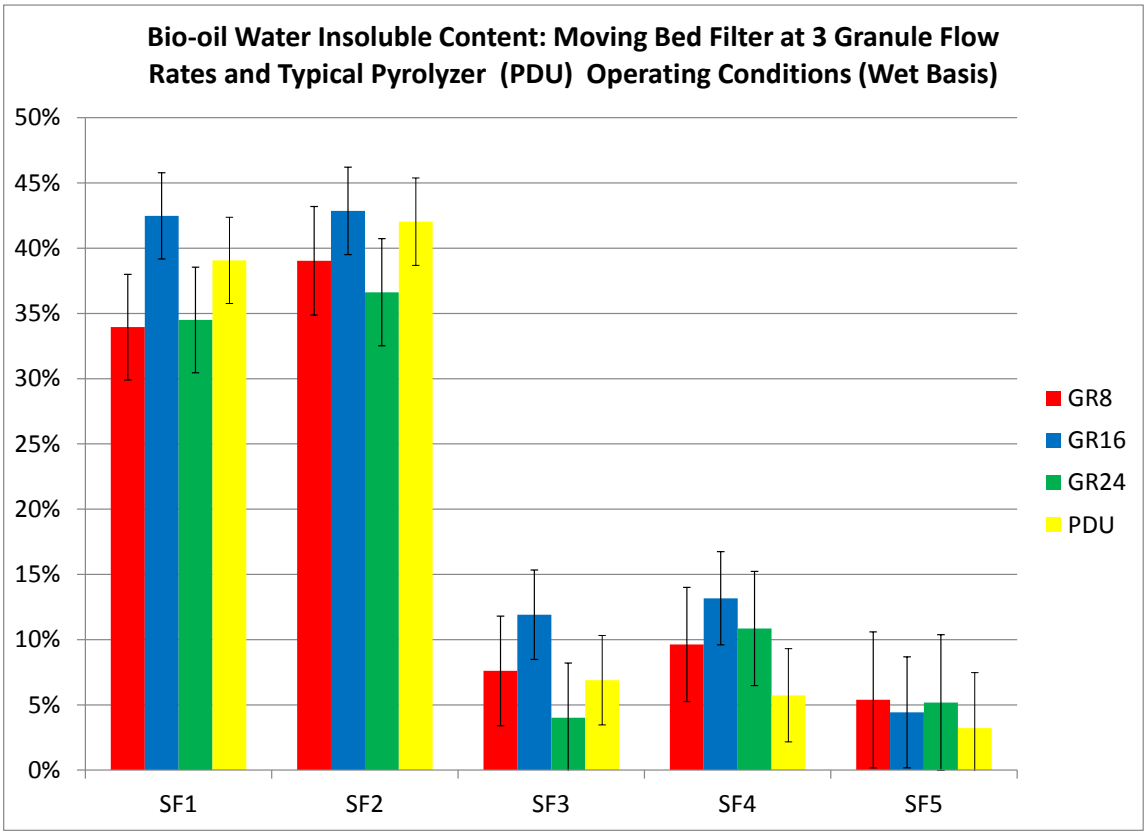

Figure 10: Bio-oil Water Insoluble Content (Wet Basis)

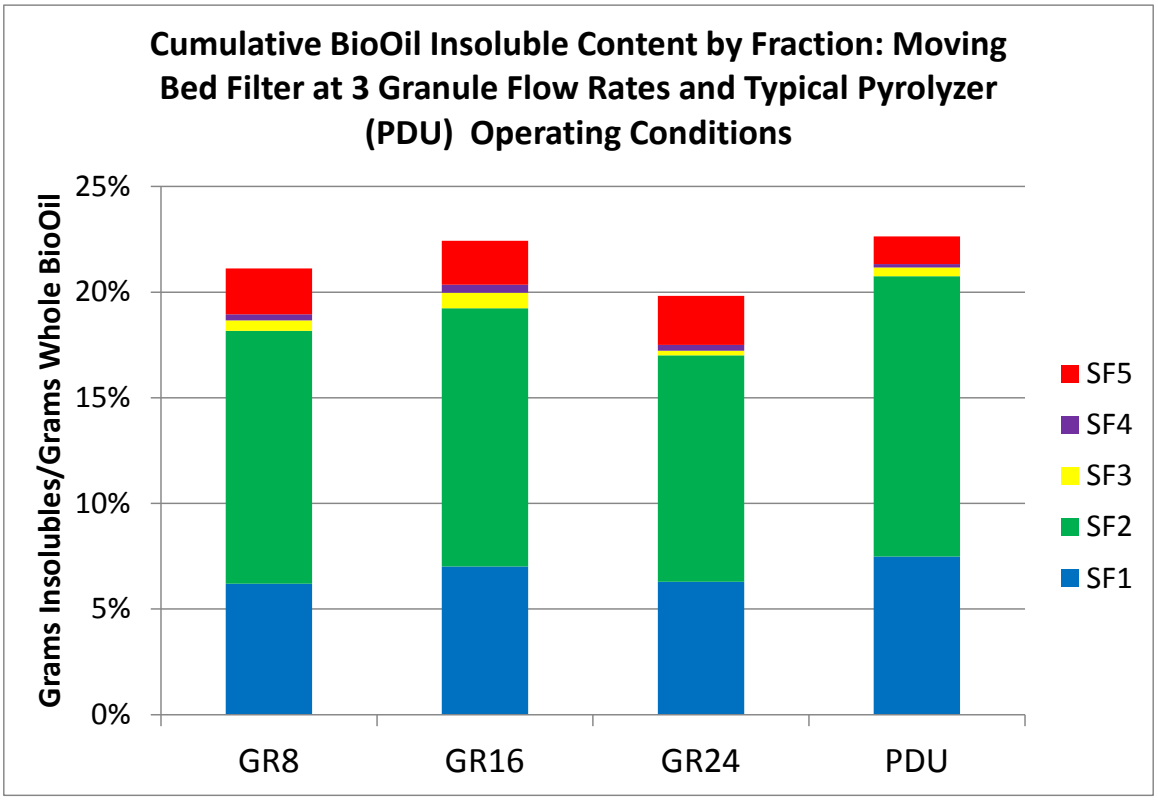

Figure 11: Mass Averaged Bio-oil Water Insoluble Content (Wet Basis)

Solids Content

In order to improve upon results garnered by previous bio-oil solids content methodology, a new method was developed that utilized the fresh collection of samples directly from the PDU and larger sample volumes. The results of the new method can be found in Figure 12. Unfortunately, the error bars associated with this data are very large in some cases. This can be attributed to several causes. It is possible that some of the water insoluble fraction is not dissolved using this technique, with polymers too large to pass through the filter paper and thus would be counted as solids content. It is also very likely, judging by further examination of the solids content, that filtration media is elutriating from the filter bed and collecting in the first stage fraction bio-oil. If the latter is correct, the elutriation process could be very sporadic in the amount of mass it could transfer to the oil, skewing solids content results.

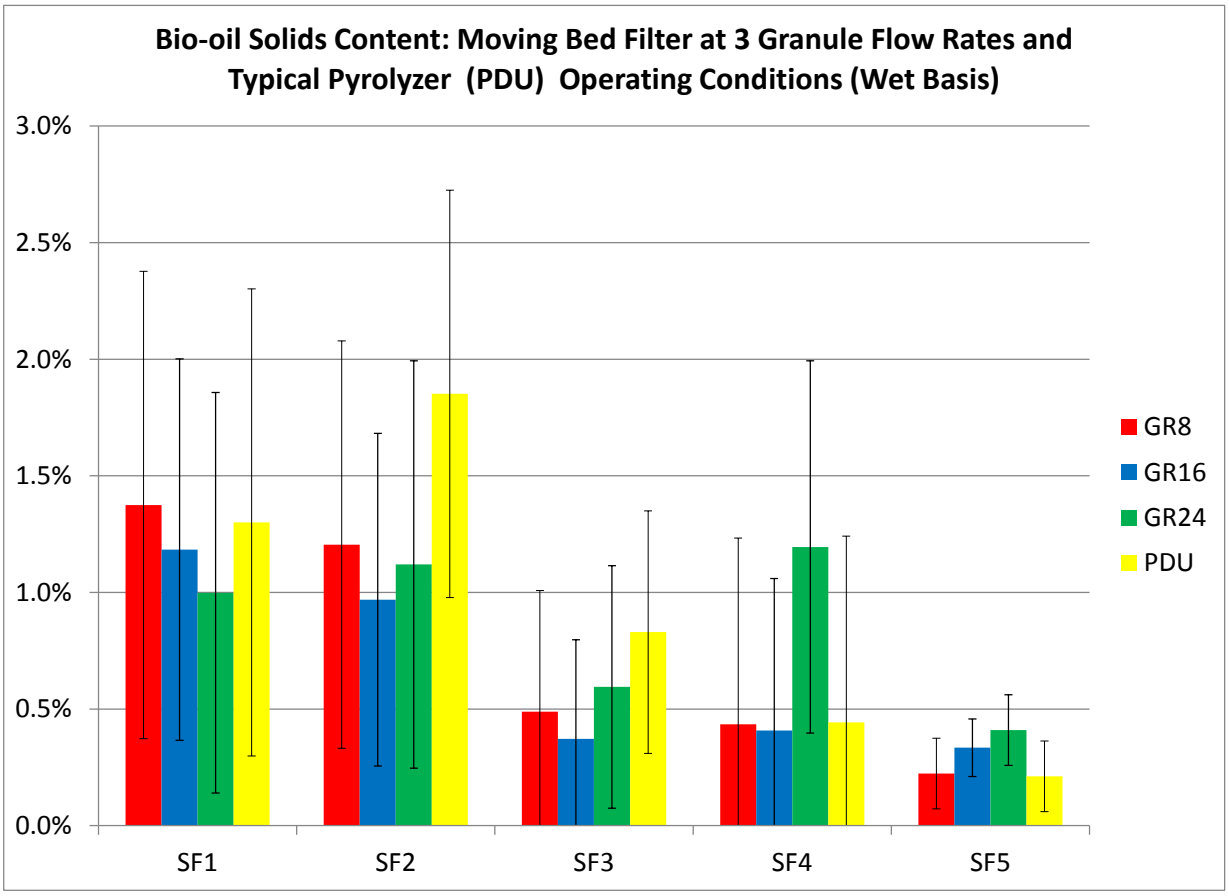

Figure 12: Bio-oil Solids Content

SEM Imaging

This section contains figures generated with the aid of a scanning electron microscope (SEM) when examining char throughout the process. Char separated from the filtration media is shown at several magnifications in Figure 13. At 100x magnification the filtration media (50-200 µm dia.) is clearly identified. The image taken at 500x magnification allows the smaller particles, which originate from the gas flow, to be better distinguished. Two different types of morphological structures are present. Elongated, porous particles typical of primary char are evident. These contrast with amorphous particles that do not appear to be the primary product of pyrolyzing biomass. Instead, these carbonaceous particles appear to have been generated from the shattering of a vitreous monolith into many small fragments. Generation of such monoliths would require the impaction of liquid aerosols or the condensation of vapors onto the granular filter media where they could form a liquid film. The film then polymerized and/or dehydrated to a thin plate of charcoal on and between the granular media. As the granules flowed down through the filter, the thin plates of smooth char would collapse and break into particles observed in the SEM. Magnification to 5000x reveals that the surfaces of the vitreous fragments are covered with tiny, spherical particles, which suggest that fine aerosols were the origin of the liquid phase.

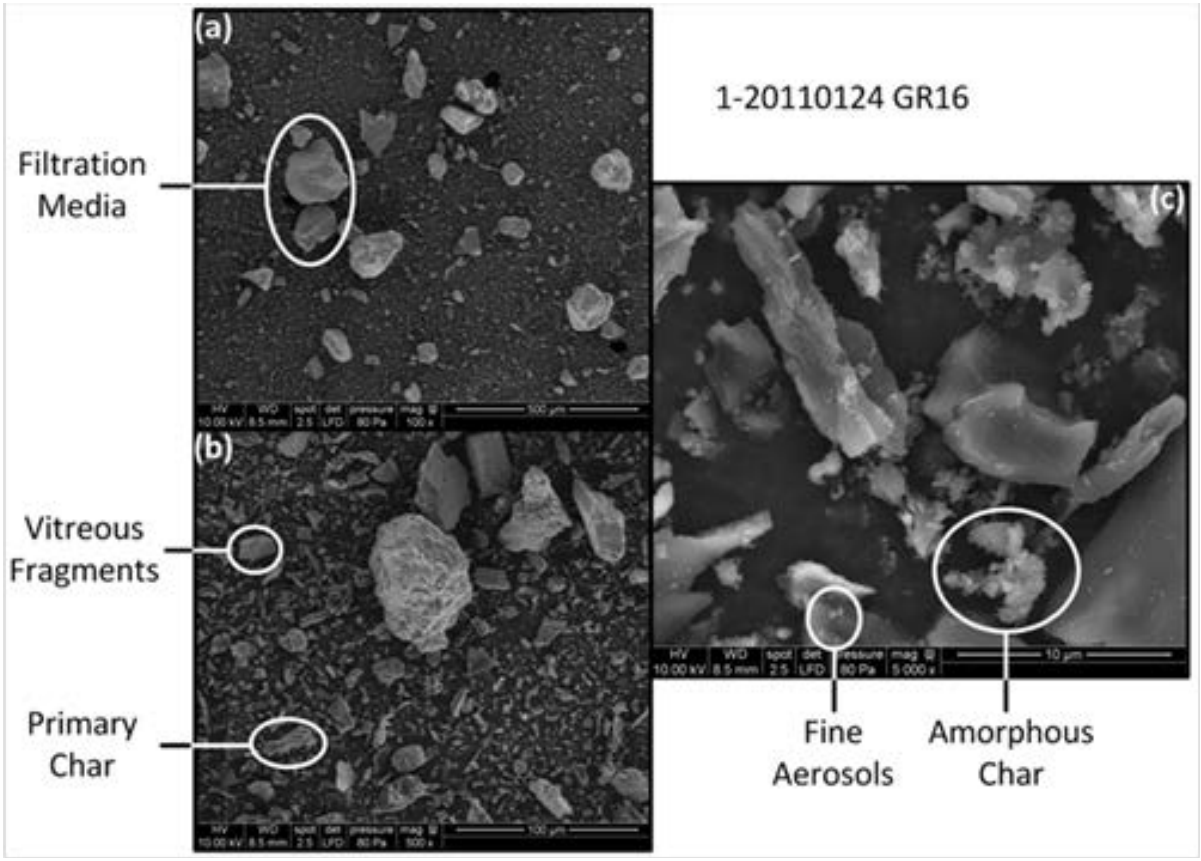

Figure 13: MBGF Separated Char Images at a) 100, b) 500, c) 5000x

In order to have a complete examination of the char throughout the filtration process, char was extracted from bio-oil collected downstream of the moving bed filter. Bio-oil was dissolved in methanol and filtered; the filter was then scraped to obtain a solids sample which could then be analyzed using the SEM. Figure 14 displays SEM images for particulate matter collected from the MBGF and bio-oils from stage fractions 1 and 2 for three media flow rates at 100x magnification. Similarly to the 16 kg/h flow rate previously discussed, the 8 and 24 kg/h MBGF samples contain a variety of particulate matter including mineral matter from the breakdown of filtration media. Qualitatively, it would appear that the 24 kg/h test had the most mineral matter content followed by the 16 kg/h test with the 8 kg/h test having the least filtration media content. This suggests that higher auger speeds promotes grinding of stone used as filter media, the resulting mineral dust being entrained with the gas flow moving through the filter. This apparent increase in mineral matter dust may also be due simply to the increased exposure of pyrolysis gases to larger amounts of filtration media at higher granular flow rates. Amorphous particles are present in all SF1 extracted samples and are markedly similar to those observed in the MBGF separated particulate. No evidence of primary char was observed in these samples. SF2 extracted solid content was also composed entirely of the amorphous particulate matter and in a seemingly smaller quantity than that of stage fraction 1. Both 24 kg/h stage fraction derived samples appear to have a higher concentration of particulate matter than tests at lower flow rates. This could be an indication that sufficient filter

cake may not develop at the higher granular flow rate resulting in decreased filtration efficiency.

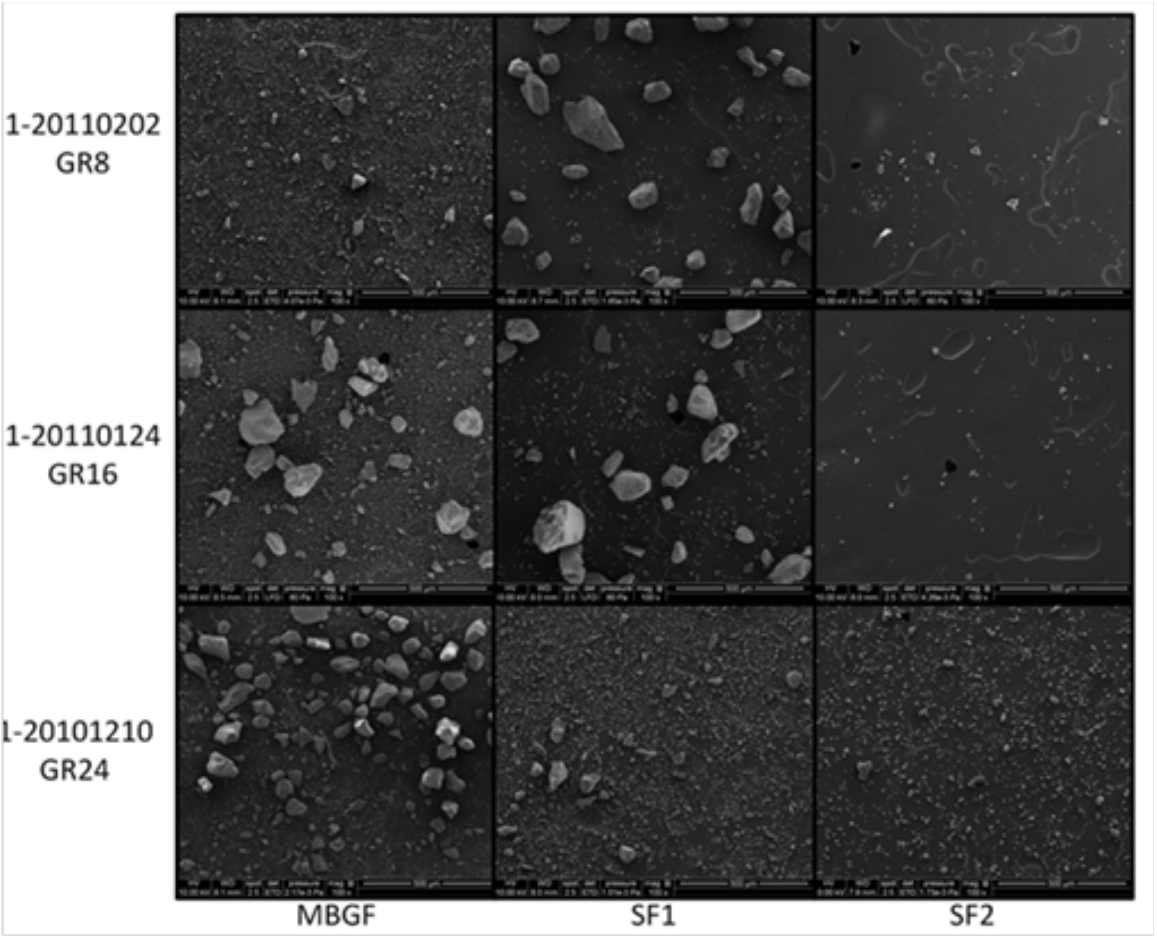

Figure 14: SEM images (100x) of particulate matter recovered from the filtration media of the MBGF and two stages of bio-oil recovery (SF1 and SF2) for three granular flow rates through the filter (GR8, GR16, and GR24 corresponding to 8, 16, and 24 kg/h, respectively)

Figure 14 also reveals the presence of jagged edged particulate in the SF1 bio-oil recovery samples for all three granule flow rate conditions. A hypothesis was formed that the material is mineral matter dust derived from the filtration media which has elutriated from the moving bed filter. In order to test this hypothesis, an SF1 extracted sample was analyzed using a second SEM equipped with EDS detector capable of measuring trace metal content. An x-ray map of the SF1 solids content of an 8 kg/h MBGF test is shown in Figure 15. The background picture in the upper left-hand corner indicates the position of jagged edged particulate matter located throughout the sample. It is very clear though this analysis that the material is primarily composed of aluminum and silica with small amounts of potassium, calcium, magnesium, and iron. The mapping does not indicate the presence of trace metals in the smaller amorphous particulate matter contained in the sample. Some sodium content is present, however the particles are mainly composed of oxygen and carbon as indicated in Figure 15. Since alkali metal concentration is typically high in

primary char, the absence of trace metal in this particulate matter suggests that it was formed after primary pyrolysis during solid-vapor phase interactions (secondary char). It should be noted that the dark shadow regions in the carbon trace map are due to the angle of the EDS detector in relation to the sample causing the larger, jagged edged particulate to overshadow portions of the sample.

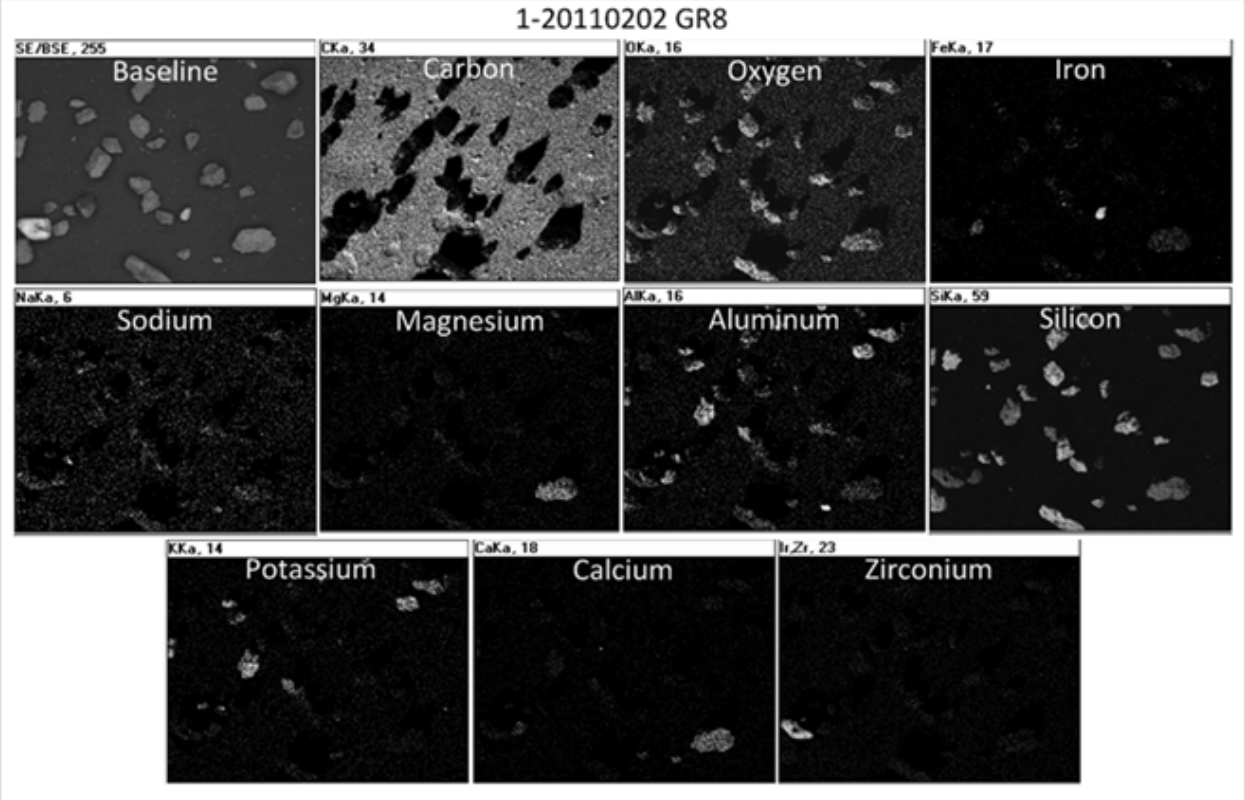

Figure 15: Elemental EDS X-ray Map of SF1 Extracted Solids Content, MBGF 8 kg/h

If the hypothesis presented above holds, a solids extraction from SF1 under normal PDU operation without the MBGF in-situ would not contain any jagged edged particulate. The comparative SEM images for SF1 extracted content are displayed in Figure 16. The PDU baseline sample shows no trace of jagged edged particulate, further supporting the hypothesis. The PDU sample also clearly indicates the presence of primary char. Comparatively, it would appear that the solids collected from the PDU baseline sample are due to a range of particles including both primary char and smaller amorphous particulate matter while the majority of the matter in the MBGF sample is due to the jagged edge particles. Due to its greater density, the jagged edged particulate would have an overwhelming effect on the solids content analysis performed in Section 4.6. The presence of this material is likely the reason a reduction in bio-oil solids content in SF1 samples collected post moving bed filtration could not be detected through mass differencing methods and could also be a factor in measurement consistency.

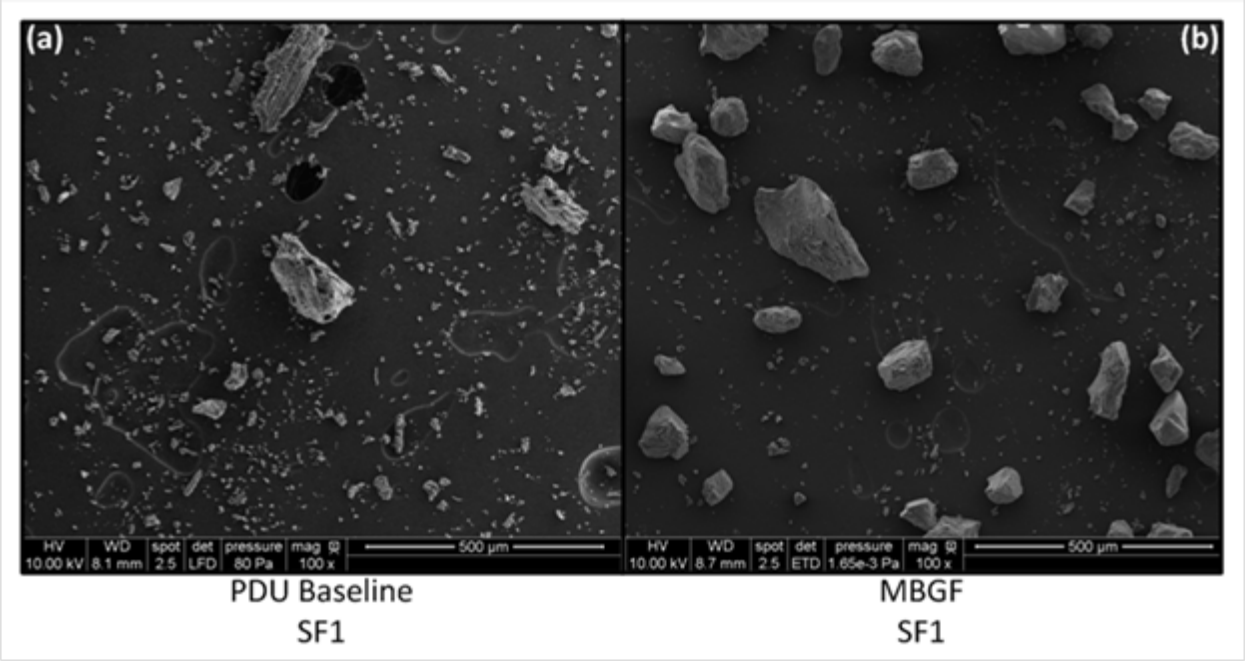

Figure 16: a) PDU Baseline and b) MBGF Bio-oil Solids Extraction SEM Comparison - 100x Magnification

As a result of this analysis it can be concluded that the jagged edge particulate present in the SF1 bio-oil extracted samples is originating from the elutriation of filter media derived mineral matter dust from the MBGF. Qualitatively, the 8 and 16 kg/h tests had increased mineral matter content in SF1 samples compared to the 24 kg/h test. This is likely due to the increased operating pressure differential associated with slower granular flow rates, which translates into increased face velocity at the gas disengagement section of the MBGF. Due to the uniformity of the size, greater density, and larger particle size when compared to the char particulate designated for removal, the MBGF could easily be redesigned to avoid this elutriation. A simple geometry change resulting in a larger surface area at the filter's exit and thus a slower exit face velocity could eliminate this phenomenon all together.

Accelerated Aging and GPC (UV-Vis Detector)

The baseline data of each MBGF test was compared to that of PDU baseline operation using the GPC software directly. These graphs plot milli-absorbance units by retention time in minutes resulting in higher molecular weight compounds on the left of the graph and progressively lower molecular weight compounds traversing to the right. By comparing these curves, anomalies in the types of compounds being collected during filtration would be apparent. As shown in Figure 17, no anomalies were present and the PDU baseline curves are nearly identical to that of the MBGF test. This same comparison was made for each granule flow rate tested and no anomalies were found.

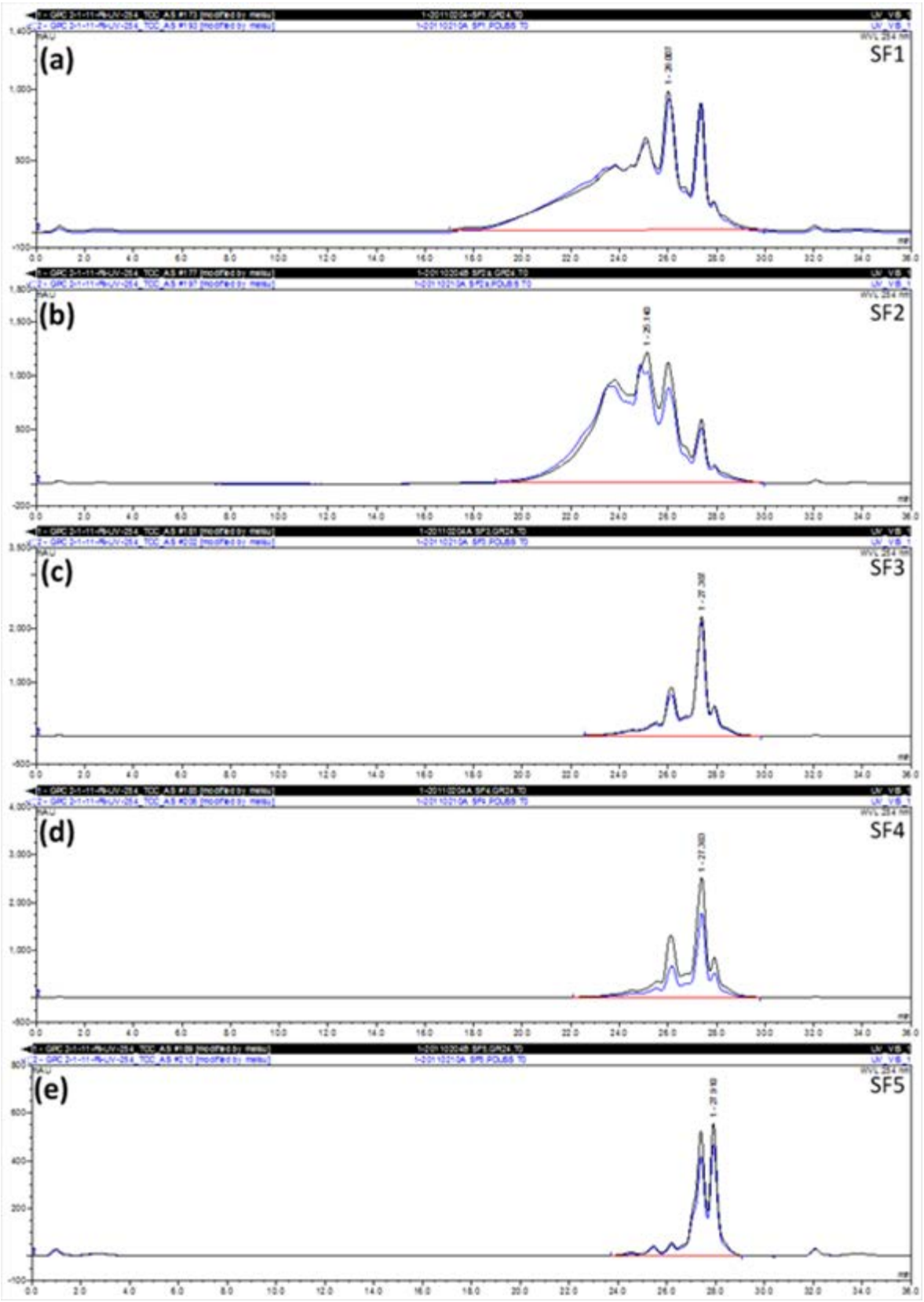

Figure 17: GPC Molecular Weight Curve Comparison between GR24 MBGF and PDU Baseline Operation for a) SF1, b) SF2, c) SF3, d) SF4, and e) SF5

Figure 18 displays the results of an aging study conducted previously on the pyrolyzer PDU. The amplitude on the y-axis corresponds to the number of constituents in the sample that have the molecular weights shown on the x-axis. The molecular weight curves progress in aging from "TIME 0 HR"(blue) corresponding to bio-oil as collected to "TIME 24 HR"(purple) corresponding to 24 hours of aging at 90°C. In the case of each stage fraction, the peak(s) toward the beginning of the curve associated with lower molecular weight species shrink in response area height as the bio-oil is aged. At the same time, the last peak toward the end of the curve associated with higher molecular weight compounds increases and broadens as the bio-oil is aged. These graphs clearly indicate the occurrence of polymerization reactions in the oil under accelerated aging conditions.

Similar graphs have been generated for results obtained at each of the three tested MBGF granular flow rates. Aging analysis was conducted on two tests run at each granular rate, the results of which are displayed in Figure 19 - Figure 21. Once again, a clear trend of increased higher molecular weight compounds and decreased lower molecular compounds with accelerated aging is present under all MBGF conditions tested.

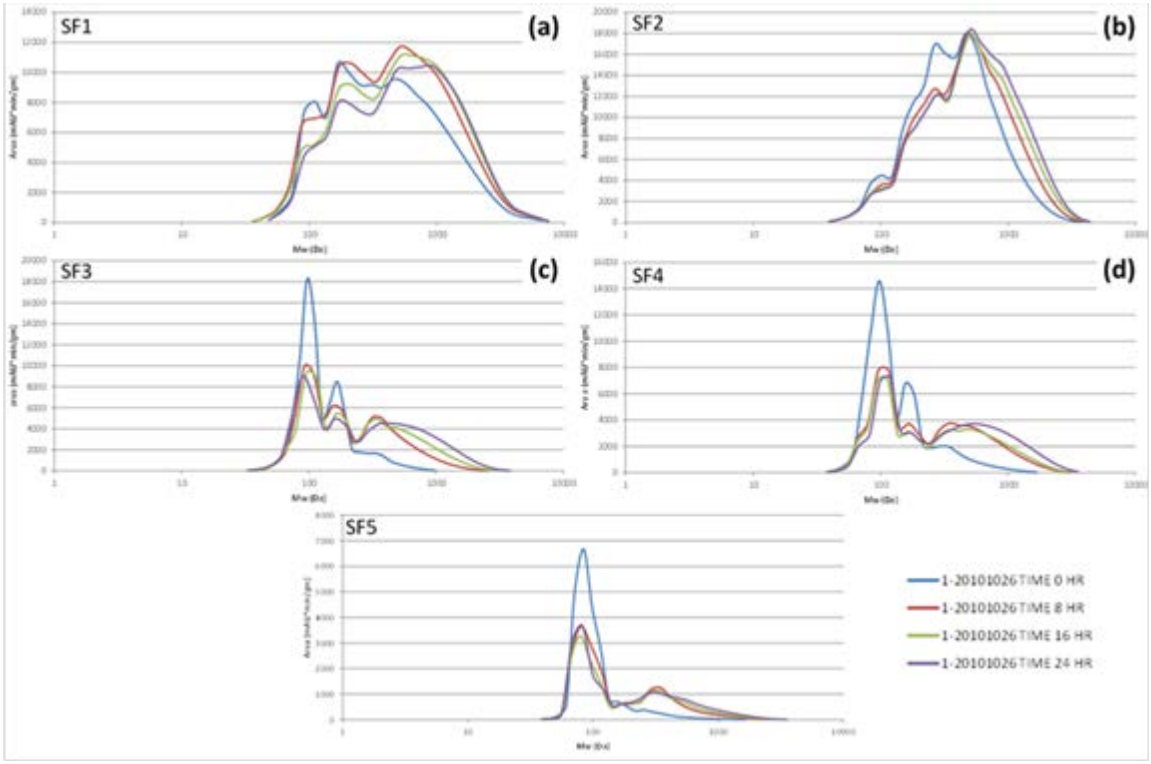

Figure 18: GPC Bio-oil Comparison of PDU Baseline Samples at 0, 8, 16, and 24h Aging Periods for a) SF1, b) SF2, c) SF3, d) SF4, and e) SF5

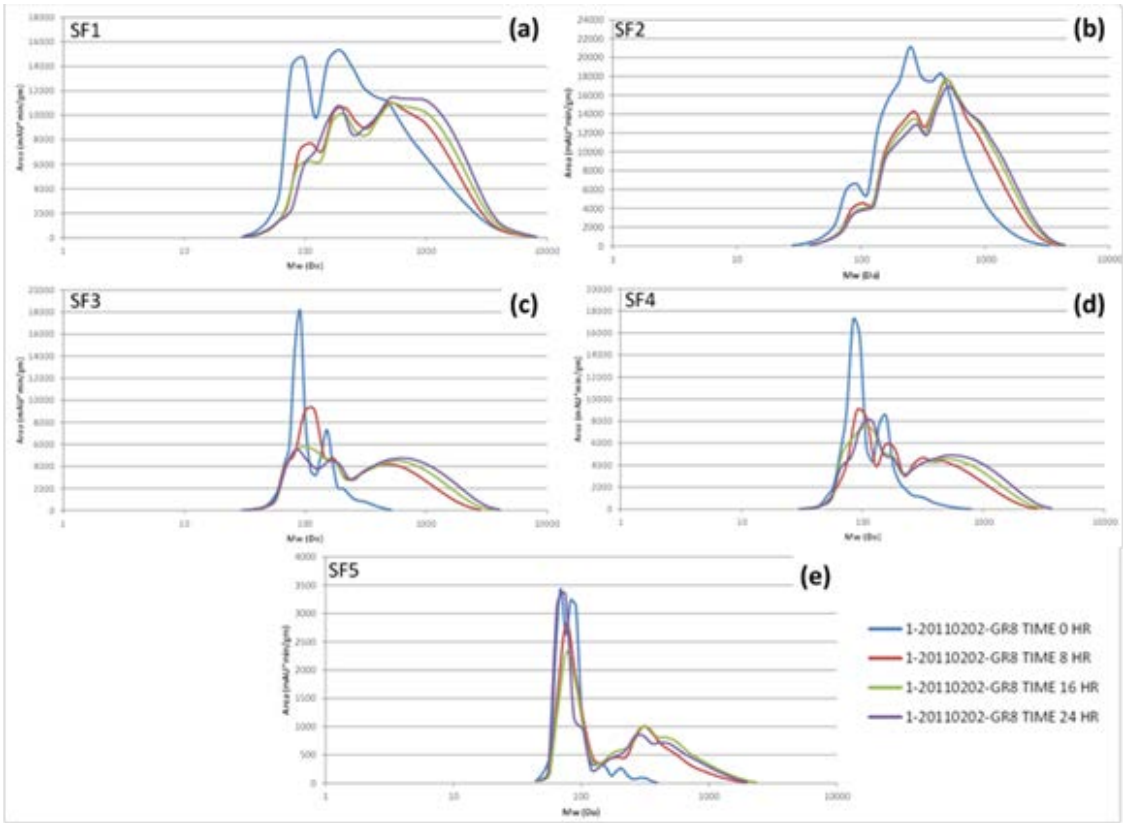

Figure 19: GPC Bio-oil Comparison of MBGF GR8 Samples at 0, 8, 16, and 24h Aging Periods for a) SF1, b) SF2, c) SF3, d) SF4, and e) SF5

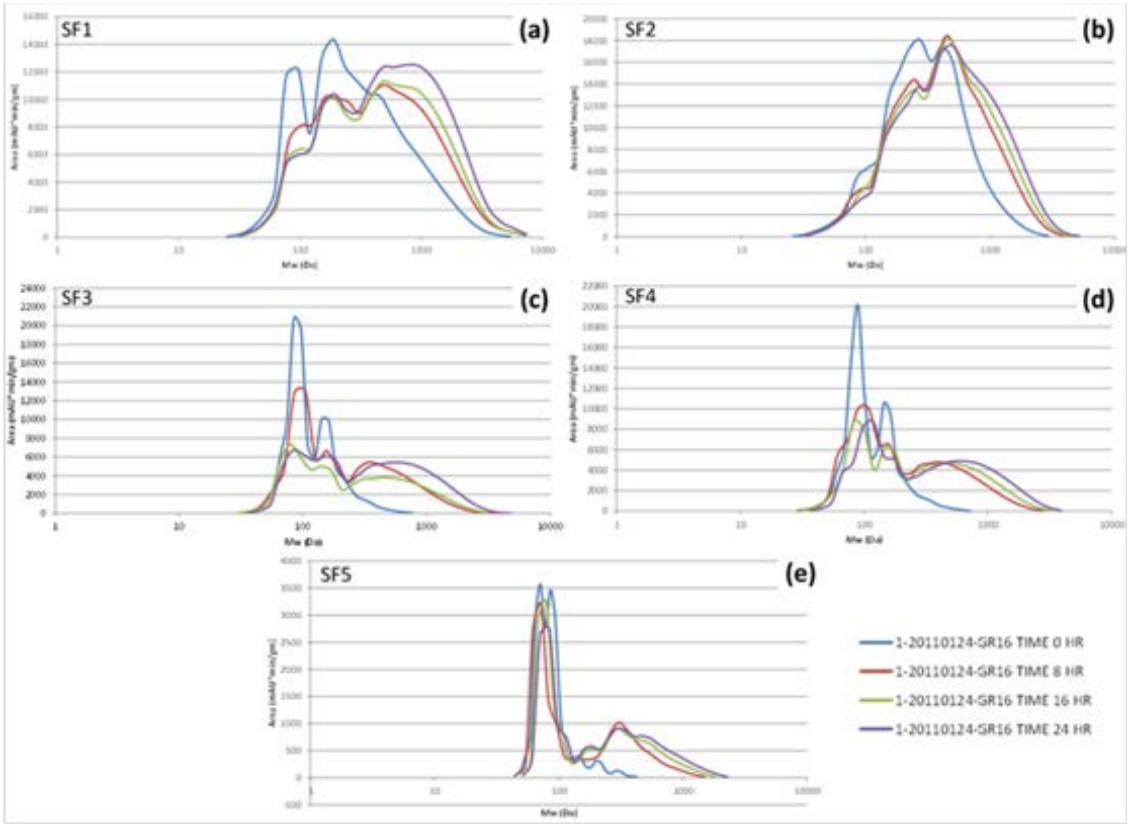

Figure 20: GPC Bio-oil Comparison of MBGF GR16 Samples at 0, 8, 16, and 24h Aging Periods for a) SF1, b) SF2, c) SF3, d) SF4, and e) SF5

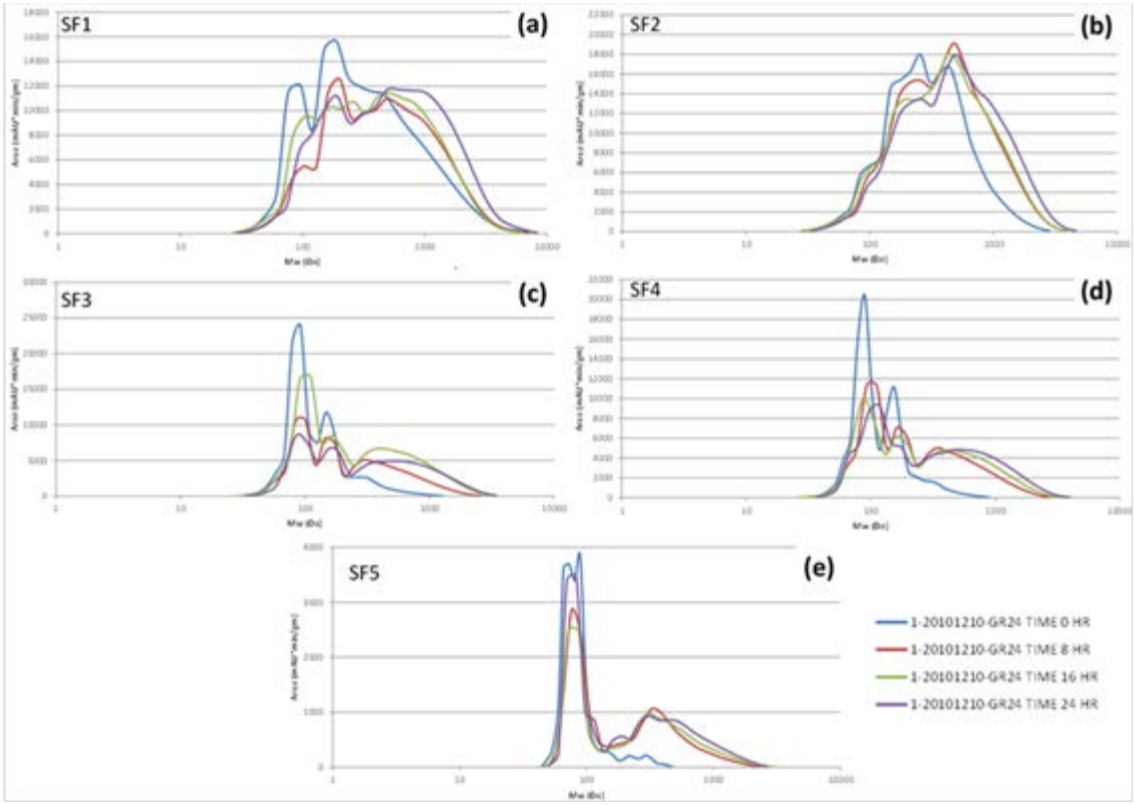

Figure 21: GPC Bio-oil Comparison of MBGF GR24 Samples at 0, 8, 16, and 24h Aging Periods for a) SF1, b) SF2, c) SF3, d) SF4, and e) SF5

Each fraction of baseline oil undergoes the majority of the aging process within the first 8 hours. The same conclusion could be drawn about bio-oil stage fractions 1, 2, 4, and 5 obtained from all three MBGF operating conditions tested. In the case of SF3, polymerization appears to complete after 16 hours of accelerated aging. SF1 bio-oil samples appear to age less under MBGF operating conditions than baseline PDU operation. The lower molecular weight peaks associated with MBGF trials decrease to approximately 8,000 for the first peak and 12,000 for the second. However, baseline oil low molecular weight peaks settle at 5,000 and 8,000 after aging is complete. In all four cases, high molecular weight peaks in the SF1 samples increase to approximately 12,000. Therefore, MBGF SF1 samples appear to undergo a smaller reduction in low molecular weight species than the baseline SF1 sample. A similar trend is observed with SF2 bio-oil samples as the baseline sample decreased to 12,000 and increased to 20,000 for low and high molecular weight species respectively. The MBGF SF2 samples decreased to 14,000 and increased to 17,000 for low and high molecular weight species respectively. SF3 bio-oil ages to the same extent in all four instances, however, bio-oil obtained from MBGF trials does so at a much slower rate, requiring upwards of 16 hours of accelerated aging to reach stable molecular weight levels. No discernable differences between baseline and MBGF bio-oil aging can be determined in the cases of SF4 and SF5.

To quantify the aging process, the molecular weight distributions from the GPC analyses were converted into number averaged molecular weights as a function of time using the relationship:

Equation 4: Number Averaged Molecular Weight

$$M_n = \frac{\sum_i N_i M_i}{\sum_i N_i}$$

where the products of the molecular weight of molecule i is multiplied by the number of molecules of that size, N_i, are summed and divided by the total number of molecules.

Acid-catalyzed free radical polymerization is expected to follow a second-order reaction model, which can be express as:

Equation 5: Acid-catalyzed Second-Order Reaction Model

$$\frac{M_n(t)}{M_n(t_0)} - 1 = kt$$

where t is time, t0 is the starting time, and k is the second-order reaction rate constant. This model was used to correlate the four time intervals evaluated for accelerated again trials (0, 8, 16, and 24 hours). All of the resulting plots show excellent correlations with the two most viscous fractions (SF 1 and 2) generally shown rate constants for polymerization that were half that of the other fractions (SF 3, 4 and 5). This slower rate constant of aging for the viscous fractions may reflect that these samples are already highly oligomerized. Figure 22 compares the effect of filtration on the rate constants for each stage fraction. In most cases a general trend of increased reaction rate coefficient with increased granule flow is apparent. The baseline reaction coefficient trends reasonably well with filtration occurring at a granular flow rate of 8 kg/h in the first three fractions. In the fourth and to a greater extent the fifth fraction the baseline reaction rate is greatly reduced. In general, the bio-oil obtained from baseline operating conditions had a lower polymerization reaction coefficient than bio-oil obtained from MBGF operating conditions.

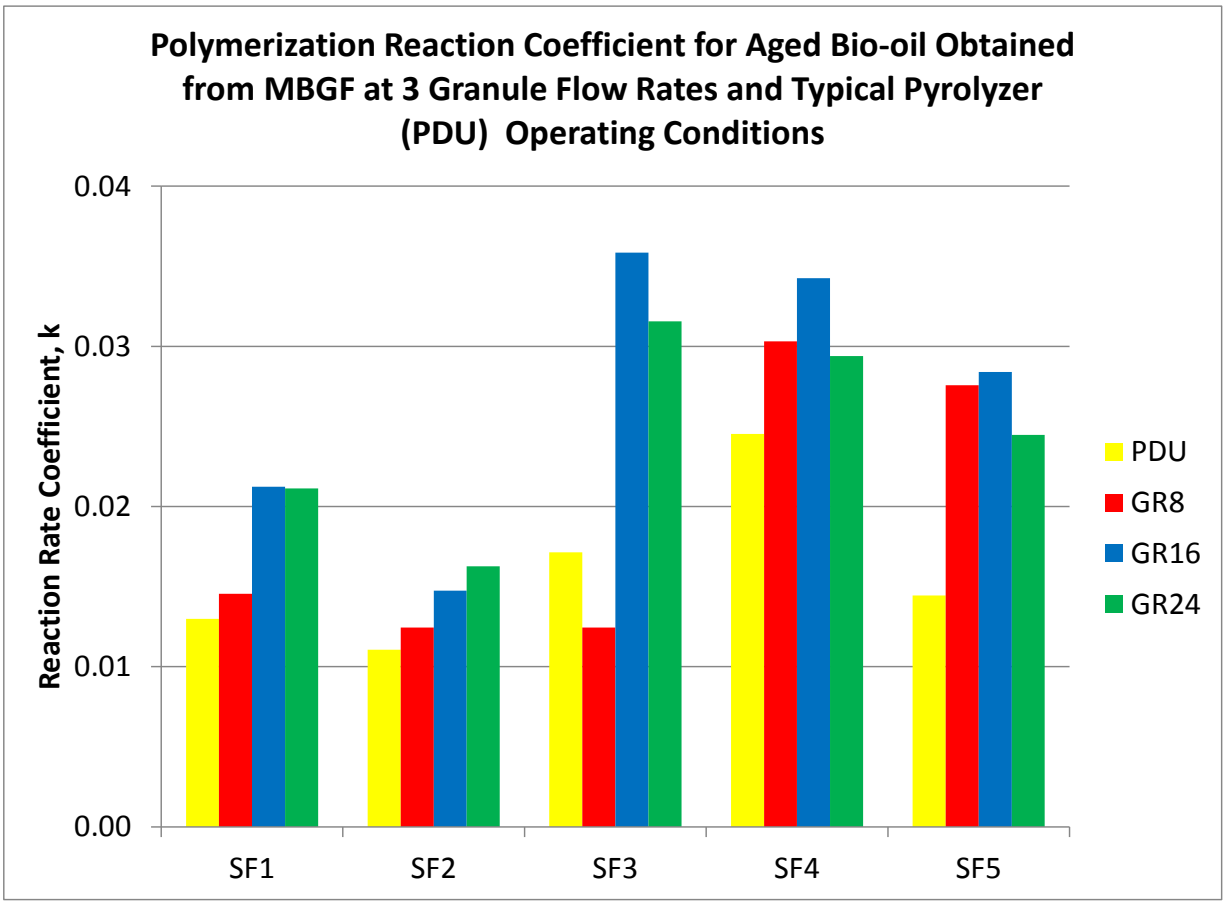

Figure 22: Second Order Polymerization Model Reaction Rate Coefficients for Aged Bio-oil Samples from PDU and MBGF at 3 Granular Flow Rates

Conclusions

This work has successfully shown the ability to sustainably operate a demonstration scale moving bed granular filter at high temperatures in the presence of a pyrolysis product stream. Limitations on both granular flow rate and operating temperatures exist and have been identified

Pyrolysis operation with the MBGF in-situ resulted in bio-oil that was higher in moisture content suggesting the occurrence of secondary dehydration reactions occurring in the filter. The extent of the moisture increase was dependent on granular flow rate. The presence of the filter had an apparent effect on bio-oil water insoluble content and was also dependent on granular flow rate.

Quantitative measurements with regards to solids removal were difficult to make and inconclusive using traditional methods. However, qualitative analysis by SEM shows no evidence of biomass derived particulate in MBGF derived bio-oil samples, yet shows distinct evidence of its presence in baseline derived oil. SEM analysis also confirms the presence filtration media derived dust in SF1 samples.

SEM analysis confirms the removal of primary char by the MBGF at all tested granular flow rates through examination of the spent filtration media. Additional analysis of SF1 derived bio-oil solids content confirms the presence of filtration media derived dust in samples obtained at each granular flow rate. Smaller char particles present in bio-oil derived samples appear to have formed after primary pyrolysis during secondary reactions taking place post moving bed granular filtration.

ICP analysis of the baseline and MBGF collected bio-oil indicates that overall trace metal concentrations are not reduced when using the filter in-situ. However, analysis of the filtration media indicated that the same trace metals are present in the media and could contribute to bio-oil contamination through the transport of dust particles elutriating from the filter.

Accelerated bio-oil aging analysis indicates that all bio-oil samples collected with the MBGF in-situ experienced some degree of aging. This phenomenon could be a result of the presence of alkali metal remaining in the bio-oil product stream due to filtration media derived dust contamination. Additional polymerization reaction modeling indicates that bio-oil obtained from MBGF operation had a larger reaction coefficient than bio-oil obtained from baseline operation.

Future Work

Several areas of improvement for MBGF operation have been identified as a result of this work. A simple geometry change resulting in a larger surface area at the exit of the filter would eliminate the elutriation of larger filtration media derived dust which collects in SF1. This change should help facilitate more accurate bio-oil solids content measurements in future MBGF derived samples. The change to a less frangible filtration media would reduce grinding in the transport augers and eliminate the creation of very fine dust particles that eventually contaminate collected bio-oil. The use of an inert filter media, such as glass beads or crushed granite, would eliminate the media as a source of trace metal contamination and allow mass balances on alkali partitioning occurring within the pyrolysis process. The incorporation of a recycling loop with the ability to remove carbonaceous residue from the media through combustion would decrease the amount of media needed for testing and reduce the amount of heat input required to operate the system. Future moving bed granular filtration work should include the application of these solutions and possible progression to the addition of rugged, deoxygenation catalysts to the filtration media.

References

1. Pollard, A.J.S., *Comparison of bio-oil produced in a fractionated bio-oil collection system*, Master's Degree Thesis, 2009, Iowa State University: Ames, IA.

Task #3: Fractionating Recovery of Vapors and Aerosols

Two main activities were conducted during this task. The first dealt with upgrades made to the pyrolysis system in order to improve reliability and repeatability. The second major activity was an optimization study that examined the effect of the pyrolysis reactor temperature on the composition and stability of the bio-oil collected with the fractionating condenser train. Both major activities will be discussed in the following paragraphs.

Tests to examine the effect of reactor temperature on the properties and stability of fractionated bio-oil were completed. Initial plans were to pyrolyze from 400 to 600°C in increments of 50 degrees. This range was later modified to 350 to 550 °C after a maximum bio-oil yield was observed at 400 °C. Reactor residence time was kept approximately constant by varying the flow rate of the nitrogen fluidizing gas. Fractionating condenser conditions were not varied. Yield data were recorded and non-condensable gas was analyzed using a micro-gas chromatograph (Micro-GC.) Mass balance closure was attained for all five tests. Pyrolysis product yields are below.

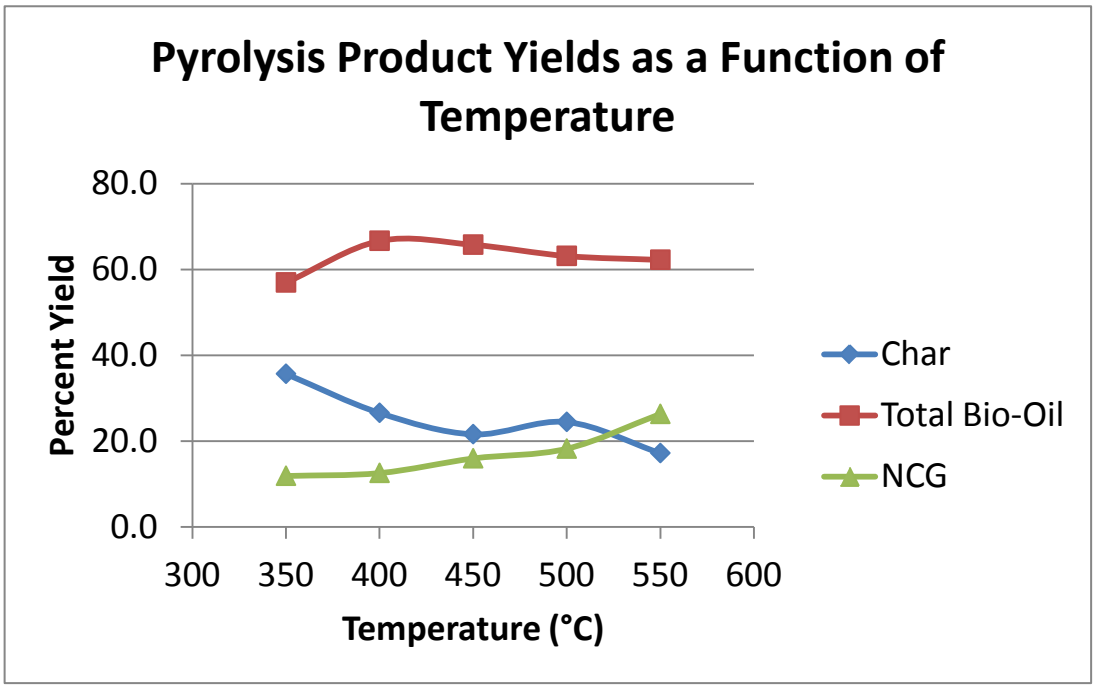

Figure 1. Yields of pyrolysis products as a function of pyrolysis temperature

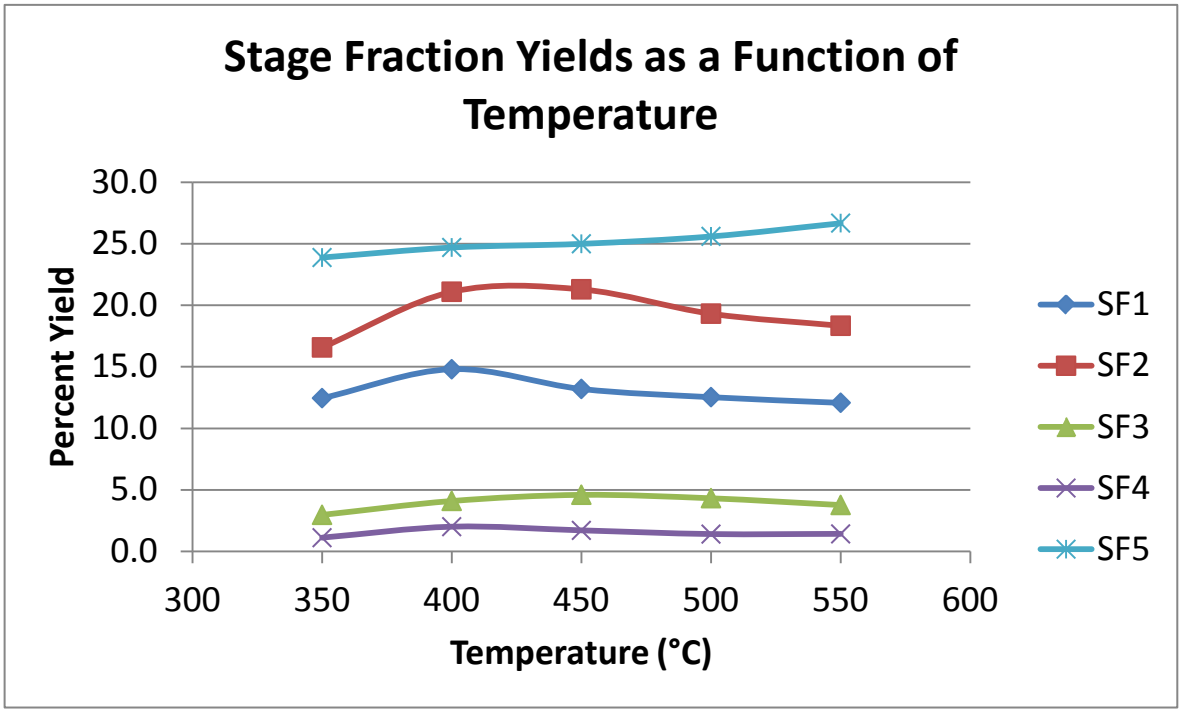

Figure 2. Yields of stage fractions as a function of pyrolysis temperature

Maximum bio-oil yields are typically said to occur at ~500°C in literature. However, articles describing experiments done on a specific apparatus yield a much wider range of temperatures of maximum yield, anywhere from 400 to 600 °C. For the PDU, maximum total oil yield occurred on the low end of this range, at 400 °C. If high yields are the main objective, this data indicates they can be achieved in the PDU at a low reactor temperature, resulting in lower operating costs and less wear and tear on equipment. It should be noted that total oil yield only dropped from 66.76% at 400°C to 62.28% at 550°C, suggesting other measures of bio-oil quality may be more important in determining optimal reactor temperature. Three of the five fractions have clear yield optima (SF1, SF2, and SF3). This could be due to the different temperatures at which the three major components of biomass decompose. Cellulose decomposes between 240 and 350°C, and lignin decomposes between 280 and 500°C depending on feedstock. Because SF1 is designed to collect anhydrosugars (specifically, levoglucosan), the maximum yield of SF1 would be expected to occur before the maxima of SF2 and SF3, which are designed to collect lignin-derived products (aerosols and phenolics). Note that the ESP modifications (discussed below) have drastically reduced the yield of the second ESP as well as the yield of the ESP of SF4. Chemically, SF4 seems to be a blend of SF3 and SF5. Further optimization of the collection system could potentially result in fewer stage fractions, or stage fractions aimed at further separation of classes of compounds.

Analysis of the fractions produced at the varying reactor temperatures was completed. Planned analyses included Modified Acid Number (MAN), moisture content, water insolubles, GC-FID, molecular weight via Gel Permeation Chromatography (GPC), and total sugars via an FTIR method developed within CSET. Accelerated aging at 90°C for 8,

16, and 24 hours was performed on all fractions for the five reactor temperatures. Aged samples were analyzed by GPC. Results of the analyses are given below.

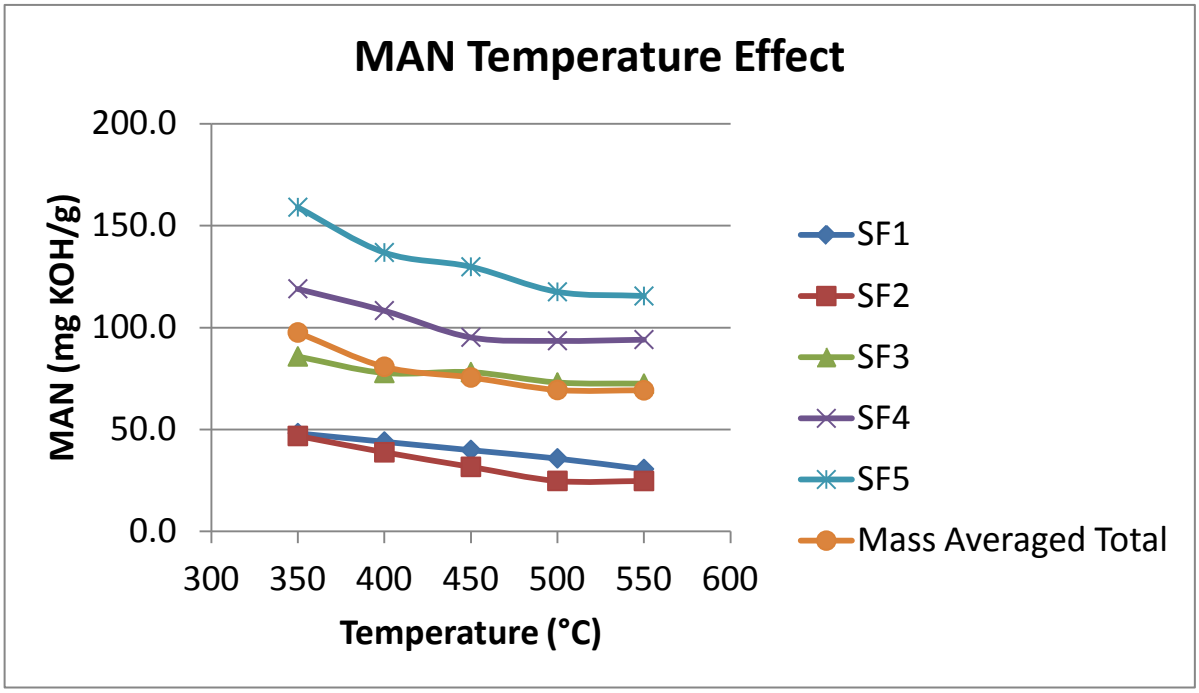

Figure 3. Modified acid number (MAN) of stage fractions as a function of pyrolysis temperature

Modified Acid Number (MAN) decreased with temperature for all fractions, as well as on a mass averaged basis representing a "whole" bio-oil obtained by recombining the fractions. Mass averaged total MAN decreased from 97.6 to 69.2 mg KOH/gm sample from 350 to 550 °C. Decreases in MAN taper off after 500°C, except for SF1. Minimum MAN required operation at 500 °C, although the difference in MAN between 450°C and 500°C is relatively modest. Mass averaged total MAN at the temperature of maximum yield (400 °C) is 80.7 mg KOH/gm sample compared to 69.3 mg KOH/gm sample at 500 °C. This reduction in MAN is achieved at the expense of a 3.5% reduction in bio-oil yield. Bio-oil MAN is still higher than accepted for refining petroleum, but in related work, MAN has been found to strongly correlate with the acetic acid content of the bio-oil. Because acetic acid has a relatively low boiling point, it is unlikely to have the same hot corrosion potential of the naphthenic acids found in petroleum.

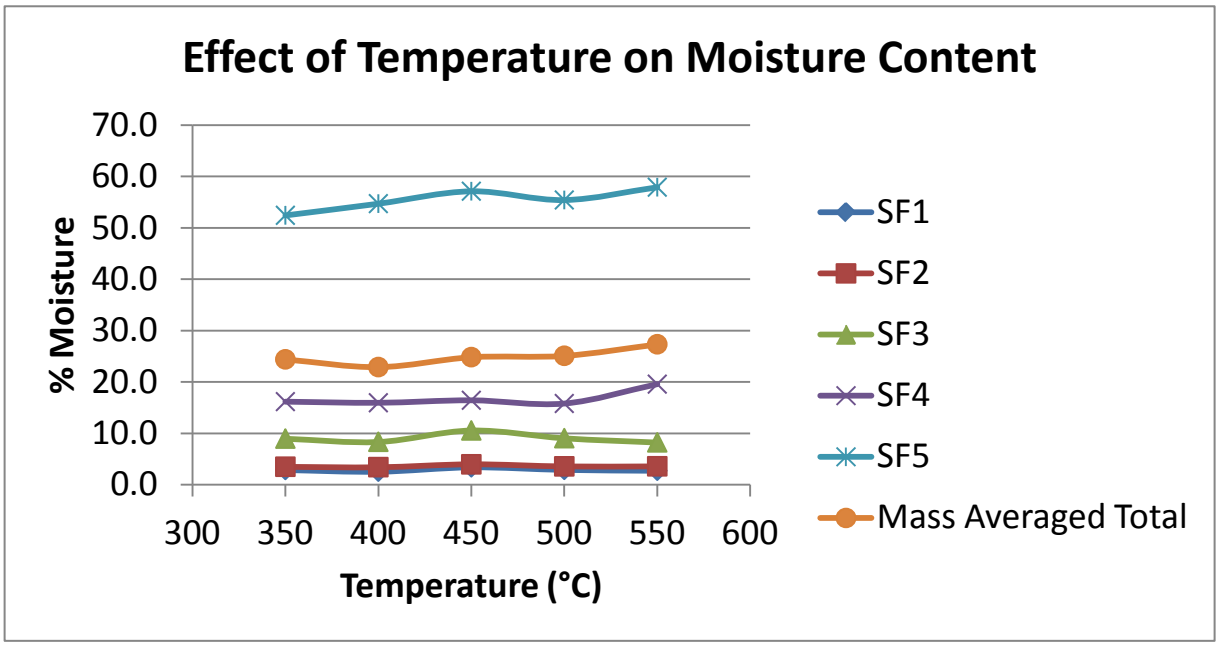

Figure 4. Moisture content of stage fractions as a function of pyrolysis temperature

The moisture content of SF1, SF2, and SF3 remained constant over the range of reactor temperatures tested. This was expected, as condenser operating conditions were not changed. Differences in the moisture content of the product stream exiting the reactor were found in SF5, as seen in Figure 4, which was designed to collect water along with light oxygenates. The minimal mass averaged moisture content of 22.9% occurred 400 °C compared to 27.3% at 550 °C. These values fall within the 15-30% bio-oil moisture content found in the literature for whole bio-oils. In figures 3 and 4, there is a striking correlation between the partitioning of acidity, as measured by MAN, and the moisture content of the stage fractions at a given temperature. The acidity of stage fractions 1 - 4 may be the result of acetic acid vapors absorbing into moisture that condenses in these stages. Refinement of the bio-oil recovery system to further reduce moisture content of stage fractions 1 - 4 is likely to dramatically drop MAN and drive additional acidity to SF5.

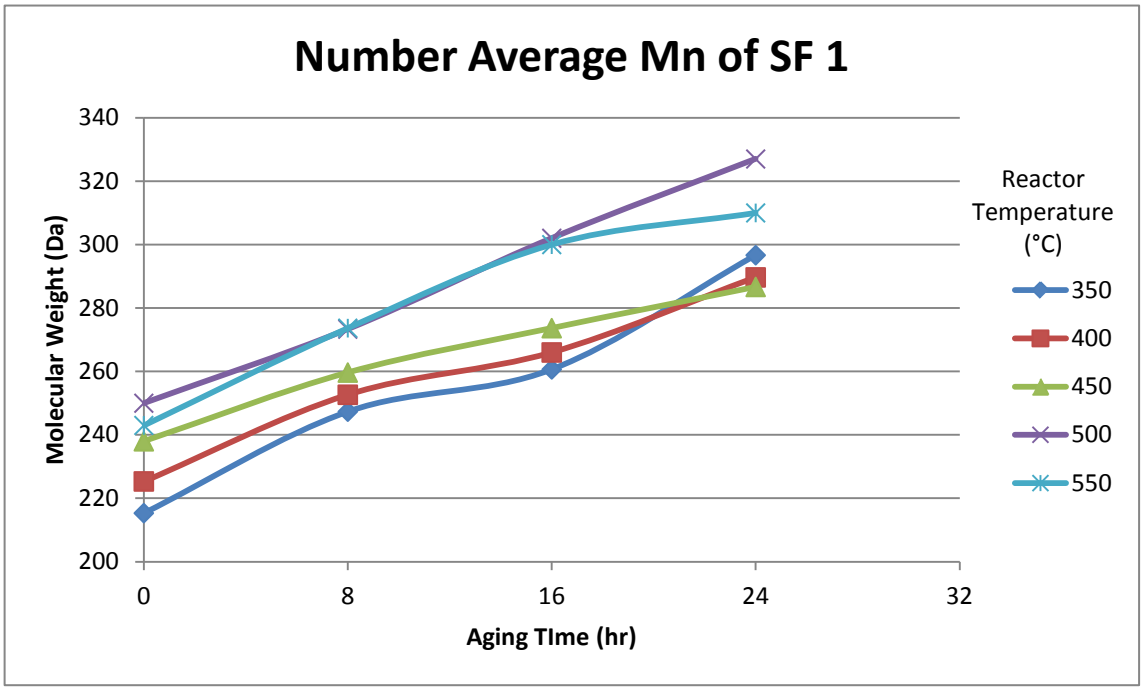

Figure 5. Number average molecular weight of SF1 as a function of pyrolysis temperature

An analysis of average molecular weight as a function of accelerated aging time has been completed. For SF1 (Figure 5), pyrolysis at lower temperatures has the effect of decreasing the final molecular weight after aging. SF2 exhibits the clearest temperature effect of all the fractions. The oil produced at 350°C has the lowest final molecular weight, with final molecular weight increasing with temperature all the way to 550 °C (Figure 6). SF3 and SF4 produced at 400 and 450°C appear to be most stable (Figures 7&8). Interestingly, the SF3 and SF4 fractions produced at 350°C show the largest changes in average molecular weight. Conclusions about the optimum temperature for the last fraction are difficult (Figure 9). SF5 produced from 400 to 550°C ages in a similar manner, with only the 350°C SF5 exhibiting a significantly higher final molecular weight. In a positive development, oils produced at the temperature where yield is maximized performed relatively well in the stability studies. A comparison of the five fractions at each reactor temperature is also included below (Figures 10-14). From these comparisons, clear separation of different molecular weights within the fractionating condenser can be seen. With the exception of the oil produced at 350 °C, SF2 collects the highest molecular weight, as expected for an ESP intended to collect aerosols. SF3 and SF4 collect compounds of number average molecular weight approximately 100 Da less than SF1. From these figures SF3 and SF4 appear quite similar. Low molecular weight compounds are clearly ending up in SF5 as designed.

Changing the reactor temperature does not completely eliminate the bio-oil aging problem, as can be seen above. However, changing the reactor temperature has a definite effect on the molecular weight distribution of the fractionated bio-oil. The data indicate the potential for fractionating bio-oil produced at an optimized temperature in a fluidized bed reactor as a first step in tailoring the oil for specific end uses.

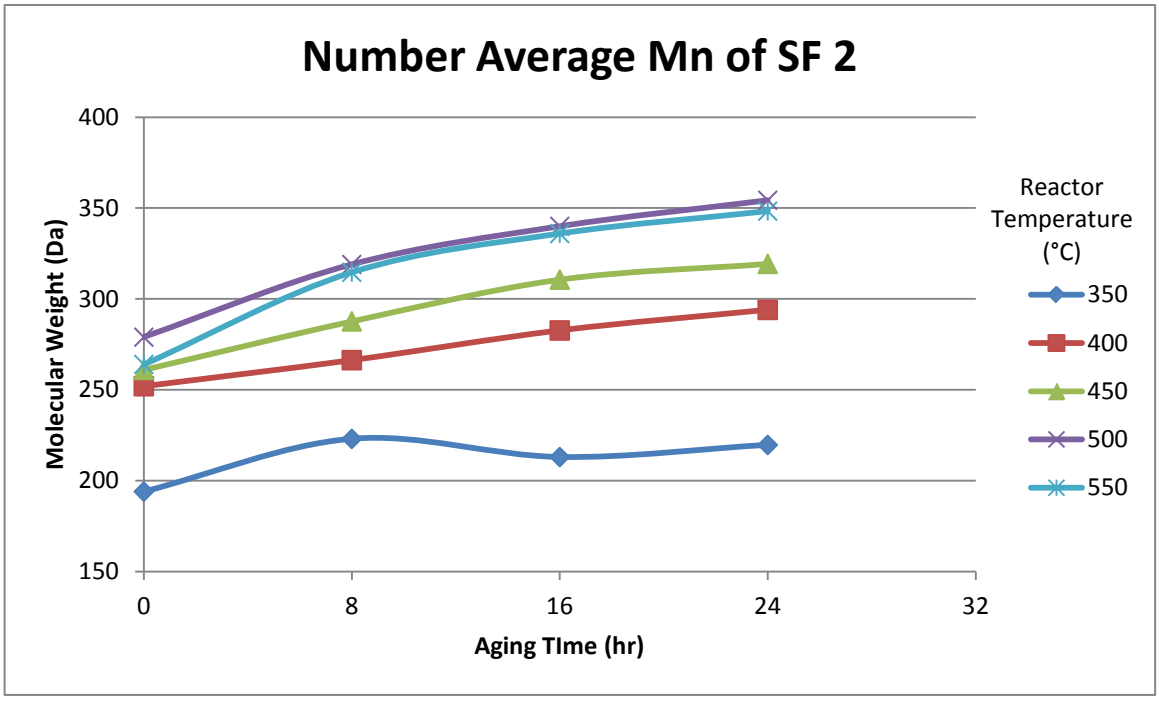

Figure 6. Number average molecular weight of SF 2 as a function of pyrolysis temperature

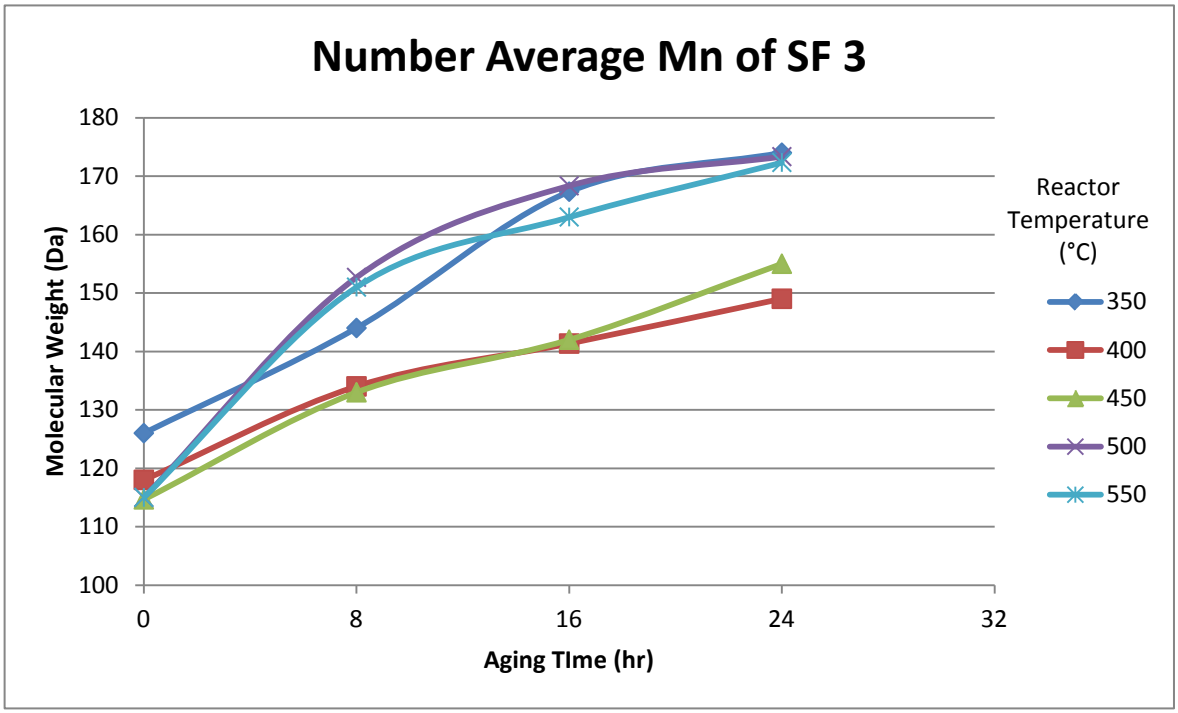

Figure 7. Number average molecular weight of SF 3 as a function of pyrolysis temperature

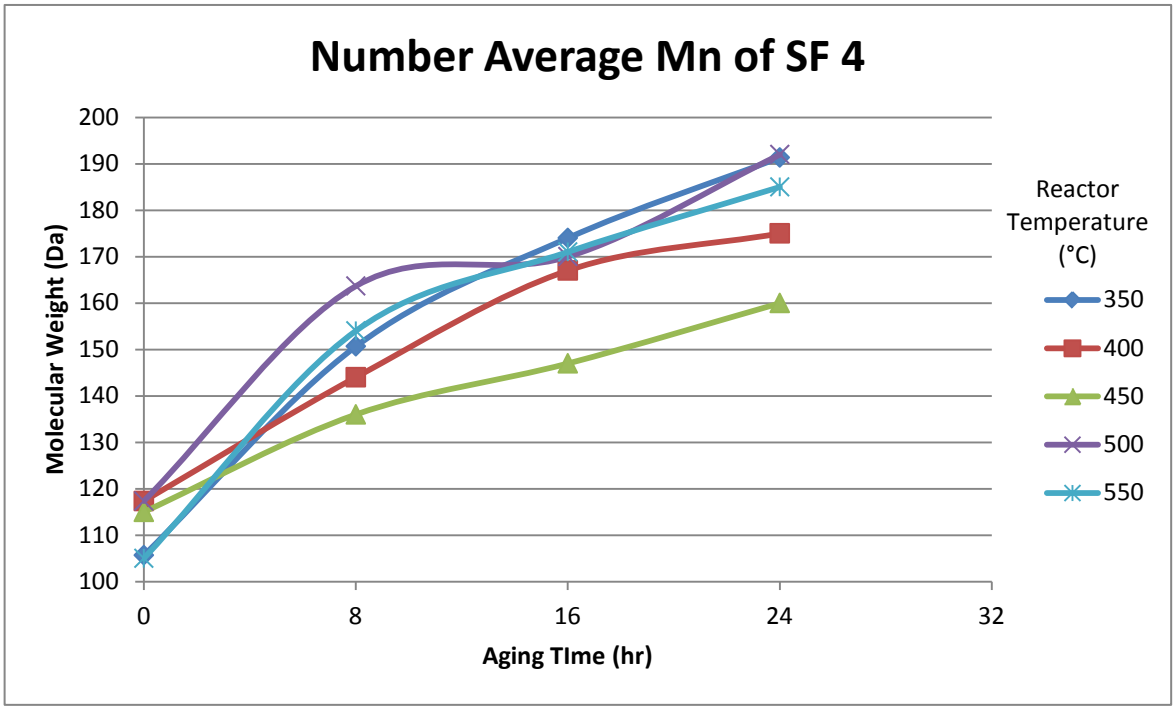

Figure 8. Number average molecular weight of SF 4 as a function of pyrolysis temperature

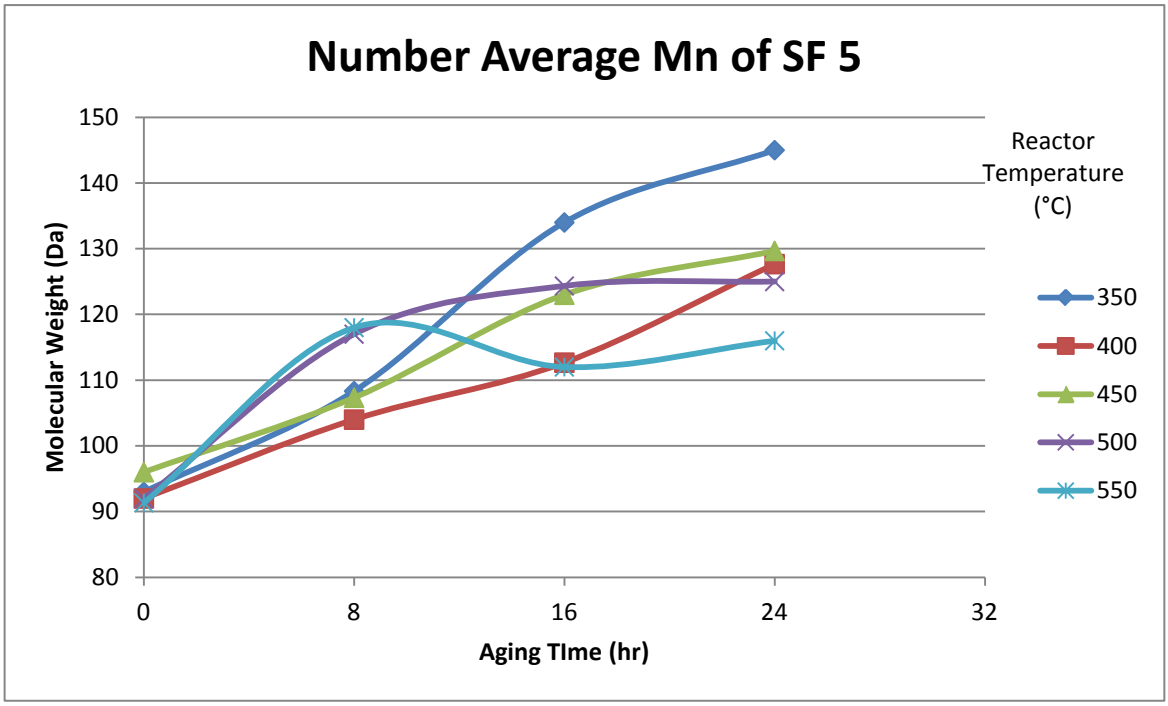

Figure 9. Number average molecular weight of SF 5 as a function of pyrolysis temperature

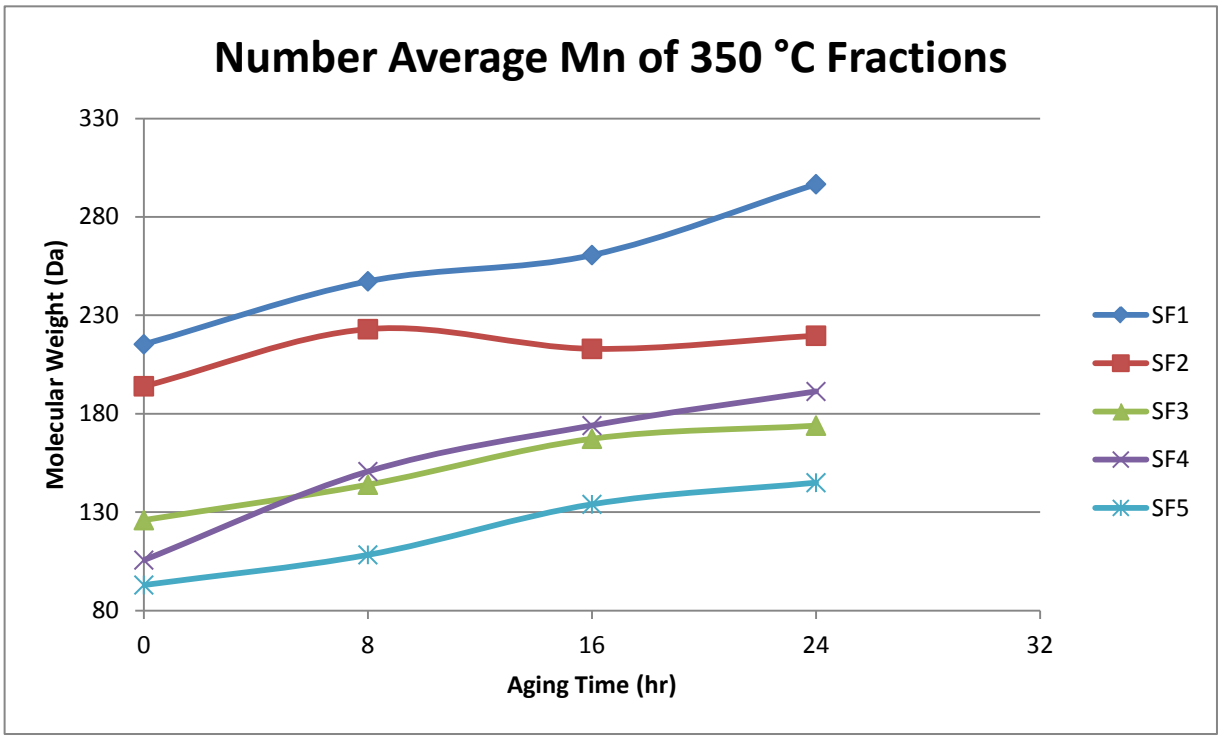

Figure 10. Number average molecular weight of the fractions produced at 350 °C

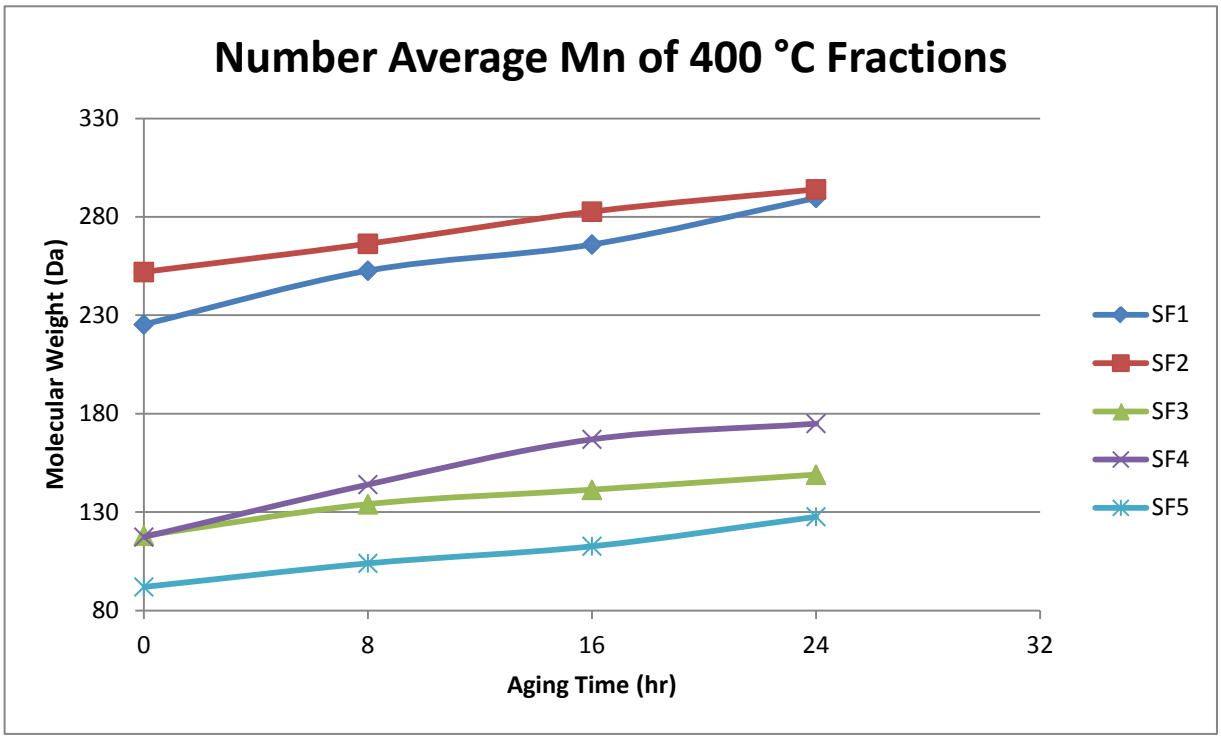

Figure 11. Number average molecular weight of fractions produced at 400 °C

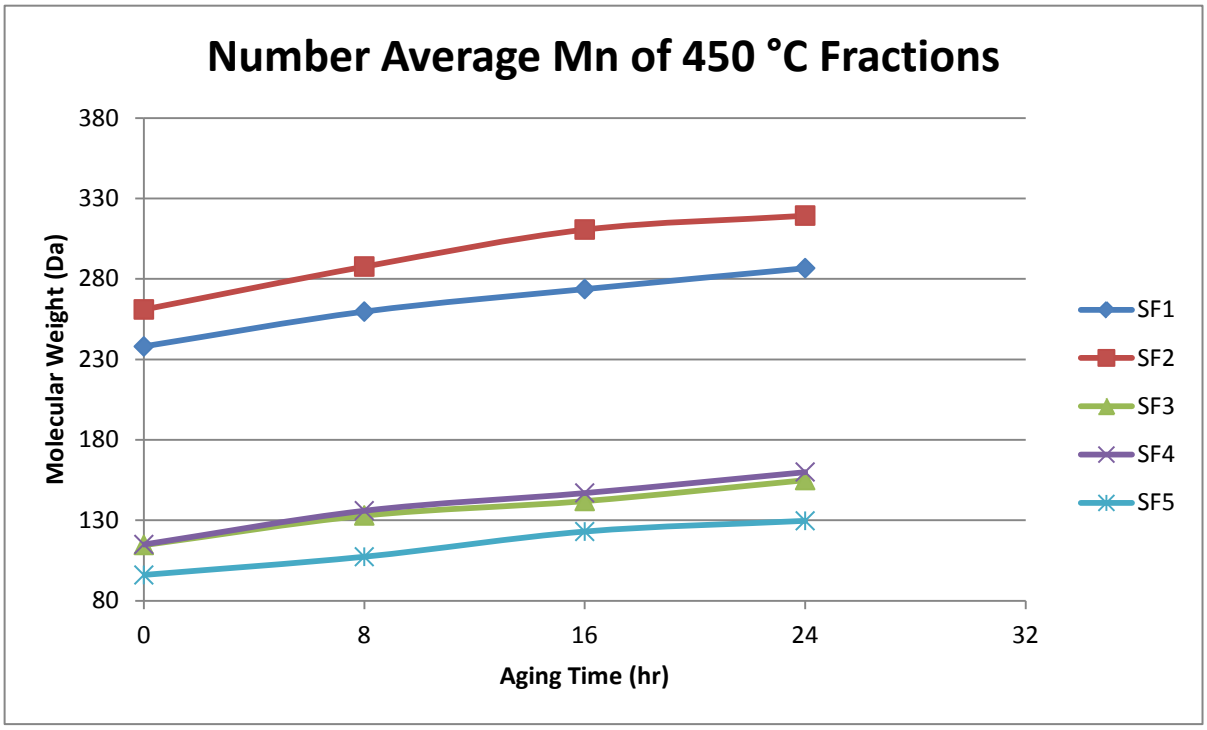

Figure 12. Number average molecular weight of fractions produced at 450 °C

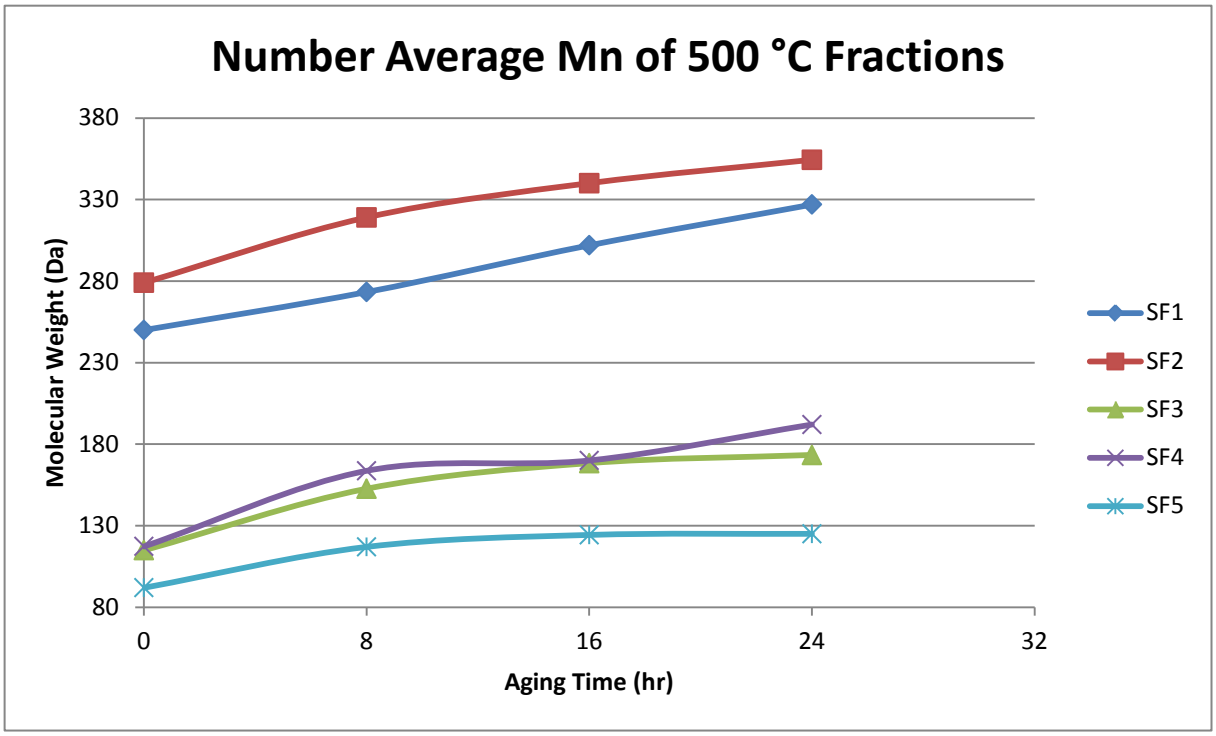

Figure 13. Number average molecular weight of fractions produced at 500 °C

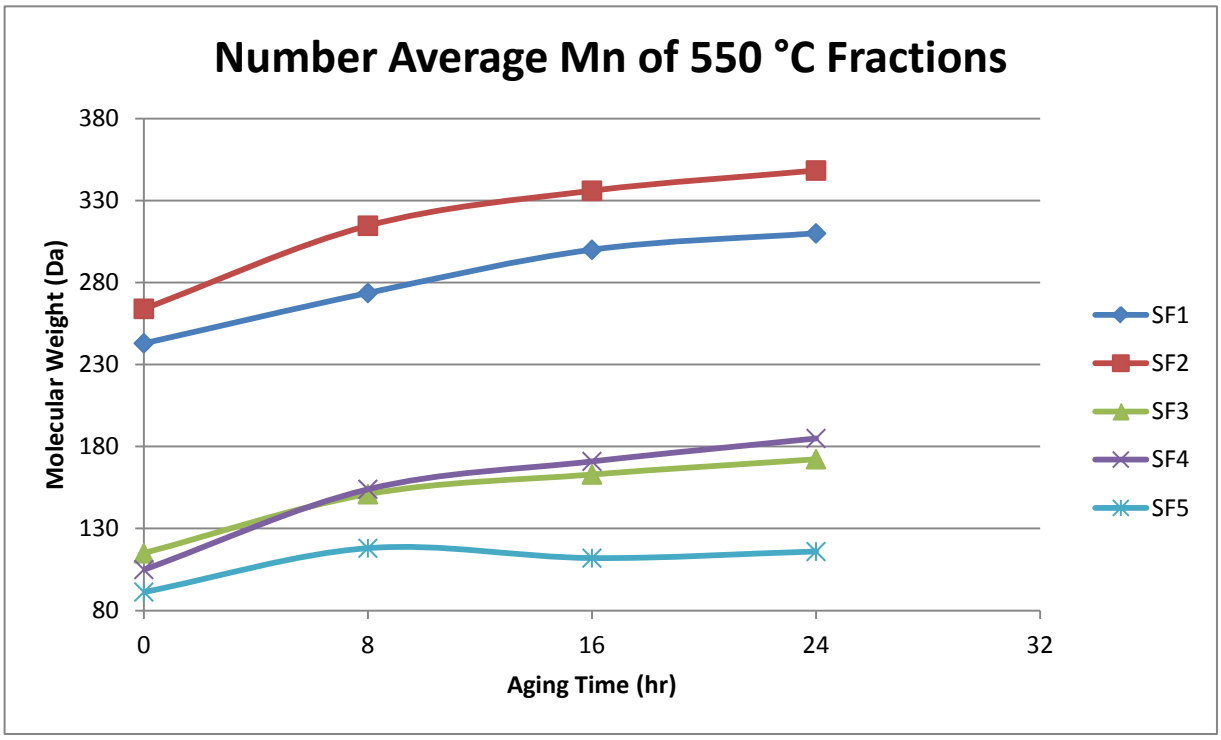

Figure 14. Number average molecular weight of fractions produced at 550 °C

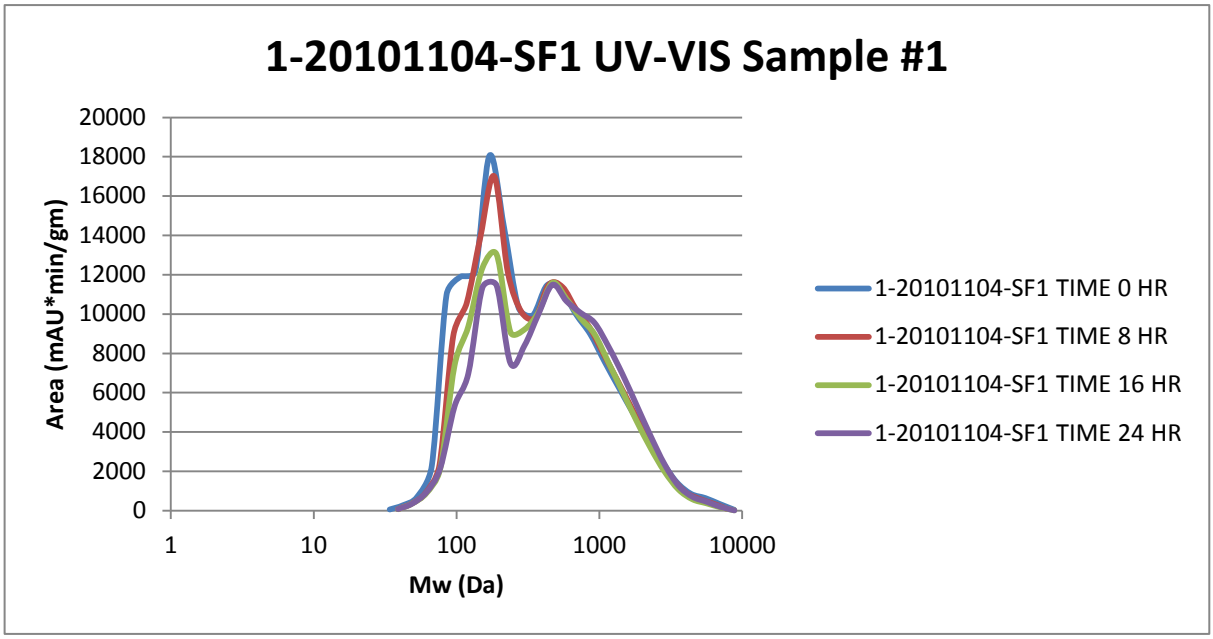

Figure 15. Molecular weight distribution SF1 produced at 400°C for different times during accelerated aging

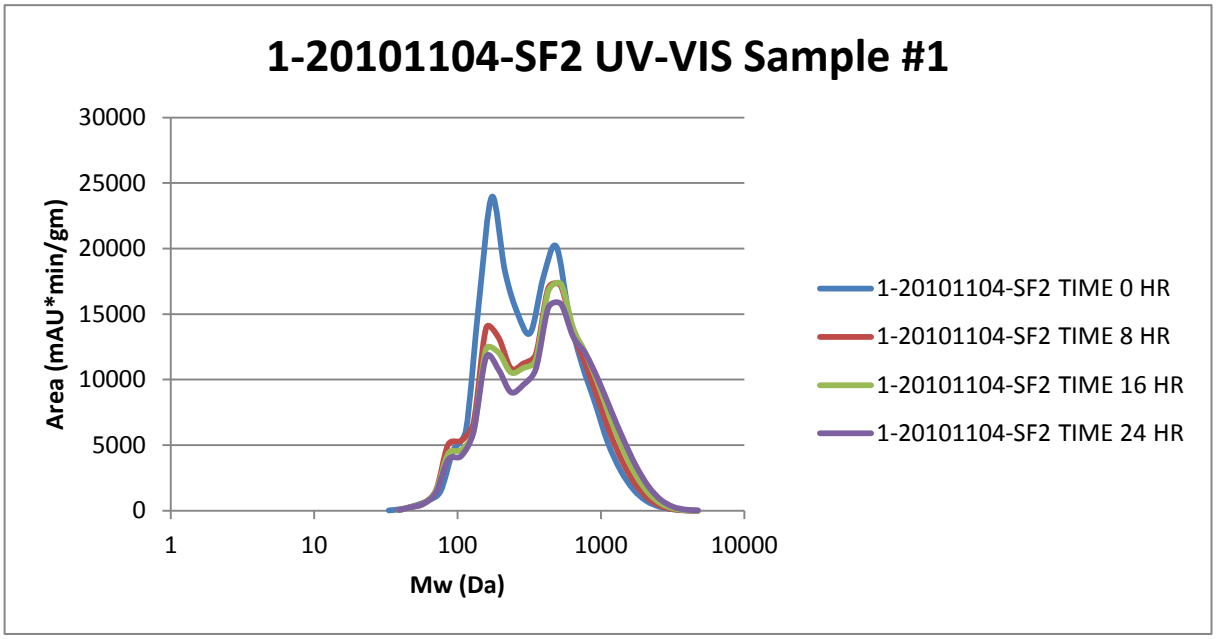

Figure 16. Molecular weight distribution SF2 produced at 400°C for different times during accelerated aging

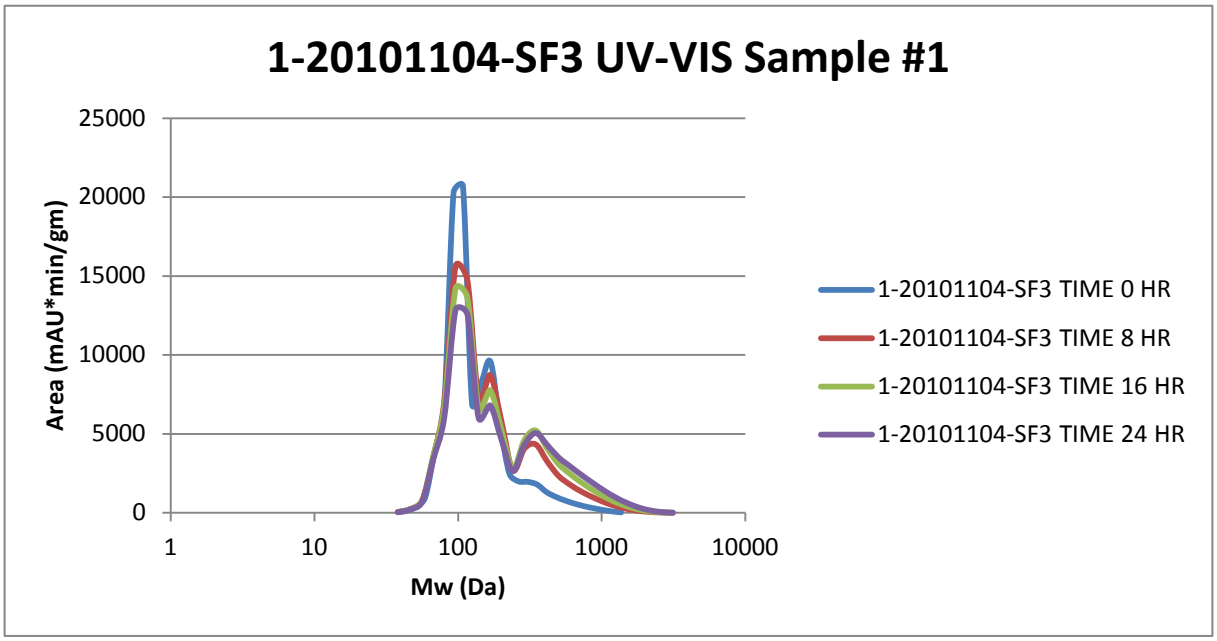

Figure 17. Molecular weight distribution SF3 produced at 400°C for different times during accelerated aging

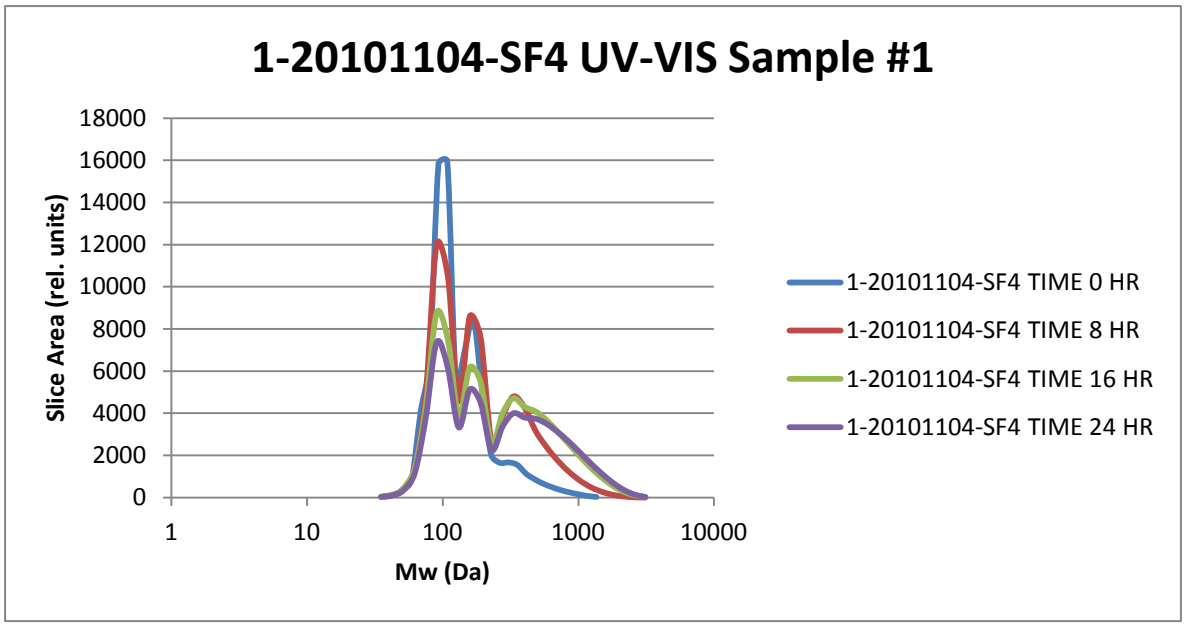

Figure 18. Molecular weight distribution SF4 produced at 400°C for different times during accelerated aging

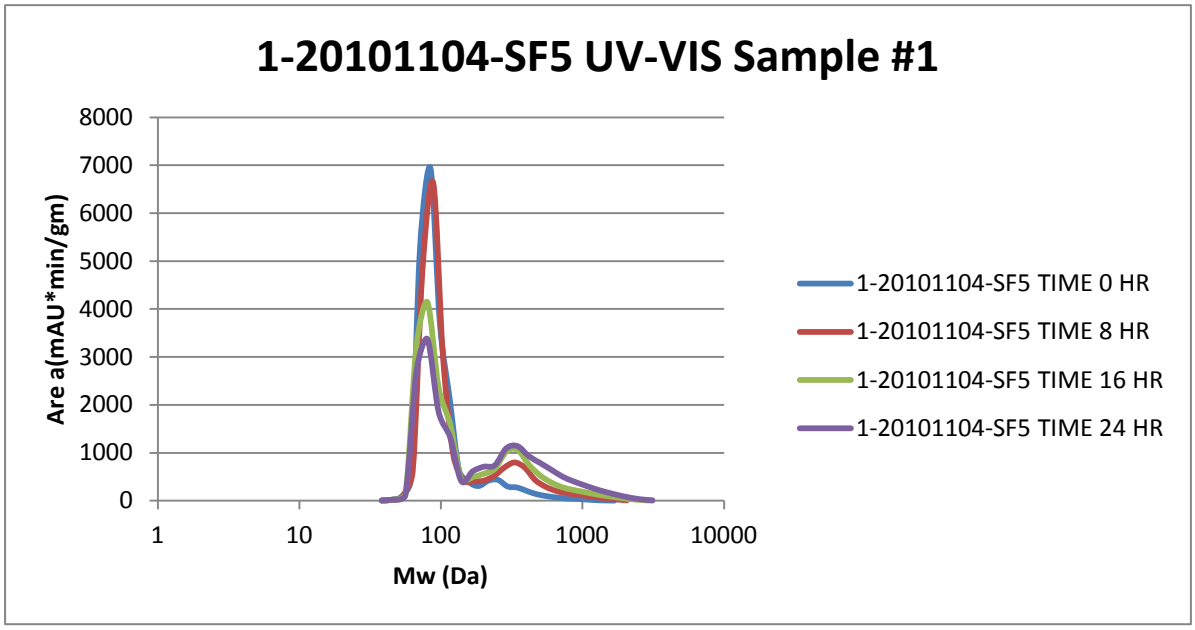

Figure 19. Molecular weight distribution SF5 produced at 400°C for different times during accelerated aging

Molecular weight distributions for stage fractions generated at 400°C as a function of time during accelerated aging tests are shown in Figures 15-19. These clearly show shifts from presumably monomeric phenols (around 100 Da) at early times to what is thought to be phenolic oligomers with molecular weights as high as 10,000 Da. Interestingly, a series of peaks in molecular weight are observed that evolve with time, suggesting the formation of a distinctive succession of monomers, dimers, and trimers that merge into large oligomers with time.

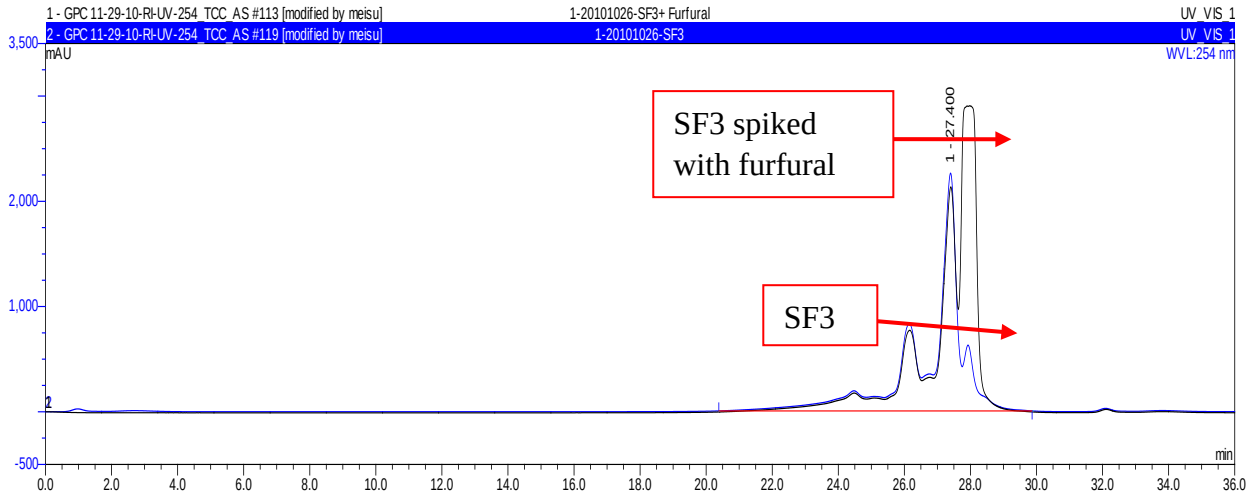

Figure 20. GPC chromatogram overlay of SF3 and SF3 spiked with furfural

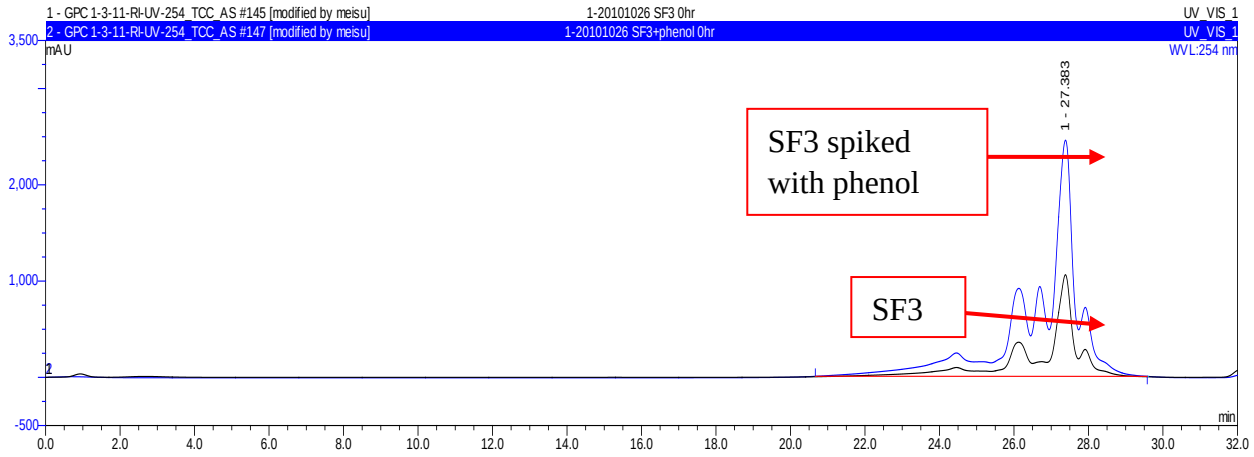

Figure 21. GPC chromatogram overlay of SF3 and SF3 spiked with phenol

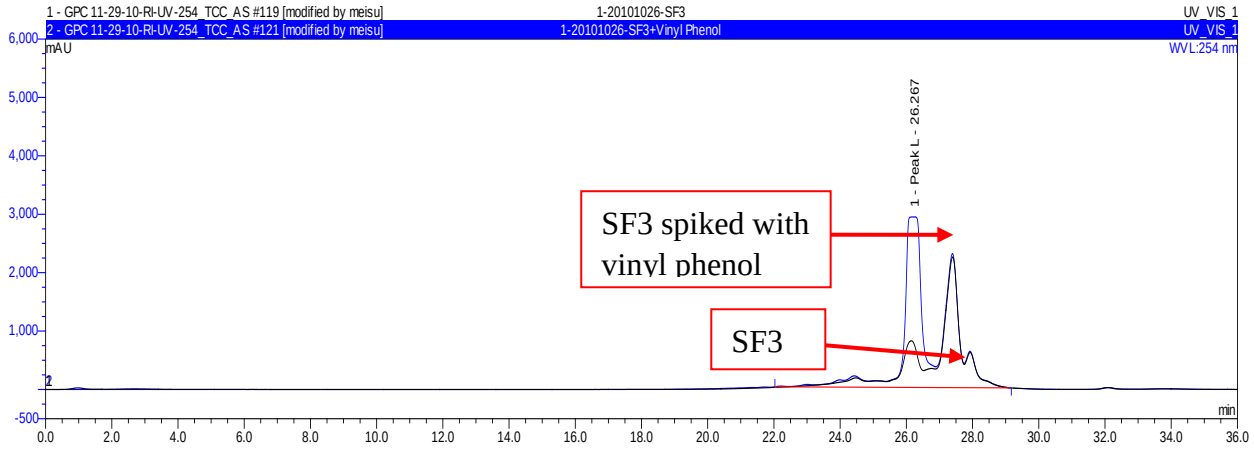

Figure 22. GPC chromatogram overlay of SF3 and SF3 spiked with vinyl phenol

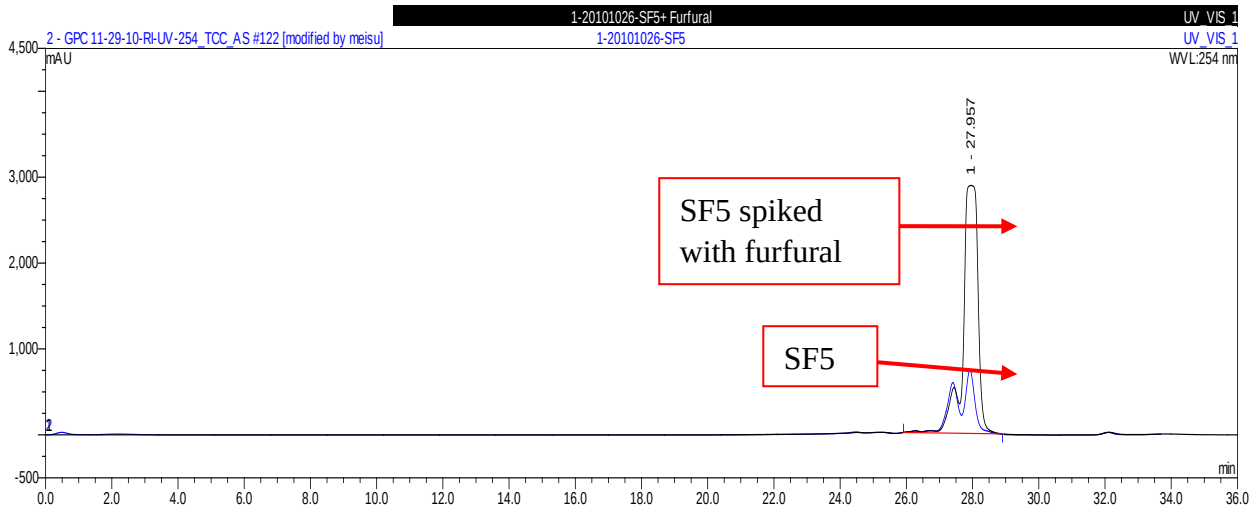

Figure 23. GPC chromatogram overlay of SF5 and SF5 spiked with furfural

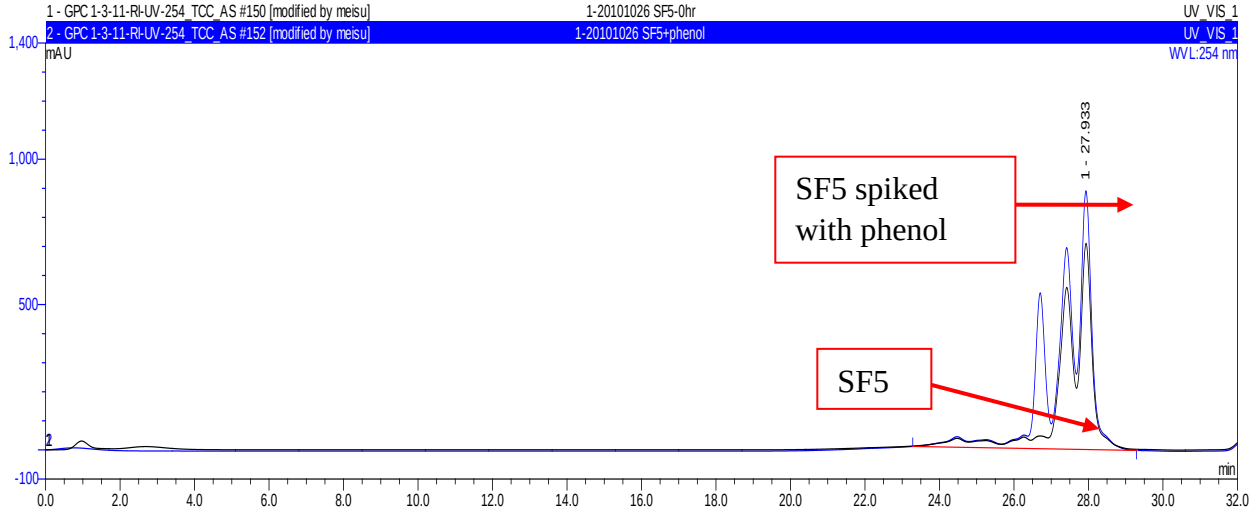

Figure 24. GPC Chromatogram overlay of SF5 and SF5 spiked with phenol

Stage fractions were spiked with some monomeric phenol derivatives and aldehydes for identifying the peaks (Figures 20-24) and these experiments show that:

1) Major peaks in SF3, SF4 with molecular weight 93 and 84 Da could be monomeric phenol and furfural derivatives.
2) One of the major peaks in SF5 could be furfural derivative and it looks like this fraction doesn't have any phenolic monomers.
3) The peak at 168 Da in SF3 & SF4 could be some monomeric substituted phenols and vinyl phenol derivative.

These experiments clearly show that the fractionating condenser train is efficiently separating monomeric phenols and aldehydes in stage fractions 3, 4 & 5. As a majority of monomeric phenols are present in SF3 & SF4 they are showing more aging compared to other fractions. In the same way SF1 & 2 have less monomers and have most of the dimer,

trimers and oligomers, and they are showing less aging. All these results clearly show that the reactive species in bio-oil causing aging are phenol, substituted phenols, vinyl phenol derivatives and aldehydes and ketones (more possibility for furfural derivatives according to molecular weight).

The second major activity conducted during Task 3 dealt with upgrades made the pyrolysis system. A number of system modifications were completed that improved the reliability of the fast pyrolysis system. These modifications were performed on the feed system, the reactor, the cyclones, and the condensing train. The following paragraphs contain a detailed account of each modification.

In the past, the knife gates in the feed system did not seal completely because biomass became lodged in the gate seat during biomass unloading and loading operations, thus preventing a complete seal. Without an adequate seal, the feed system could not be operated in a continuous fashion. A batch method was used for refilling the lower metering hopper during which the reactor sweep gas was stopped. In order to correct this problem, nitrogen purges were installed on the feed system knife gates. These purges allowed nitrogen to blow biomass out of the gate seat during operation. This modification is complete, and the knife gates now hold a satisfactory seal. As a result, the metering hopper can be refilled while the pyrolyzer reactor is running resulting in higher daily bio-oil yields and reduced system downtime.

The cyclones have plugged frequently in the past. In order to unplug them, the char catch was removed during a run and a brush was inserted into the cyclone to dislodge any residual char. A problem with this method is that char was reinserted into the vapor stream during the cleaning, and the entrained char was then carried to the condenser train. A better solution has been devised for this problem. A short blast of nitrogen is shot into the char catch of the plugged cyclone which slightly disturbs the lodged char, allowing it to fall into the char catch. Recently, a solenoid value and a pressure transducer have been installed that automatically purges the cyclone when the pressure transducer detects that it is plugged. This new automatic cyclone purge has been tested, and proven successful.

One problem encountered with this system was the loss of voltage over time in the ESPs. In order to keep the system operating, the ESP electrode would need to be cleaned every 3-4 hours. This was not only interrupting trials, but was limiting the biomass feed rate below capacity. After consulting the literature, a current vs. voltage test determined that corona onset was not occurring until about 25 kV (see Figure 1) whereas typical ESP's achieve corona at much lower voltages.

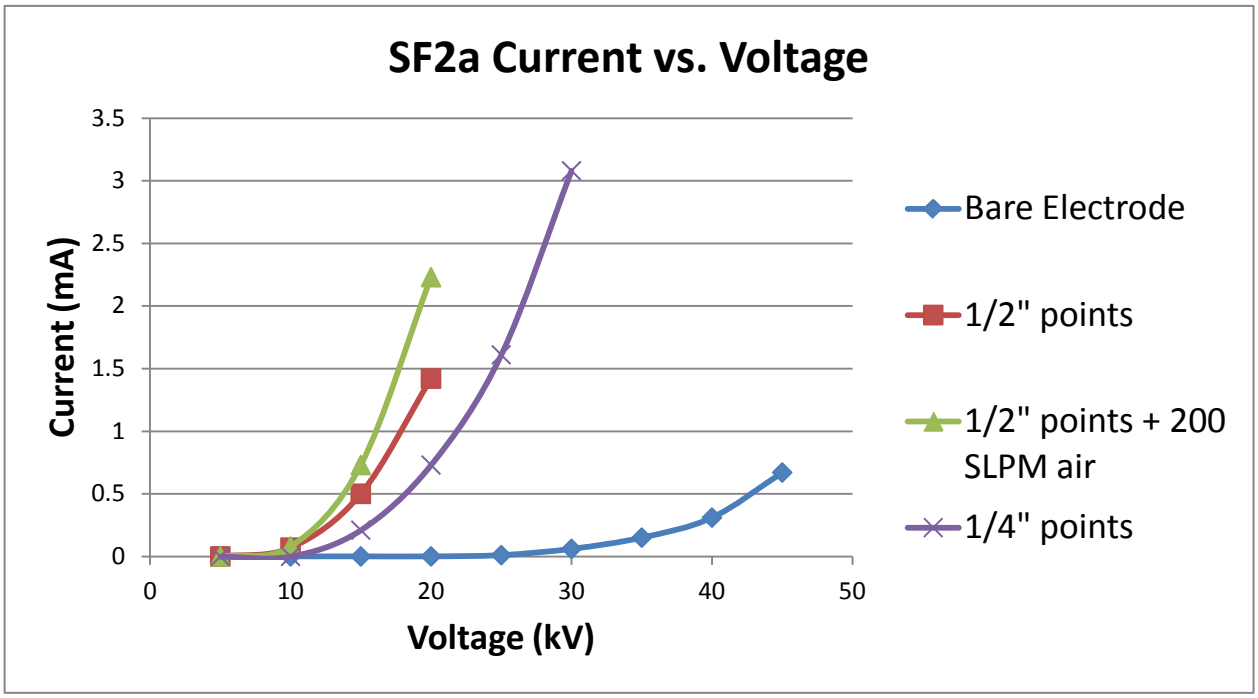

Figure 1. Measured current vs. voltage before and after electrode modifications

The first ESP electrode was modified with barbs (see Figure 2) in an effort to improve the corona, as suggested by the literature. Barbs extending both ½" and ¼" from the electrode were tested. The ½" barb with 200 SLPM of air added through the system was also tested. After measuring the current vs. the voltage for each condition, as shown in Figure 2, a ¼" barb was selected for further testing. Corona onset occurred between 10-15 kV, and produced a much larger current at a lower voltage point.

Figure 2. Modified ESP electrode after trial run

Preliminary results from a trial run with the ¼" barbs demonstrated an increase in both sustained feed rate and bio-oil yield. Prior to this test, the maximum biomass feed rate that could be maintained ranged between 4.5-5.5 kg/hr. A feed rate of 5.9 kg/hr was maintained after modifying the ESP electrode. The average total bio-oil yield for 2009 trials was 55.89%. After the electrode modification, a yield of 62.2% was observed. The effectiveness of the first stage was so much improved that little aerosol carried over to the

second stage ESP as evidence by the small amount of oil collected in this stage. The last ESP (SF4) was also modified by installing short barbs on the electrode.

New Teflon lids have been constructed for each of the three electrostatic precipitators. In the past, bio-oil has condensed on the underside of the ESP lids, allowing for electricity to short circuit across the lid from the electrode to the wall. The new lids use a NPT threading system that does not allow for electricity to arc across the condensed bio-oil. Because of this improvement, the system can be run for at least 8 hours without an unscheduled shutdown. This time was not attainable before this improvement was made. The ESPs can now be run at maximum power supply capacity, meaning that more current passes through the electrode which results in a more efficiently operated ESP. To illustrate this point, the electric corona field within each ESP is so large since the lid modifications, that each ESP generates enough heat to overshoot their desired operating temperatures by 20 C. This means that each ESP provides the heat internally instead of required external heat tracing. Another evidence of improvement can be seen on the electrode itself of the first ESP (SF2a). In the past, the electrode was completely covered with bio-oil after a daily run. After the lid modifications, only the bottom half of the electrode is covered with bio-oil, with the top half remaining clean. This indicates that all of the aerosols are being collected in the bottom half of the ESP due to the increase in operating efficiency corresponding to the high voltage and current draw. The electrode of the first ESP is pictured below.

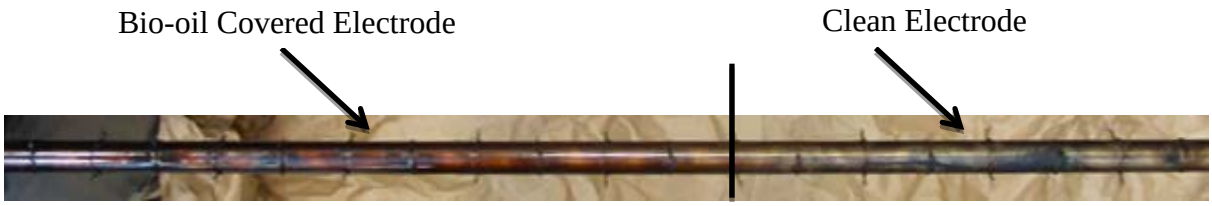

In the past, stage fraction 4 (SF4) was assumed to be isothermal. Collected temperature data has proven that it is not isothermal. In fact, SF4 is collecting compounds which should only be collected in SF5, such as water and organic acids. This stage fraction has been heat traced using an external temperature control.

In order to support new heating zones and other future system modifications, an additional controls cabinet was designed and built. The additional controls cabinet is necessary because the current cabinet contains no room for expansion.

Numerous programming changes were made in the control software. These changes included software interlocks, visible and audible alarms, startup and shutdown sequence controls, and changes to the operator interface. These programming modifications will reduce operator error, system downtime, and improve system reliability.

Task #4: Laser Diagnostics for Vapor Filtration and Bio-Oil Recovery

Table 4.1 below summarizes the various diagnostic techniques considered for use in the research work. The laser source is a compact, portable Nd:YAG laser with output at either 532 nm or 266 nm. The various excitation schemes and the measured parameters of interest in the pyrolysis system are listed in the table. For reference, note that the visible range of laser radiation is typically from 400 – 700 nm, with wavelengths below 400 nm being in the ultraviolet and wavelength above 700 nm being in the infrared. Of these techniques, we have focused on three that can be used for differentiating aerosols and char particles, as well as measuring elemental concentrations of N, O, C, and H. These techniques include laser scattering, laser induced incandescence, and laser-induced breakdown spectroscopy. All are at 532 nm but differ with regard to timing of detection and laser excitation energy.

Briefly, laser scattering will be very weak from vapors but can be used to detect aerosols and particles. However, scattering cannot distinguish between aerosols and particles of the same size. Scattering occurs immediately after excitation and can be detected within 10 ns of the laser pulse. Hence, by delaying the detection in time, it is possible to detect laser heating of particulates, which results in detectable laser-induced incandescence (LII). This laser heating is specific to solid particles and will not occur from aerosols. Finally, by increasing the laser energy even further, it is possible to perform laser-induced breakdown spectroscopy (LIBS) by breaking the molecular bonds to reveal signals specific to different elemental species (N, O, C, and H). In the presence of particulates, the breakdown occurs at lower laser energy but does not seem to perturb the signal. Rather, the breakdown propagates quickly through the vapor and reveals the elemental composition of the vapor phase rather than the particulates or aerosols. However, the selection of laser energy and timing of detection are key to realizing quantitative measurements for each particular environment, especially in the presence of non-vapor species. Hence, the main hypothesis of this work is that *in situ* laser diagnostic techniques can be used to provide key information on the complex, multiphase pyrolysis products for analysis of important processes such as hot-vapor filtration and bio-oil recovery.

The planned activities encompassed three main efforts, including analysis of filtration efficiency for different types of granular materials compatible with hot-vapor filtration, primarily using scattering, and studies of pyrolysis products using scattering, LII, and LIBS.

Filtration Studies. The goal of the filtration study was to (1) provide validation measurements for comparison with a CFD model being developed by collaborators on the project and (2) enable methods to different particles and aerosols in pyrolysis flows. The physical arrangement of the filtration system for comparison with CFD calculations is shown along with the laser and camera detection systems in Figure 4.1.

Table 4.1. Summary of diagnostics characterization for operation with bio-oil aerosols and particulates.

Laser Excitation (nm)	Signal Range (nm)	Detection Band (nm)	Measured Parameter
532	532	532	Scattering of Aerosols and Particles (Sized 0.5 – 50 μm)
532	400 – 900	400 – 500	Laser-Induced Incandescence of Soot Primary Particles (sized 30-100 nm)
266	300 – 500	300 – 500	Aerosol Fluorescence (Sized < 1 μm)
532	200 - 1100	200 - 1100	Laser-Induced Breakdown for Elemental Analysis of Aerosols and Particles (Sized 0 – 50 μm)
532 (x2)	532 (x2)	532 (x2)	Particle Image Velocimetry (Sized 1 – 50 μm)

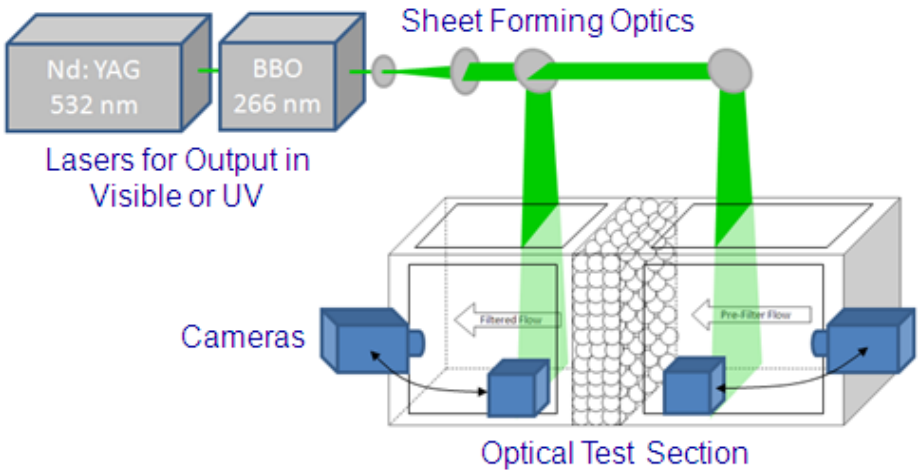

Figure 4.1. Schematic of test set up to be used for comparison with numerical modeling studies of hot vapor filtering.

In the test facility shown in Fig. 4.2(a), a closed flow loop is utilized to recycle particulates and aerosols, and the removal rate is measured over time. This is similar to the procedure used in the CFD calculations in which a relatively thin layer of filter material (1 to 2 cm thick) is simulated to reduce computation time and continuous recycling of the particle-laden media provides a measure of the time (and hence filter path length) required for various levels of filtration. Results using this test facility are shown in Fig. 4.2(b), where the decay of laser-light scattering from particles over time is recorded for the case with and without a granular filter (made of 2-mm glass beads).

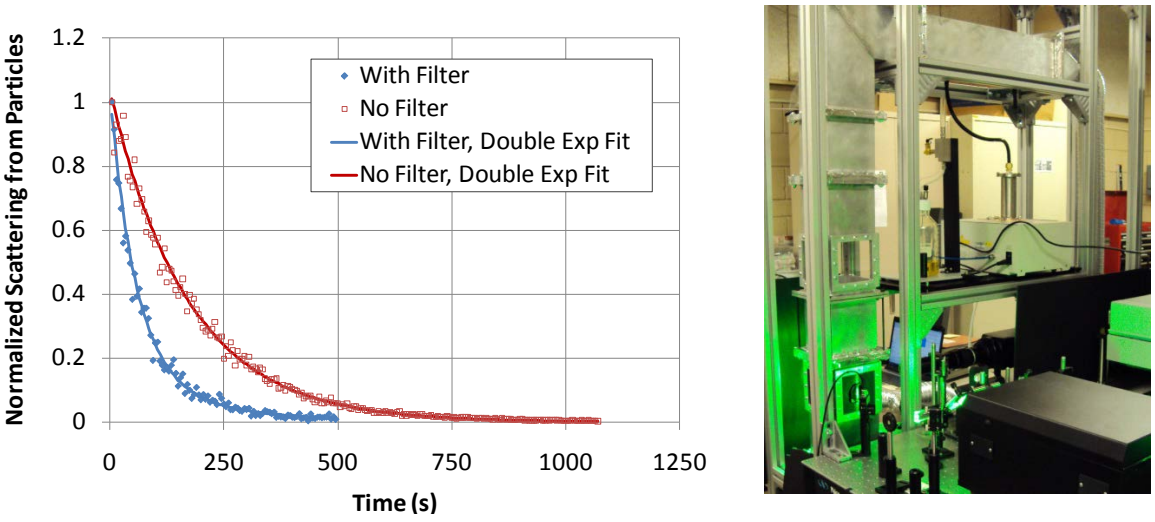

Figure 4.2. (a) Closed filtration loop and (b) sample measurements of filtration time.

The decay for the case without a filter occurs as particles coat the walls of the test section. When the filter is added, the decay rate increases significantly, as expected. Interestingly, the decay rate does not fit a single exponential decay, but is accurately modeled with a double exponential function for cases with and without the granular filter. The double exponential functions used to fit the data are shown below.

$$\text{Signal with No Filter} = 0.14\exp(-0.005t) + 0.9\exp(-0.006t)$$
$$\text{Signal with Filter} = 0.14\exp(-0.005t) + 0.9\exp(-0.0175t)$$

These results indicate that the decay rate of particles is more rapid initially, and that there are two primary mechanisms that are filtering particles in the system. However, as shown in the equations above, the difference between the case with and without the granular filter can be represented by the change in only one parameter, namely a three-fold increase in the time constant of the second exponential term (from 0.006 to 0.0175). Another important result of the current tests is that the decay rate for aerosols is unaffected by the presence of the filter. While the data are not shown here, aerosol scattering diminished at the same rate regardless of whether a granular filter was present in the flow, meaning that it is possible to remove particles while allowing the passage of aerosols through the filter.

If corrections are made to account for natural losses in particulates due to agglomeration on surfaces of the circulating particle flow tunnel, the filtration coefficient can be calculated as a function of filter bed depth to accommodate comparisons with numerical predictions. Here, the filtration efficiency was taken as the difference in signal intensity between the pre- and post-filter sections, which is then divided by the signal intensity in the pre-filter test section. Because the seeded particles were monodisperse, the signal intensity from laser scattering is proportional

to the number density of particles. The plot in Fig. 4.3 (a) shows the cumulative filtration efficiency as a function of time, wherein for each successive time period, the total number of captured particles to that point are divided by the total number released. As evidenced by these data, the trend is similar to that which we see in the models, by which there is a rapid ramp up, followed by a slow approach to steady state. The filtration efficiency increases as the bed depth increases, until gradually approaching a filtration efficiency of unity, as expected. The plot in Fig 4.3 (b) shows the average filtration efficiency as a function of bed depth. From this, a filtration coefficient can be calculated as:

$$k = \frac{-\ln(1-\eta)}{d/u}$$

where η is the efficiency, d is the bed depth, and u is the velocity of the flow.

Because there is an inherent filtration in the system due to agglomeration on walls, an effective bed depth for the cold flow chamber was calculated first by determining the filtration coefficients for each bed depth, as indicated above. Because the filtration efficiency should be zero without beads, the effective bed depth for the zero bead condition was iterated until the linear fit line, forced to intercept at the origin, had the best fit. As a check to the effective bed depth, the extrapolated filtration coefficients were used to plot expected filter efficiencies against the true filter efficiencies with the added effective bed depth, and were found to be in good agreement.

The aerosols for the tests conducted above were generated with an instrument designed to produce very small oil droplets (of the order 0.3 to 0.5 microns. The particles were derived from char collected from previous pyrolysis operations and aerosolized using a fluidized bed with constant particle concentration. Two different commercial particle sizers were used to characterize the size distribution of this char, including a process particle counter (PPC) and aerodynamic particle sizer, as shown in Figs. 4.4 (a) and (b), respectively. The distribution shows an abundance of small particles with some larger particles near 10 microns. This is somewhat smaller than expected, but still useful for testing. However, both particle counters provide similar distributions, providing some confidence in the distribution. Unfortunately, it is difficult to implement such counters *in situ*, and it is moreover impossible to differentiate between small particles and aerosols within the distribution, requiring product analysis with repeated and expensive test runs and preventing online optimization of the pilot scale pyrolyzer.

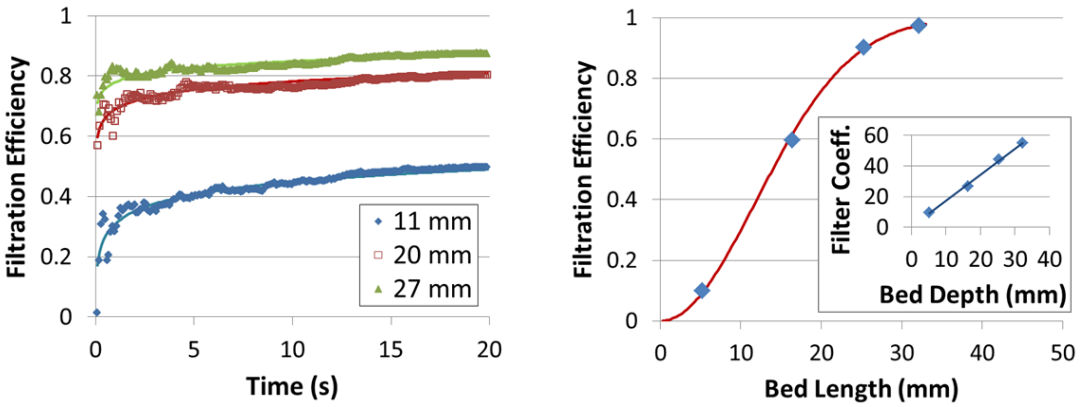

Figure 4.3. (a) Filtration efficiency vs. time for 3 bed depths showing logarithmic progression, and (b) filtration efficiency vs. bed depth; inset is filtration coefficient with linear fit.

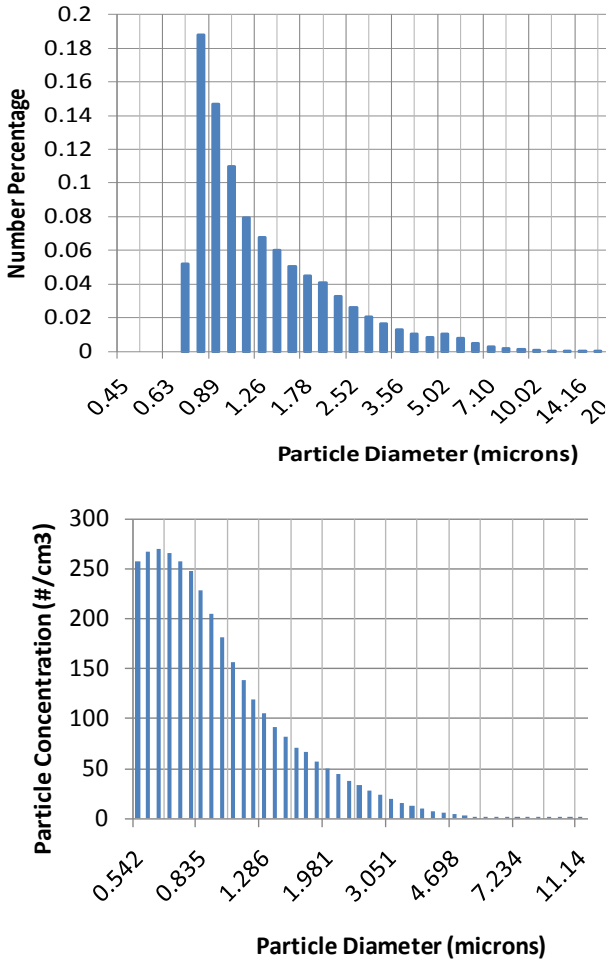

Figure 4.4. Particle size distribution collected using (a) a process particle counter (PPC), which relies on laser scatter to measure size distribution, and (b) an aerodynamic particle sizer.

As noted earlier, to differentiate between particulates and aerosols, it is possible to employ laser-induced incandescence, which physically heats particles to the point of incandescence (LII), as the name suggests, followed by detection with a camera. This allows imaging of the flow field. In the current work, a small scale pyrolyzer was constructed to demonstrate the feasibility of performing LII as well as scattering to detect particles and aerosols, respectively. The pyrolysis reactor consisted of pine biomass that was ground and packed into a stainless steel tube and suddenly exposed to 35 standard liters per minute (SLPM) of nitrogen flow at 540 °C to simulate fast pyrolysis. Results of LII and scattering tests are shown in Fig. 4.5, with the pyrolysis products flowing from bottom to top. As shown in Fig. 4.5(b), the LII produces an image of particles in the flow, which appear discrete as they have lower number density that the aerosols. Fig. 4.5(c) shows an image of scattering from aerosols. Because the aerosols are smaller than the resolution of the camera and have very high number density, they produce a more uniform image as compared to the particles. The laser energy for the scattering image was reduced significantly so that no LII could contaminate the image. For this reason, and because the aerosols have very high number density, it is possible to scattering from aerosols but not particles. These results demonstrated the capability to differentiate between biochar particles and aerosols in a pyrolysis environment. Hence, this approach can be used to assess the effectivess of hot-vapor filtration for fast, online optimization of the pyrolysis system.

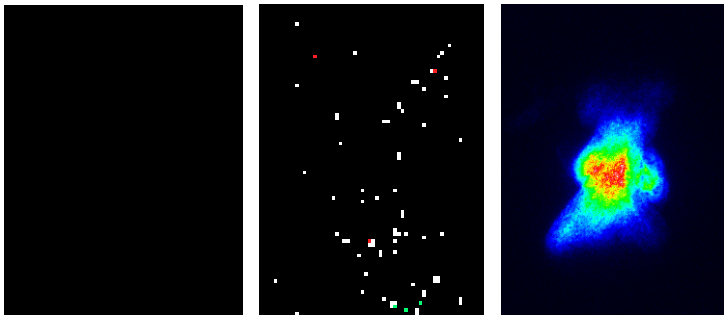

Figure 4.5. (a) Background image, (b) image from LII, and (c) image from laser scattering from the products of a small-scale pyrolysis reactor.

Elemental Analysis for Bio-Oil Recovery. Elemental analysis is of particular interest for detecting the composition of the pyrolysis products at various stages of bio-oil recovery. For example, it can be used to detect the prevalence of water versus other light gases during condensation. In the current work, the ability to determine the relative species concentrations of N, O, H, and C was demonstrated using laser-induced breakdown spectroscopy (LIBS).

To determine the effectiveness of LIBS for measuring the vapor phase within the pyrolysis reactor, experiments were conducted with various test gases and the results compared for data collected with and without aerosols and particles within the probe volume. A laminar co-flow test section was devised to deliver CH4 sheathed in N2 to simulate the presence of light hydrocarbons within a low oxygen environment. A

532 nm Nd:YAG laser was used to produce a plasma in the flow for elemental analysis. The laser was focused just above the outlet of the co-flow device, and at the focal point of a spherical lens. When the plasma is formed, the spherical lens captures the emission, collimates the light, which is then coupled to a lens focusing on the slit of a 303-mm spectrometer. For calibration measurements, pure nitrogen in the sheath flow was delivered at 10 slpm, and CH4 was introduced at intervals of 0.25 slpm up to 4 slpm. For each concentration, 1000 time-delayed spectra were collected with an exposure time of approximately 1 microsecond at 10 Hz and averaged. The time delay minimizes the broad continuum LIBS background. As the nitrogen concentration is typically known, the concentrations of species are determined relative to N.

The data in Fig. 4.6 (a) show the LIBS signal for differing concentrations CH4. Initially, at a CH4 mass fraction of 0.008, the peak near 656 nm is comparable to that of the other features in the spectrum. As the mass fraction of CH4 is increased, the central peak, consisting primarily of a strong H (I) transition identified in the NIST spectral database, increases significantly up to a mass fraction of 0.184. Meanwhile, the other peaks in the spectra, consisting of nitrogen lines identified in the NIST spectral database, remain relatively constant, except that they increase slightly as the baseline of the central peak increases. To determine whether these data could be used for quantitative analysis, the measured peak height of the H (I) peak is plotted as a function of the CH4 mass fraction in Fig. 4.6 (b). The linearity of the LIBS signal indicates that it is possible to extract quantitative information about vapor elemental composition. Absolute measurements of concentration are possible by comparing the strength of the central peak to that of a calibrated nitrogen peak, since the nitrogen concentration in the pyrolysis reactor is more or less known. In fact, when taking the ratio of the H (I) peak to that of the N (I) peak near 653 nm, that ratio varies with a standard deviation of about 5% over each 10-shot average (i.e., for a 1-second averaging period) during the 1000-shot collection time. Hence, it is possible to achieve real time, *in situ*, elemental analysis using this approach.

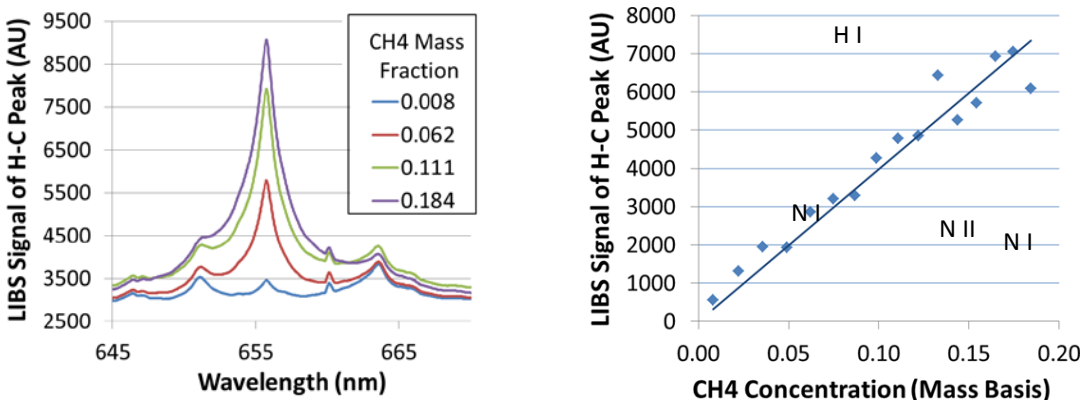

Figure 4.6. (a) LIBS Spectrum showing increase in H relative to N with CH4 addition, and (b) calibration for in-situ concentration of hydrocarbon gases showing excellent linearity.

Figure 4.7 shows spectra obtained in a bio-oil laden flow showing the signals of elemental hydrogen, oxygen, carbon, and nitrogen. The spectra are collected at three different wavelength regions. Later, a new spectrometer allowed simultaneous detection of all species.

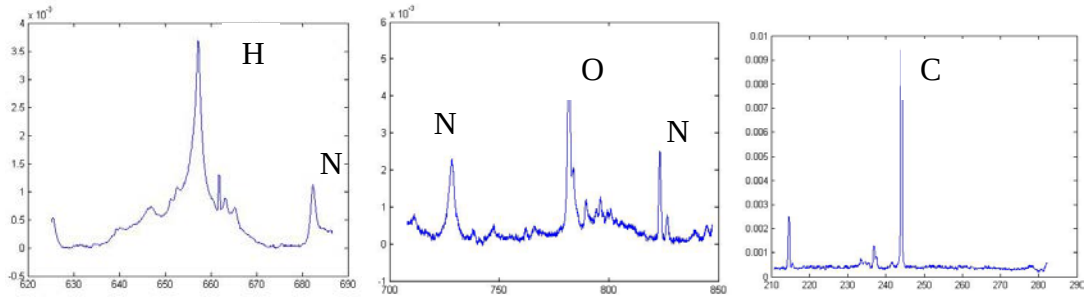

(a) (b) (c)

Figure 4.7. Plots of intensity (arb. Scale) vs. wavelength for LIBS signal showing peaks of (a) hydrogen, (b) oxygen, and (c) carbon.

Figure 4.8 shows sample calibration curves for carbon and oxygen versus mass fraction. These data show repeatable results, with the nonlinearity to be removed upon normalization with nitrogen.

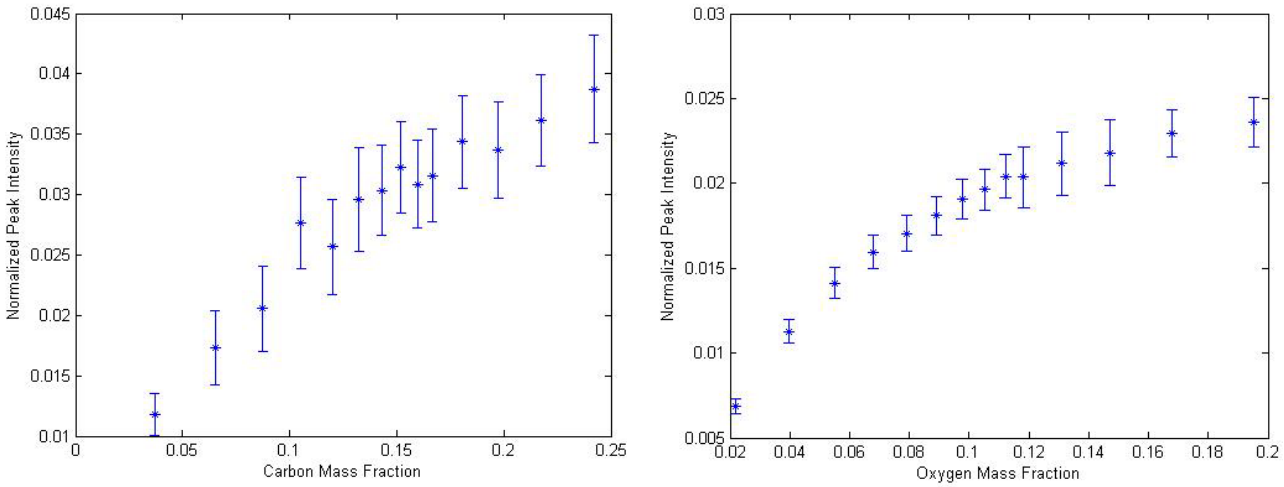

(a) (b)

Fig. 4.8 Plots of background subtracted, normalized intensity as a function of (a) carbon mass fraction and (b) oxygen mass fraction from LIBS spectra.

The data in Fig. 4.9 shows the processed oxygen signal after normalization with nitrogen. The relative oxygen signal is linearized as a function of oxygen mass fraction, as shown in Fig. 4.9. This is critical because variations in laser intensity and the strength of the breakdown can lead to increased uncertainty in the elemental concentration measurements.

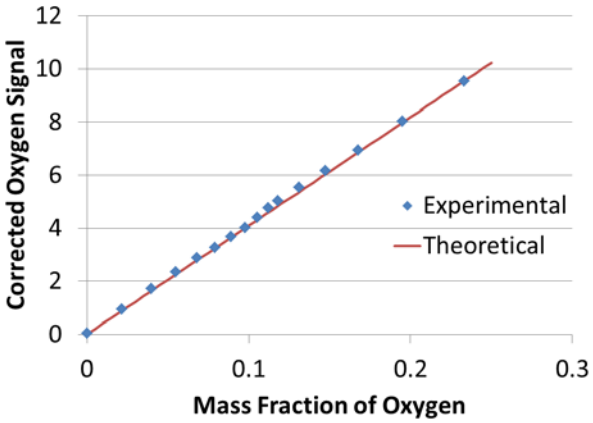

Fig. 4.9 Corrected oxygen signal after final normalization with nitrogen.

To obtain all four species simultaneously, an echelle spectrometer was employed, which allows detection from 240 to 1000 nm through a special arrangement utilizing a two-dimensional detector. As shown in Fig. 10, C, H, N, and O species can be detected, with a close-up of the carbon peak showing the signal-to-noise ratio that can be achieved. These data were collected in the small-scale pyrolysis system described earlier and confirms the presence of hydrocarbons and water vapor in the products.

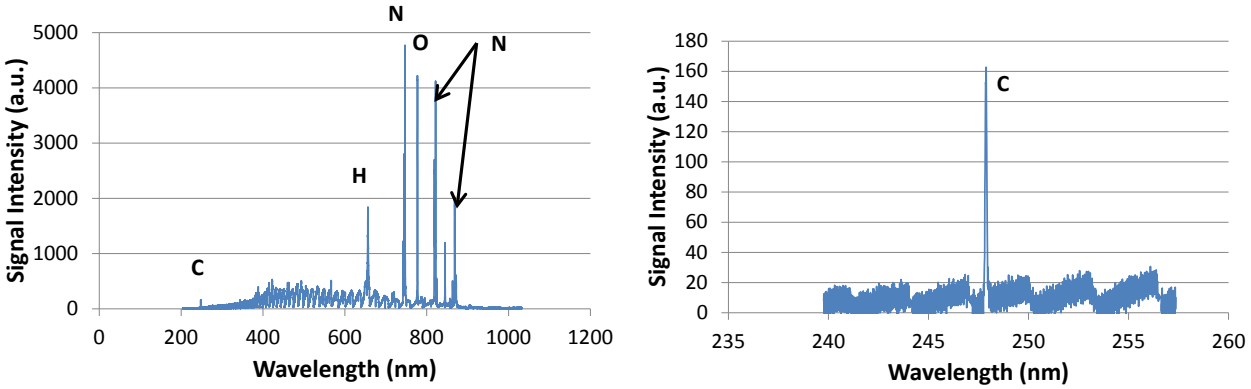

(a) (b)

Fig. 4.10 Simultaneous spectra of (a) C, H, N, and O species and (b) close-up of C element using echelle spectrometer in a pyrolysis product flow.

These data thus far indicate that it will be possible to differentiate regions with high levels of water vapor versus light hydrocarbons. These data can also be collected in the presence of char particles. In combination with scattering and laser-induced incandescence, these techniques will be used to characterize the in-situ particulate, aerosol, and vapor concentrations.

Final work focused on transitioning the diagnostic system to the pilot-scale pyrolysis facility for studies of bio-oil recovery. An optically accessible pipe was placed in line at the pilot scale pyrolysis reactor at the Bio Century Research Farm, as shown in Fig. 4.11. The test section was placed between the filtering cyclones and the first condensation section. A 532 nm pulsed laser (SOLO PIV IV, New Wave Research) was mounted to the frame of the reactor, and a train of mirrors (Fig. 4.12) was placed to direct the beam into the test section. A combination of UV sensitive cameras (Princeton Instruments) and the eschelle spectrometer coupled with an ICCD (Andor Mechelle, Andor iStar ICCD) were used to detect signal in situ.

Fig. 4.11. Photograph of test section designed for insertion into pyrolysis production rig.

Fig. 4.12. Photograph of laser, optics, spectrometer, and camera installed in the pyrolysis oil pilot plant.

Several attempts were made to mitigate the effects of condensation of bio oil on the windows and the buildup of biochar in the optical ports, which made making repeatable measurements difficult. The optical ports were heated to a temperature of 450 degrees Celsius, all surfaces not used for optical access were covered by insulation, and a 3 to 4 SLPM nitrogen purge, heated to 350 degrees Celsius, was plumbed into the optical ports. Optical ports not directly used to image or send a beam through the test section were blocked and insulated. Prior to any heating of the entire pyrolysis system, the optical access section and nitrogen purges were allowed to come to steady state temperature, and the feed rate was slowed to produce fewer aerosols and char.

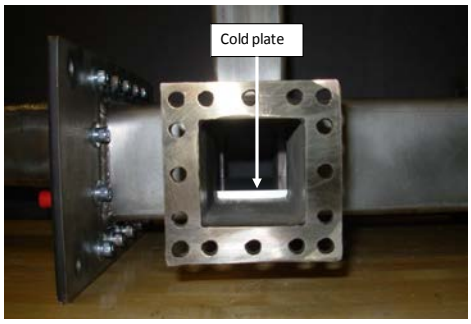

Figure. 4.13. Optical insertion rig for studying bio-oil condensation.

Figure 4.13 shows the test rig designed for insertion into the condensation section of the pilot-scale pyrolysis facility, which includes a cold plate for temperature control. The data in Fig. 4.14 show relative molar concentrations of oxygen (upper) and carbon (lower) in the condensation rig. 6.5 SLPM of nitrogen was used to aerosolize bio-oil, which was heated to 200 C prior to entering the test section. The cold plate was held at 21 C. A 532 nm Nd:YAG pulsed laser (10ns/pulse, 150 mJ/pulse) was focused into the test section using a 200-mm focal length lens mounted to a transverse stage to generate a plasma at varying distances from the cold plate. The LIBS signal was coupled into the spectrometer and an average of 500 shots was used to generate relative concentrations of H, C, and O. These provide a measure of the relative concentrations of bio-oil and other species in the flow for studies of pyrolysis and condensation.

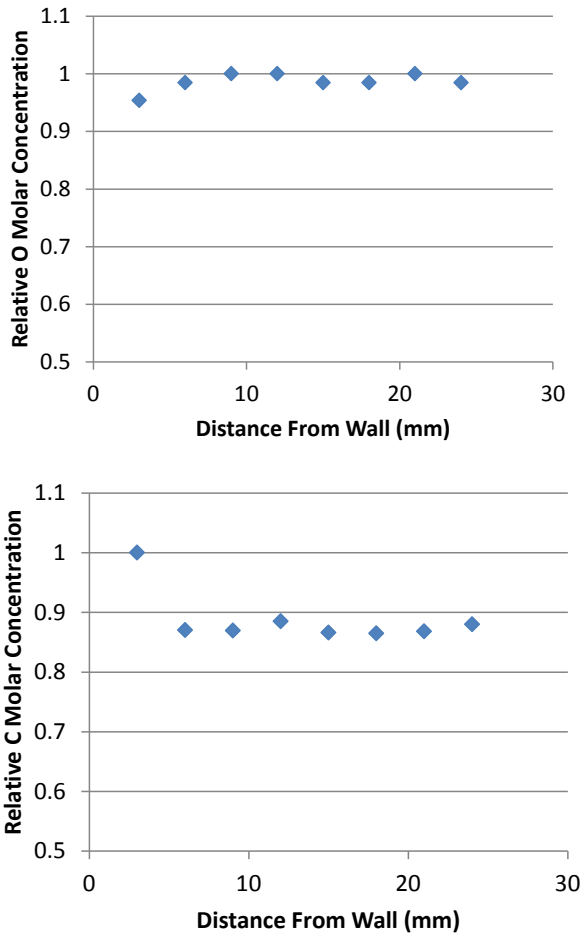

Figure. 4.14. O (upper) and C (lower) relative molar concentrations across simulated bio-oil aerosol.

The data in Fig. 4.15 show plots of H (upper) and C (lower) molar concentrations for a simulated heated flow of water vapor and light hydrocarbons. 15 SLPM of nitrogen was bubbled through acetone then mixed with steam prior to entering the test section. The cold plate used for condensing the gas was held at 57 C. As with the plots above, an average of 500 shots was used to generate relative concentrations of H, C, and O. By quantifying the relative concentration of carbon, these data can be used to determine the concentration of water vapor during condensation. By measuring the spatial distribution of concentrations, it is also possible to evaluate the diffusion of areosols and vapors towards the cold surfaces of the condensation sections of the pilot plant.

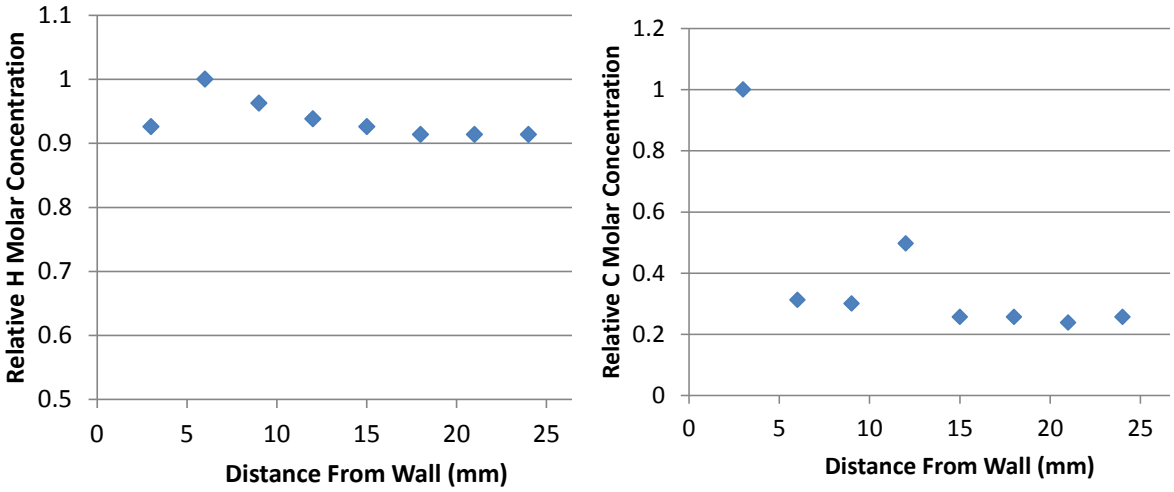

Fig. 4.15. H (left) and C (right) relative molar concentrations across simulated water vapor and light hydrocarbons.

Task #5: Computational Modeling of Vapor Filtration and Fractionating Condenser

The activities in the computational tasks were focused along two directions

I. Development of a CFD model for the entire MBGF system

Approaches used: 2-D simulations of gas flow through an empty filter and filter media were done using ANSYS-FLUENT. The simulations were then extended for filtration of particles through a 3-D packed filter media. The 3-D CFD model developed using ANSYS-FLUENT was validated by comparing simulation results of pressure distribution along the axis of filter with the results obtained from Ergun's equation (Macdonald 1979). Char accumulation rate obtained from 3-D CFD model with Jung et. al (1989) and Qin (2010) models implemented in it gave a good match with experimental results (El-Hedok 2009). More details are found under the "Computer Modeling Information" section of this report (page 78).

Problems encountered: In CFD simulations, char concentration is seen to leak into the granule feed tube of the MBGF. However, a minor modification to this model such is currently being developed will address the issue of leakage.

Assessment of impact: Demonstrated that the ANSYS-FLUENT can be used to reproduce much of the experimental data. However, the model used in ANSYS-FLUENT assumes correlation (Jung et. al 1989 and Qin 2010) for the filter efficiency. From these studies, we conclude that the current 3-D CFD model can accurately

predict the char transport as well as char accumulation processes in a moving bed granular filter and, therefore, can be used for practical design and improvement of the filter performance.

II. Development of a DNS char particle tracking code and a char trapping efficiency model

Approaches used: Granular filtration of char/fly ash is simulated by Lagrangian tracking of char/fly ash particles in a flow field obtained from direct numerical simulation (DNS) of Navier-Stokes equations governing flow past an assembly of granules. The Lagrangian particle tracking (LPT) code was validated by comparing its results with LPT studies of granular filtration in the literature by Araujo et al. (2006). The coupled DNS and LPT code is called DNS-LPT. The DNS-LPT char particle tracking code through an array of spheres with an appropriate computational approach gave an excellent match with the empirical correlation of D'Ottavio and Goren (1983). Additionally, the DNS-LPT code was extended for filtration of polydisperse particles through a granular bed. More details are found under the "Computer Modeling Information" section of this report (page 78).

Problems encountered: Initial obstacles were in choosing the right computational approach to simulate filtration of char particles in a granular bed. Different computational approaches like, volumetric initialization of particles with outflow boundary condition, volumetric initialization and inflow of particles at a specified rate followed by outflow of particles, and volumetric initialization with periodic boundary conditions applied on particles (feed particles flowing out back in at inlet) were tried. Finally, granular bed filtration simulations were done with particles distributed homogeneously in the inlet plane and continuously injected into the computational domain and removing the particles flowing out of the domain.

Assessment of impact: DNS-LPT approach developed in this project has helped us understand the mechanism of filtration of particles in granular bed and the effect of Stokes number on the filtration rate. We were able identify the presence of different filtration rates in the interfacial and downcomer regions of a granular bed by probing DNS-LPT data. During the period of the project we were also able to develop an analytical flow intensification model (Qin, 2010) for granular applications, some work has been done on the apparent particle dispersion in a granular media (Qin et. al, 2011), and additional analytical framework was developed for filtration of polydisperse particles (Ravi et. al).

References

1. Macdonald, I. F., El-Sayed, M. S., Mow, K., & Dullien, F. A. L. (1979). Flow through Porous Media-the Ergun Equation Revisited. Industrial Engineering Chemistry Fundamentals, 18(3), 199-208.

2. I. El-Hedok (2009), Moving Bed Granular Filtration of Fast Pyrolysis Char: Granular Flow Rate Study (M.S. Thesis, Iowa State University).
3. Kolakaluri, R., E. Murphy, R. C. Brown, R. O. Fox, and S. Subramaniam. A Polydisperse Model for Particulate Filtration in Gas-Solid Flow Using Particle-Resolved Direct Numerical Simulation (in preparation)

Task #6: Catalytic Stabilization of Bio-Oils

The original target catalytic moieties for our bifunctional hydrogenation /esterification catalyst was platinum (Pt) for the metal hydrogenation functionality and tethered propylsulfonic acid ($PrSO_3H$) for the esterification functionality. These two functional groups were incorporated onto a mesoporous silica framework to maximize the surface area of the catalyst. We examined how best to incorporate these two functionalities into the synthesis of the catalytic material.

The first major discovery of our work was that the presence of Pt increased the acid strength of the $PrSO_3H$ sites and accordingly the activity of the bifunctional catalyst, Pt/SBA15-$PrSO_3$ as the bifunctional material exhibited superior esterification activity to the monofunctional sample, SBA15-$PrSO_3H$ material. We hypothesized that the enhancement was due to the interaction of Pt with -SO_3H groups and detailed work was performed to demonstrate the possibility of this interaction.

Table 6.1 Mutual influence of hydrogenation and esterification in the OHE reaction (150°C)

	SBA15-$PrSO_3H$	Pt/SBA15	Pt/SBA15-$PrSO_3H$	Physical mixture: SBA15-$PrSO_3H$ + Pt/SBA15
Hydrogenation activity CH_3CHO conv. (24h)	——	8.1%	7.9%	——
Esterification activity HAc Cumulative TON (25min)	3000	——	8000	3400

The one-step hydrogenation/esterification (OHE) activity of the bifunctional catalyst, Pt/SBA15-PrSO3H, was compared with that of a physical mixture of monofunctional catalysts, SBA15-PrSO3H and Pt/SBA15. As shown in Table 6.1, the superiority of the bifunctional catalyst, Pt/SBA15-PrSO3H, in esterification activity was clearly evident with its cumulative turnover number after 20 min of reaction being more than twice that of either the monofunctional acid catalyst or the physical mixture of the monofunctional materials. This comparison suggested that the platinum modification effect was not simply a result of having platinum present in the reaction system, but was from the interaction of platinum and sulfonic acid groups when located in close proximity. It should also be noted that the hydrogenation activity of the Pt was unaffected by this interaction as the hydrogenation activity for the Pt/SBA15 and Pt/SBA15-PrSO3H were the same.

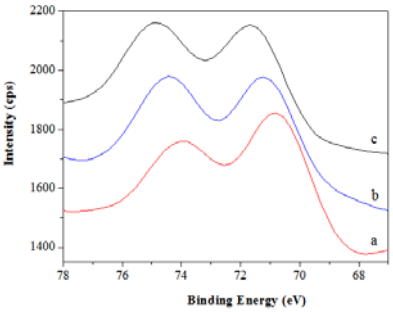

Figure 6.1. Pt $4f_{7/2}$ and $4f_{5/2}$ XPS spectra
(a): Pt/SBA15(R_F);
(b): Pt/SBA15-$PrSO_3H$(R_F);
(c): Pt/SBA15-$PrSO_3H$(R_F).

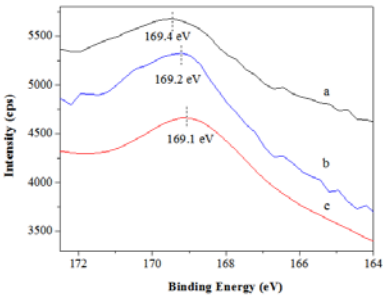

Figure 6.2. S 2p XPS spectra
(a): SBA15-$PrSO_3H$;
(b): Pt/SBA15-$PrSO_3H$(R_F);
(c): Pt/SBA15-$PrSO_3H$(R_F).

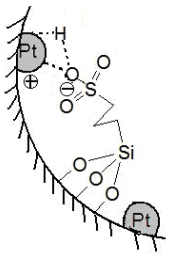

Figure 6.3. Speculated Pt and $–SO_3H$ interaction.

As given in Figures 6.1 and 6.2, XPS results showed that there was a charge transfer effect between Pt and –SO3H. The blue-shift of the Pt 4f binding energy suggested that Pt was serving as an electron donor and the red-shift of the S 2p binding energy indicated that the sulfonic acid groups were electron acceptors. As shown in Figure 6.3, we speculated that this interaction was between the Pt and OH groups of the sulfonic acid, leading to electron withdrawal from the Pt particles to the oxygen atom of the sulfonic acid groups, such that Pt became electron-deficient and O became electron-rich leading to some of the electron density being redistributed to the adjacent S atoms. This interaction with Pt might lead to the acidic protons being less restricted and more acidic. This study supported the idea of an interaction between Pt and –SO3H, which could the activity enhancement of the acid sites in the esterification reaction in the OHE reaction system when Pt was present.

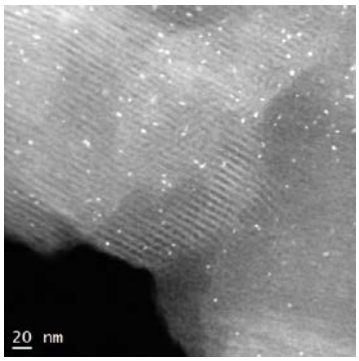

Figure 6.4. STEM image of Pt/SBA15-$PrSO_3H$ using the HCHO aqueous reduction-deposition for Pt.

The reaction results from the Pt/SBA15-PrSO3H bifunctional catalyst suggested that the hydrogenation activity of the metal functionality was rate limiting. The reduction efficiency and Pt dispersion were found to be important factors for Pt activity.

Aqueous reduction-deposition of the Pt using HCHO was demonstrated to be the best Pt loading method because it yielded the best Pt dispersion (Figure 6.4). Due to the observed fact that high temperature treatment (calcination or H_2 reduction) helped to enhance the acetaldehyde hydrogenation activity of Pt/SBA15 (the Pt was loaded through reduction-deposition by HCHO), detailed catalyst characterization was performed to investigate the key factors in these treatments to provide a basis for further enhancement of the metal functionality in the bifunctional catalysts. Both XPS and H_2-TPD were used to examine the Pt activation:

a. XPS

As shown in Figure 6.5, the peaks of Pt broadened significantly in the XPS spectra of Pt/SBA15 due to various oxidation states. The contribution at 70.8 eV was due to Pt $4f_{7/2}$ corresponding to Pt in the metallic state and the other contribution was at 71.9 eV, which was attributed to $Pt^{\delta+}$ ($0<\delta<2$) and indicated incomplete reduction of the Pt species. It was shown that the $Pt^{\delta+}$/Pt(0) ratio decreased from 2 (Figure 6.5a) to 0.8 (Figure 6.5b) after the catalyst was calcined in air at 350 ^{o}C for 4 h and this $Pt^{\delta+}$/Pt(0) ratio decreased even further to 0.22 (Figure 6.1c) after H_2 reduction at 350 ^{o}C for 4 h. Therefore, high temperature treatment in air helped to activate Pt to its metallic state and this activation was more significant if treated under H_2.

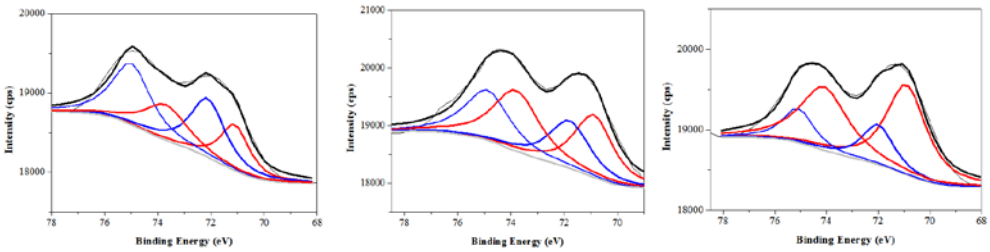

Figure 6.5. Pt $4f_{7/2}$ and $4f_{5/2}$ XPS spectra of the catalyst Pt/SBA15. (a): Reduction-deposition by HCHO; (b): After (a) and calcined in air at 350 ^{o}C for 4 h; (c): After (a) and H_2 reduction at 350 ^{o}C for 4 h.

b. H_2-TPD

As shown in Figure 6.6, both the air calcination (b) and H_2 reduction (c) procedures resulted in more hydrogen desorption at lower temperatures. Compared to calcination in air, the H_2 reduction led to an even lower hydrogen desorption temperature (a new peak centered around 350 ^{o}C), which meant that the adsorbed hydrogen was more active. We concluded that the lower desorption temperature for hydrogen, which suggested weaker metal-H bonding and more active adsorbed hydrogen, was a reason for the enhanced hydrogenation activity that was observed after high temperature treatment.

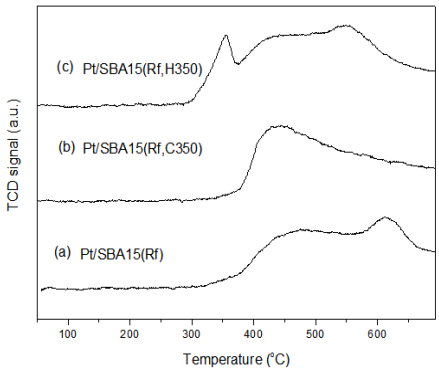

Figure 6.6 H_2-TPD profiles of Pt/SBA15. (a): Reduction-deposition by HCHO; (b): After (a) and calcined in air at 350 ^oC for 4 h; (c): After (a) and H_2 reduction at 350 ^oC for 4 h.

Since high temperature activation of Pt was required, we modified the synthesis procedure so that the Pt was introduced before the organosulfonic acid groups were incorporated, which allowed us to do the Pt activation without decomposing the organic group. Additionally we changed from the $PrSO_3H$ group to an arenesulfonic acid group ($ArSO_3H$) to further enhance the acidity of our material. The optimized bifunctional catalyst synthesis approach, which represented our best possible catalyst, is shown schematically in Figure 6.7. The procedure involved a) synthesis of the silica SBA-15 support, b) Pt impregnation onto the support using reductive deposition, c) reduction of the supported Pt, and d) grafting of the $ArSO_3H$ groups

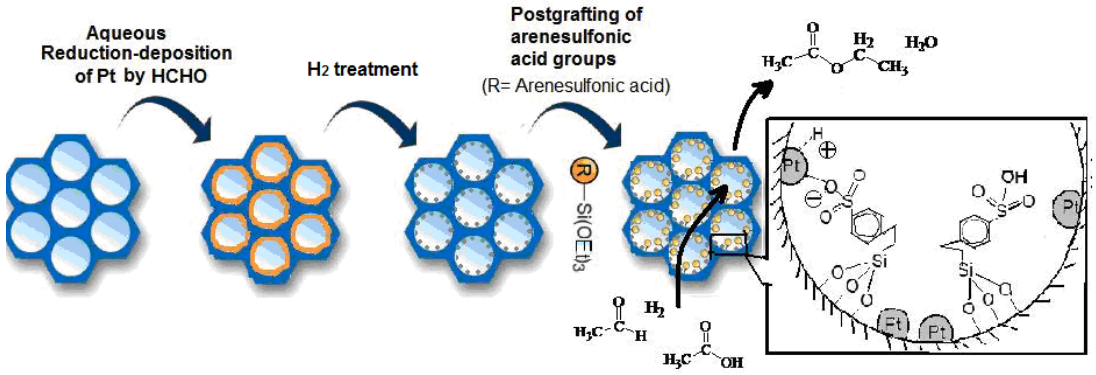

Figure 6.7. Schematic of the best synthesis procedure for the bifunctional mesoporous silica catalyst.

onto the Pt-impregnated SBA-15. The catalyst was characterized and used in the OHE reaction. The reaction results are shown in Figure 6.8 at 150°C. As can be seen from the figure, we doubled the reaction rate for both the hydrogenation and esterification by optimizing the incorporation of the functional groups and changing from tethered proplysulfonic acid groups to arenesulfonic acid groups. Unfortunately, the activity of the combined catalyst was still insufficient so we would have to operate at a higher reaction temperature to achieve the desired conversions, which would create unacceptable bio-oil stability problems prior to the removal of the aldehydes and the organic acids. Therefore, it is clear that a different approach for catalystic stabilization of bio-oil is needed.

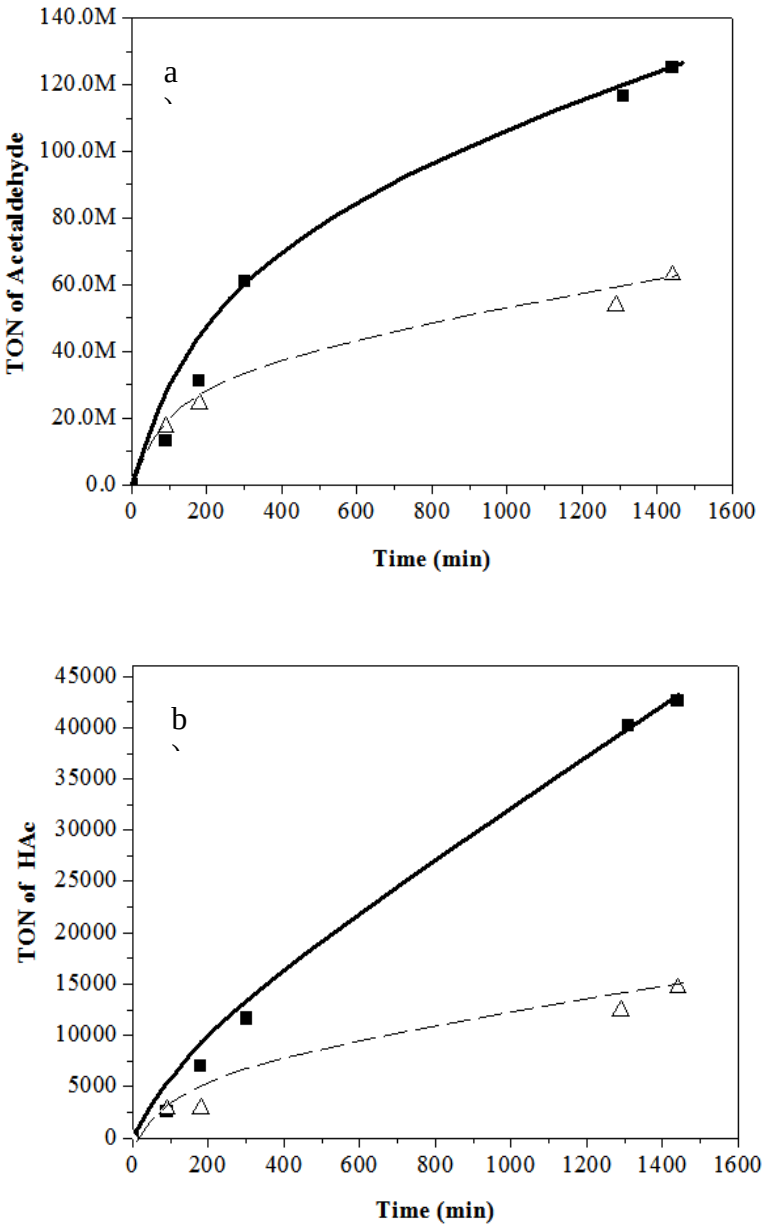

Figure 6.8. Cumulative turnover numbers for the catalysts with different sulfonic acid groups; a) turnover number for acetaldehyde; b) turnover number for acetic acid. ■——: Pt/SBA15-Ar$SO_3H(R_F)$; △_ _ _: Pt/SBA15-Pr$SO_3H(R_F)$.

Task #7: Bio-Oil Characterization and Accelerated Aging Tests

One objective of Task #7 is to utilize existing and develop new analytical protocols to measure stability in bio-oil for the strategies employed in this project. A description of tests used and results can be found in the summaries for tasks #1-3 above.

Another objective of this task is to update capital and operating cost estimates for the pyrolysis process with the selected stabilization strategies included. The whole biomass fast pyrolysis

model with bio-oil stabilization model using Aspen Plus has been used to obtain mass balances on the system. The whole system consists of the following six areas:

a.) A100 Pretreatment (Chopping, steam drying, acid Pretreatment, grinding,)
b.) A200 Fast Pyrolysis and Hot Gas Filtering (Fluidized bed and moving bed granular filter)
c.) A300 Bio-oil Recovery (Five stages fractioning system consists of condenser and ESPs)
d.) A400 Combustion (Combustor)
f.) A500 storage (storage tank)

The simulation model was adjusted to 2000 metric tons per day of feedstock to facilitate analysis of capital cost and determine the unit cost of stabilized bio-oil on the industrial scale. This is an updated fast pyrolysis system model including the acid treatment process and bio-oil stabilization parts. In this model, the red oak is employed as the feedstock which is pretreated using sulfuric acid before sent to the fluidized bed. The bio-oil recovery area includes five stage fractions (SF) simulated by condensers and Electrostatic precipitators (ESP). The whole process is illustrated in Figure 1. Table 1 shows mass fractions of red oak bio-oil fractions as collected from the fluidized bed reactor with the fractioning bio-oil recovery system. The results show that the yield is 1304 metric tons per day of bio-oil (65.2% of dry biomass). As estimated, installed equipment cost is $207 Million dollars and the total project investment is $235 Million dollars. Figure 2 shows the detailed equipment cost for each area. Among all the areas, the combustion area occupies the majority of the installed equipment cost which is up to 39% of the total installed equipment cost. Table 2 details the Key operating costs for red oak bio-oil stabilization system.

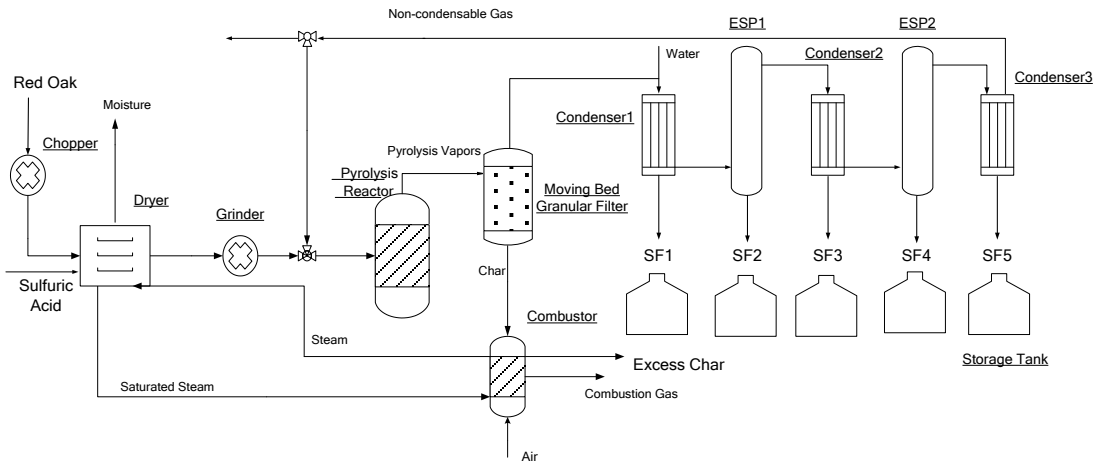

Figure 1. Process diagram for 2000 metric tons per day of red oak bio-oil stabilization

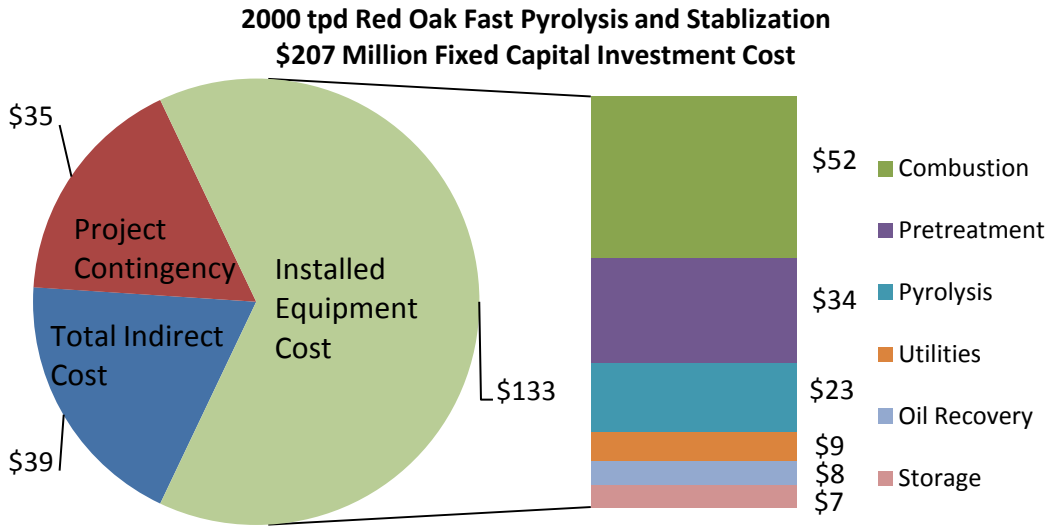

Figure 2. Installed equipment cost for red oak to stable bio-oil.

Table 1. Mass distributions for red oak bio-oil fractions

Stage Fraction(SF)	wt%	mass (metric tons per day)
SF1	21	69.38
SF2	26.5	87.56
SF3	5.46	18.04
SF4	11.1	36.67
SF5	36	118.94

Table 2. Key operating costs for red oak bio-oil stabilization system.

Parameters	Unit Cost ($/kg)	Year Cost ($MM)
Variable Operating Costs		
Red Oak	0.083	54.4
Sulfuric Acid	0.23	0.98
Solids Disposal Cost	0.0198	2.55
By Product		
Char	0.0182	1.32
Fixed Operating Costs		
Total Salaries		1.89
Insurance & Taxes		3.11
Overhead		1.13
Maintenance		3.74

Publications

Brown, R.C. Presentation: Prospects for a Thermolytic Sugar Platform. International Conference on Thermochemical Conversion Science. 2011. Chicago, IL.

Cecconi, M. and T. Meyer, Evaluation of Laser Diagnostics for Fast-Pyrolysis Reactors. Spring Technical Meeting of the Central States Section of the Combustion Institute, Dayton, Ohio, April 22-24, 2012.

El-Hedok, I.A., L. Whitmer, and R.C. Brown, The influence of granular flow rate on the performance of a moving bed granular filter. Powder Technology, 2011. 214(1): p. 69-76.

Kolakaluri, R., E. Murphy, R. C. Brown, R. O. Fox, and S. Subramaniam. A polydisperse model for particulate filtration in gas-solid flow using particle-resolved direct numerical simulation (in preparation)

Kolakaluri, R., S. Tenneti, and S. Subramaniam. Fine particulate filtration in gas-solid flow using particle-resolved direct numerical simulation. In 48th Annual Technical Meeting of Society of Engineering Science October 12-14, 2011

Kolakaluri, R., S. Subramaniam, and R. O. Fox. A model for efficiency of granular filtration based on granule-resolved direct numerical simulation of particle trapping (poster) In Workshop on Multi-phase Flow Science May 4 – 6, 2010
Kuzhiyil, N., D. Dalluge, and R.C. Brown. Poster: Passivating Alkali During Biomass Pyrolysis for Higher Yields of Anhydrosugars. International Conference on Thermochemical Conversion Science. 2011. Chicago, IL.

Kuzhiyil, N., D. Dalluge, and R.C. Brown. Poster: Biomass Pretreatment to Improve Bio-Oil Stability. Symposium on Thermal and Catalytic Sciences for Biofuels and Bibased Products. 2010. Ames, IA

Miao, S. and Shanks, B.H., "On the Mechanism of Acetic Acid Esterification over Sulfonic Acid Functionalized Mesoporous Silica," *J. Catal.*, **279**, 136-143 (2011).

Miao, S. (presenter) and B.H. Shanks, "Investigation of Esterification of Biomass Pyrolysis Acids Over Sulfonic Acid-Functionalized Mesoporous Silicas," Annual Meeting, American Institute of Chemical Engineers, Nashville, TN, November, 2009.

Murphy, E., R. Kolakaluri, and S. Subramaniam. A model of granular filtration of polydisperse particles. In 47th Annual Technical Meeting of Society of Engineering Science October 3-6, 2010

Olthoff, A., S. Sadula, and R.C. Brown. Poster: Fractionating Recovery for Bio-Oil Stabilization. Symposium on Thermal and Catalytic Sciences for Biofuels and Bibased Products. 2010. Ames, IA

Sadula, S., A. Olthoff, R.C. Brown. Poster: Stability of Bio-Oil as Measured by Gel Permeation Chromatography. International Conference on Thermochemical Conversion Science. 2011. Chicago, IL.

Tang, Y., Miao, S., Shanks, B.H., and Zheng, X., "Bifunctional Mesoporous Organic–Inorganic Hybrid Silica for Combined One-step Hydrogenation Esterification," *Appl. Catal A: Gen.,* **375**, 310-317 (2010).

Tang, Y., Miao, S., Pham, H.N., Datye, A., Zheng, X., and Shanks, B.H., "Enhancement of Pt/SBA15 Catalytic Activity in the Hydrogenation of Aldehydes," *Appl. Catal. A: Gen.,* **406**, 81-88 (2011).

Tang, Y., Miao, S., Shanks, B.H., Mo, L., and Zheng, X., "Enhanced One-step Hydrogenation/Esterification over a Bifunctional Organic-Inorganic Hybrid Silica," in final preparation (2011).

Tang, Y. (presenter), S. Miao and B.H. Shanks, "Combined One-Step Hydrogenation/Esterification over Bifunctional Mesoporous Organic–Inorganic Hybrid Silica: Model Reaction for Bio-Oil Upgrading," Annual Meeting, American Institute of Chemical Engineers, Nashville, TN, November, 2009.

Tang, Y. (presenter), S. Miao, H. Pham, A. Datye, B.H. Shanks, X. Zheng, "Effect of Pt Loading on Enhancing Aldehyde Hydrogenation for One-step Hydrogenation Esterification (OHE)," Annual Meeting, American Institute of Chemical Engineers, Salt Lake City, UT, November, 2010.

Qin, Z. A flow intensification Model for granular filter applications, Advanced powder technology 21, 2, 180-186, 2010

Qin, Z., Fox, R. O., Subramaniam, S., Pletcher, R., Zhang, L. On the apparent particle dispersion in granular media, Advanced powder technology 22, 6, 728-734, 2011

Whitmer, L. and R. Brown. Poster: Hot Gas Filtration of Pyrolysis Vapor via Moving Bed Granular Filter. International Conference on Thermochemical Conversion Science. 2011. Chicago, IL.

Whitmer, L., I. El-Hedok, and R. Brown. Poster: Gas Cleaning Systems for Syngas and Bio-oil Production. in Symposium on Thermal and Catalytic Sciences for Biofuels and Biobased Products. 2010. Ames, IA.

Website Information

Center for Sustainable Environmental Technologies, Iowa State University
http://www.cset.iastate.edu/research/current-research/

Networks or Collaborations Fostered

Diagnostics developed in Task 4 were applied for fundamental studies of particulate and aerosol filtration studies in collaborative work between Drs. Shankar Subramaniam and Terrence R. Meyer at Iowa State University.

Diagnostics developed in Task for were installed in a pilot scale pyrolysis system as part of collaborative research between Drs. Robert C. Brown and Terrence R. Meyer at Iowa State University.

The Fox and Subramaniam research groups collaborated with Dr. Terry Meyer's laser diagnostics group (**Task. 4**) in Mechanical engineering at Iowa state university for validation of the DNS-LPT approach developed. An experimental setup was developed to filter the particulate flow through a granular bed. Schematic of the experimental setup is given in Figure 1.

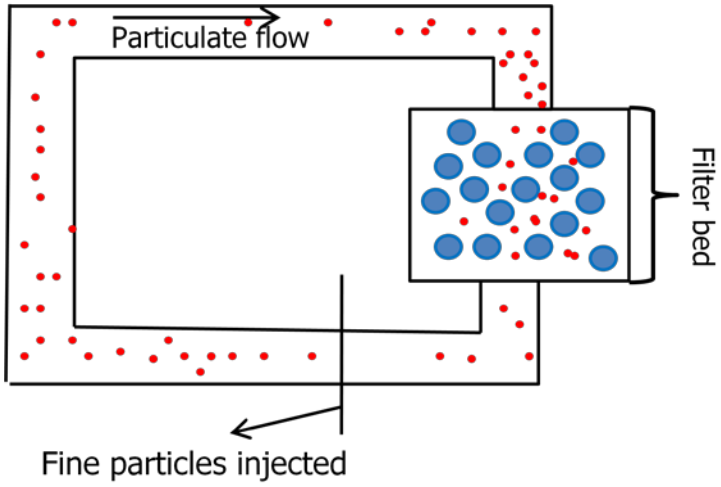

Fig. 1: Schematic of experimental setup for granular filtration

Three different granular bed thickness 0.44, 0.79, and 1.06 inches were tested for a volume fraction 0.5, Reynolds number 60, granule diameter 2mm and fine particle diameter 20 microns. The time-averaged filter efficiency η results obtained from simulation were compared with experimental results obtained from 0.44 inch granular bed.

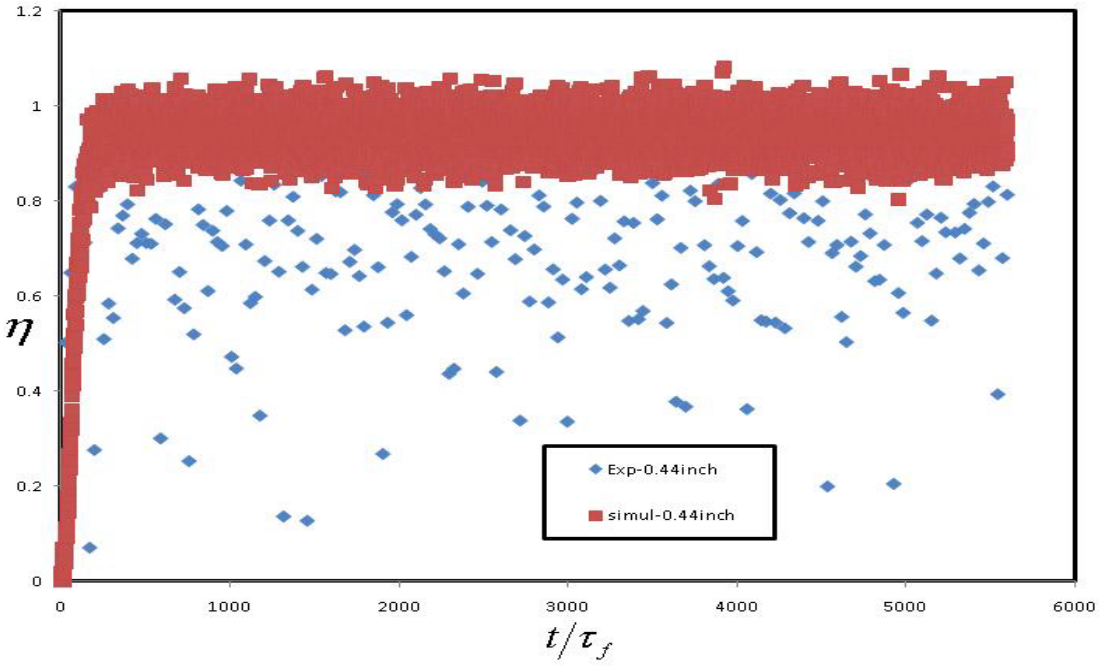

Fig. 2: Steady-state filter efficiency with non-dimensional time for a volume fraction of 0.5 and Reynolds number 60.

Figure 2 shows the comparison of filter efficiency between DNS-LPT and the experimental results obtained from Laser measurements. The time-averaged filter efficiency obtained from experimental data of 0.44 inch filter gave 0.71 and the time-averaged filter efficiency obtained from DNS-LPT of 0.44 inch filter gave 0.94. The simulation results might be over estimating the filter efficiency due to bouncing of particles from the surface of granules. The bouncing effect was also found in literature (D'Ottavio and Goren 1982, Jung et. al 1989). The Stokes number of the particles we considered for the simulation falls in the bouncing regime, and implementing bouncing mechanism in simulations might help in better match with experimental results.

Inventions/Patent Applications, Licensing Agreements

Passivating Alkali During Biomass Pyrolysis to Obtain Higher Yield of Sugars

Technologies/Techniques

Laser-induced breakdown spectroscopy (LIBS) for elemental analysis was implemented for the first time for pyrolysis environments. This includes calibration of signals within a multiphase flow with aerosols, particulates, and pyrolysis vapors.

Laser-scattering was also implemented for qualitative planar imaging of aerosols. This can be used to separate aerosols from small char particles during hot-vapor filtration.

Laser-induced incandescence (LII) for identification of char particles was implemented for the first time in pyrolysis environments. This can be used to differentiate small char particles from aerosols during hot-vapor filtration.

The capability of simulating a full granular bed using ANSYS-FLUENT was developed, which was not done before. A DNS-LPT setup was also developed to simulate micro scale filtration of particles through a granular bed consisting of homogenous randomly distributed granules and also have the capability to run for moderate Reynolds number. The DNS-LPT setup was also extended to simulate the filtration of polydisperse particles. An analytical framework was also developed to find the polydisperse filter efficiency in a granular bed (Ravi et. al).

Computer Modeling Information

1. Computational model to simulate char removal by the MBGF was used to stabilize bio-oil from fast pyrolysis was developed using ANSYS-FLUENT 12.1

   Assumptions:

   - The volume fractions of char particles are considered to be very low in the gas phase and the effect of char particles on the gas phase is neglected.

   - The concentration of char particles through a granular bed is obtained by solving a scalar equation in ANSYS-FLUENT and a model is provided for the source and diffusion term in the scalar equation through an UDF.

   Use: This will give us capability to solve full granular bed using ANSYS-FLUENT with improved models obtained from DNS-LPT and investigate and improve design of MBGF for maximizing char removal.

2. Model for char trapping efficiency by performing high-fidelity microscale simulations

   a. Particle-tracking in a flow field obtained from granule-resolved direct numerical simulations (DNS)

   Assumptions:

   i. A statistically homogeneous randomly distributed granule in a computational domain with Navier-Stokes equation solved can represent the complex flow structure in a granular bed, which has been proved to be very accurate.
   ii. The char particles are taken to be homogenously distributed in the plane perpendicular to the flow and inhomogeneous along the flow direction
   iii. Periodic boundary conditions applied to char particles in y and z direction and inflow and outflow boundary conditions in x direction and this setup represents the granular bed.

Use: DNS-LPT is a promising approach for the understanding of the nature or mechanisms of the filtration process due to the difficulty in using experimental studies using experimental techniques in a granular bed.

b. Performance criteria for the model related to the intended use;

- CFD model will be validated against experimental data (I. El-hedok 2009) from the MBGF and published literature
- DNS tracking code validation with published empirical correlation and experimental data

c. Test results to demonstrate the model performance criteria were met (e.g., code verification/validation, sensitivity analyses, history matching with lab or field data, as appropriate);

CFD simulations validation with experimental data:

I. Pressure gradient calculated from CFD simulations (8200 Pa/m) gave an excellent match with the theoretical result of Ergun's equation (McDonald 1972) (8002 Pa/m)

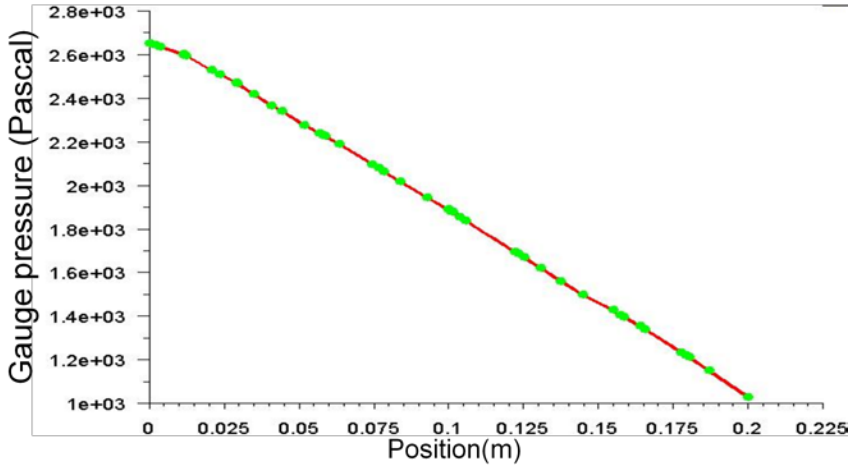

Fig. 3: Pressure distribution along the axis of filter for a flow rate of 620 slpm, particle concentration of 2.7e-06 and volume fraction of 0.63. Green symbols are simulation results and red line is from Ergun equation.

II. CFD model developed from ANSYS-FLUENT is validated by comparing the char accumulation rate with the experimental results with Jung et. al (1989) and Qin (2010) models implemented in the CFD model.

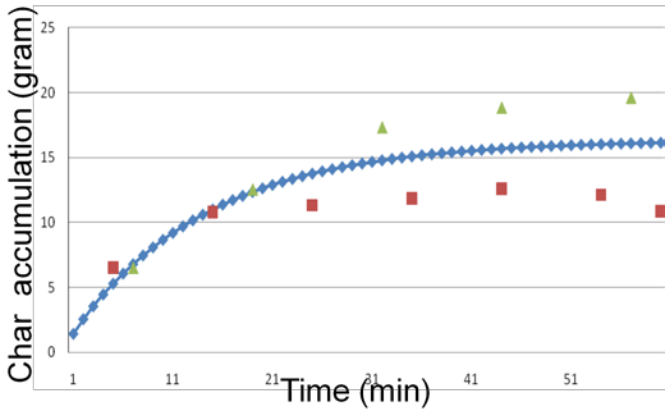

Fig. 4: The blue symbols are numerical results for granule speed of 0.00063 m/s, air flow rate of 620 slpm and green and red symbols are experimental results for granule speed of 0.00057 and 0.00072 m/s and air flow rate of 618 slpm

DNS-LPT tracking code validation:

1. Validation test of Lagrangian particle tracking code with published literature.

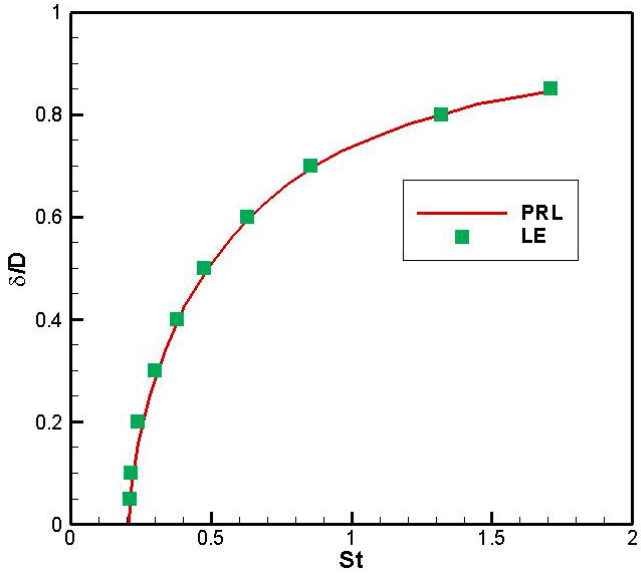

Fig. 5: Validation of Lagrangian particle tracking code (green symbols) against results from Araujo et al. 2009 (red line) with a 2D porosity of 0.9.

Figure 5 shows an excellent comparison of LPT results with published numerical results (Araújo et. al 2006)

2. Validation test of 3D direct numerical simulation of granular bed with existing empirical correlation

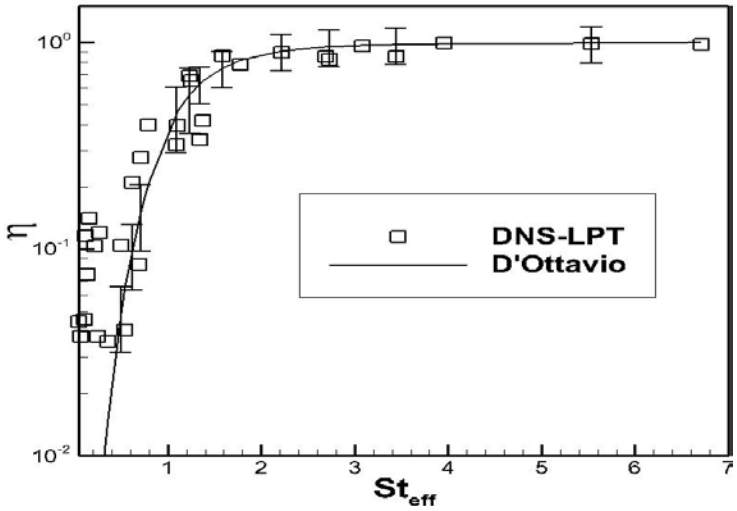

Fig. 6: DNS steady state filter efficiency η is compared with filter efficiency calculated from the correlation of D'Ottavio and Goren (1983) with the effective Stokes number

A good match of DNS-LPT results in comparison with published experimental correlation results gives us confidence in using the DNS-LPT code in the flow range of Stokes to moderate Reynolds numbers.

DNS-LPT code convergence studies:

We examined the influence of some of the important numerical parameters on the DNS-LPT simulations, to test the convergence of simulations. We investigated the influence of number of computational particles initialized on inlet plane on normalized number density or concentration of the fine particles. Fig. 7 shows that the normalized number density profile along the computational domain is insensitive to number of computational particles initialized on the inlet plane.

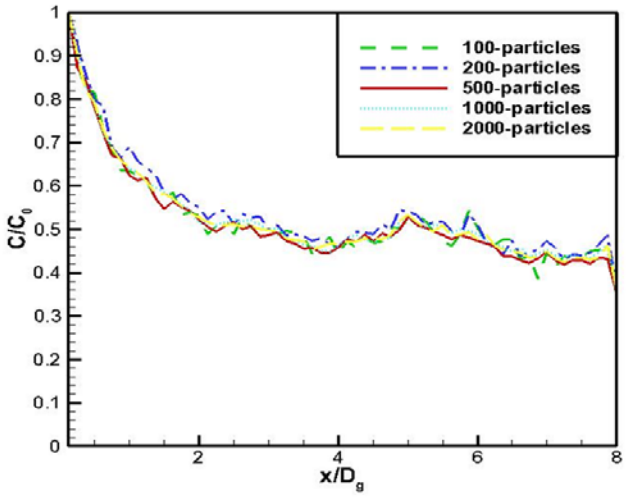

Fig. 7: Normalized number density for a volume fraction of 0.1, Reynolds number 2.5, and Stokes number 1.0 along the length of the computational domain

The effect of number of computational particles initialized at each time step on the filter efficiency is shown in fig. 8. It can be seen in the figure that the time-averaged filter efficiency is almost the same for different number of computational particles initialized on the inlet plane and there is also decrease in standard deviation from the mean with increase in number of computational particles initialized. The standard deviation normalized with square root of computational particles is almost constant after 500 computational particles. This concludes that the DNS-LPT simulations results done with more than 500 computational particles are fully convergent.

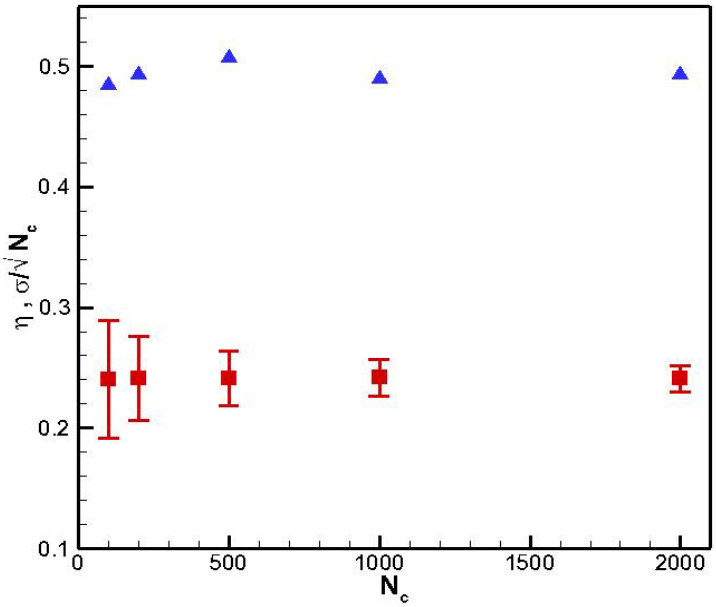

Fig. 8: η is the time-averaged filter efficiency after the filtering of particles has reached steady state with number of particles initialized at the inflow plane and the error bars denote the deviation from the mean. Blue symbols are the standard deviation normalized with number of particles

d. Theory behind the model, expressed in non-mathematical terms;

CFD is used to understand the transport of fine particles in a moving bed granular filter (MBGF). MBGF has a complex geometry, a commercial CFD software package ANSYS-FLUENT will be an ideal option for mesh generation and solving the flow through such a complicated geometry. An Eulerian model in ANSYS-FLUENT that solves momentum and mass conservation equations for gas and solid phases is used in this project. The concentration of char in the MBGF is modeled as a transported scalar with a sink term representing filtration of char particles. The efficiency of the MBGF in trapping char is a modeled term in the scalar equation. The existing models used in the scalar equation are improved using DNS.

In DNS, flow through an array of spheres is solved using an in-house code called PUReIBM, which is based on immersed boundary method, while the char particles are tracked as Lagrangian point particles in the flow fields obtained from PUReIBM. These are a state-of-the-art simulation technique for this problem. The improved char trapping model was developed

and implemented in ANSYS-FLUENT and results are compared with published empirical correlations (D'Ottavio and Goren 1983, I. El-Hedok 2009).

e. Mathematics to be used, including formulas and calculation methods;

1. ANSYS-FLUENT CFD modeling:

A. Dynamics of filtration

A.1. Particle concentration

Particles are carried by fluid flow to move through granular bed voids. Suppose the volumetric particle concentration is c; porosity of granular media is ε; physical velocity of fluid is $\underset{\sim}{u}_f$, the equation governing c is

$$\frac{\partial c}{\partial t} + \nabla \cdot \left(\underset{\sim}{u}_f c \right) = -N . \tag{1}$$

Here N is the particle filtration rate, which is the volume of particle filtered per unit bed volume per unit time. Similarly the volumetric concentration of particle captured throughout the granular filter satisfies

$$\frac{\partial c}{\partial t} + \nabla \cdot \left(\underset{\sim}{u}_s c \right) = N , \tag{2}$$

Where $\underset{\sim}{u}_s$ is physical velocity of granules. Usually at quasi-steady state the particle concentration throughout the bed is observed to follow an exponential profile (Tien and Ramarao 2007).

$$\frac{dc}{dz} = -\lambda c . \tag{3}$$

Therefore N may be approximated as

$$N = \lambda \left| \underset{\sim}{u}_f \right| c . \tag{4}$$

Since a single layer of granular media formed by granules of diameter d_g should have a layer depth l, where

$$l^3 \left(1 - \varepsilon \right) = \frac{\pi}{6} d_g^3 . \tag{5}$$

In each layer, we have

$$\frac{dc}{dz} \approx \frac{c_{out} - c_{in}}{l} = -\frac{e c_{in}}{l} , \tag{6}$$

where e is one layer filtration efficiency and c_{in} and c_{out} are the inflow and outflow particle concentrations. We can see

$$\lambda = \frac{e}{l}. \tag{7}$$

If a single collector efficiency is η_s, the rate of particle removal per collector is $\left|u_f\right| \cdot \left(\frac{\pi}{4} d_g^2 \varepsilon\right) \cdot c_{in} \cdot \eta_s$ so

$$e = \frac{\left|u_f\right| \left(\frac{\pi}{4} d_g^2 \varepsilon\right) c_{in} \eta_s N_c}{u_s c_{in}}, \tag{8}$$

where N_c is the number of granules in a single layer with surface area unity and u_s is the fluid superficial velocity. Since

$$l \cdot \left(1m^2\right) \cdot \left(1-\varepsilon\right) = N_c \cdot \left(\frac{\pi}{6} d_g^3\right) \tag{9}$$

and $u_s = u_f/\varepsilon$, we have

$$e = \eta_s \cdot \left[1.21\left(1-\varepsilon\right)^{2/3}\right]. \tag{10}$$

Therefore

$$\lambda = \frac{e}{l} = \frac{1.5\left(1-\varepsilon\right)}{d_g} \eta_s. \tag{11}$$

We may notice that according to equations (4) and (11), the particle removal rate N is zero as either $c = 0$ or $\varepsilon = 1$, which are in agreement with our physical intuition.

A.2. Single collector efficiency

Usually η_s varies with ε_s, St (Stokes number), Re (Reynolds number) and $N_R = d_p/d_g$, where d_p is the particle diameter. η_s increases with increasing these parameters except ε in inertial impact regime. However, as St is greater than a certain critical value, η_s decreases with increasing St due to possible bouncing-off mechanisms. Fig. 1 shows a sketch of different regimes of single collector efficiency.

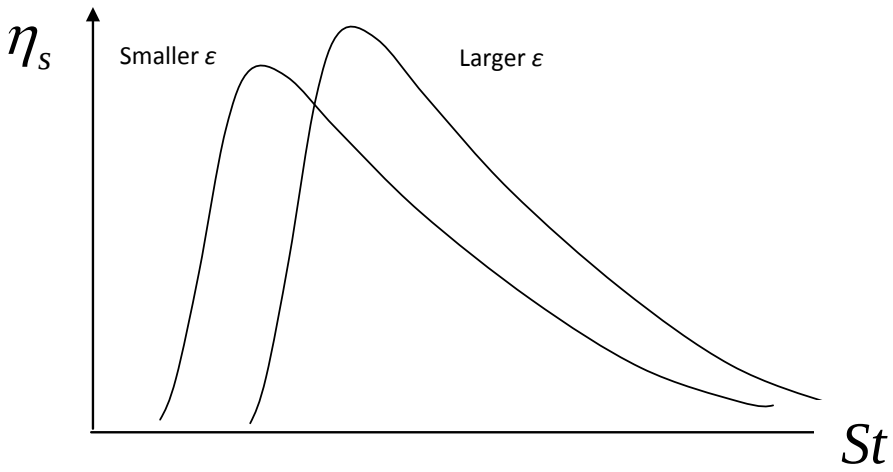

Fig. 9. The single collector efficiency regimes

In the inertial impaction regime, according to Qin 2010. We have

$$\eta_s = \frac{St^{3.1}}{e^{20\varepsilon} \times 3.3 \times 10^{-7} + St^{3.1}}. \tag{12}$$

In the bouncing-off regime, we use Jung et. al.'s correlation.

$$\eta_s = \frac{2}{3}\varepsilon^{4.23} St^{-1.968}. \tag{13}$$

This formula was proposed to correlate experimental data of KHP particles of 2.3 μ diameter. Now, according to physical reasoning, we have to conclude that if particles do not significantly alter fluid flow field, the bouncing-off rate should be controlled by particle kinetic energy $ke \propto \frac{1}{2} m_p u_s^2$ rather than Stokes number. Therefore, the above equation is modified according to this insight:

$$\eta_s = \frac{2}{3}\varepsilon^{4.23} \left(St \frac{\sqrt{\rho_{KHP} d_{p,KHP}}}{\sqrt{\rho_p d_p}} \right)^{-1.968}. \tag{14}$$

Since $\rho_{KHP} = 1640 kg/m^3$, $\rho_p = 1000 kg/m^3$ (char), $d_p = 24\mu$. We have

$$\eta_s = 4\varepsilon^{4.23} \left(St \right)^{-1.968}. \tag{15}$$

The single collector efficiency thus is the smaller value of those given by equations (12) and (15). By using the definition of Stokes number, we may find

$$St = \frac{\rho_p d_p^2 u_s}{9\mu_f d_g} = 1.62 u_s, \tag{16}$$

Since we use room temperature air as fluid and $d_g = 2mm$.

A.3. Effects of particle deposition

As char particle deposits in the granular filter, it may coat the gravel surfaces, or clog the voids between gravels. This causes the porosity to decrease, which in turn changes the fluid velocity, drag and single collector efficiency. If the volume of char deposit per unit volume at a given location is σ, the porosity becomes

$$\varepsilon = \varepsilon_0 - \frac{\sigma}{1-\varepsilon_d}, \tag{17}$$

where ε_0 is the original porosity and ε_d is the porosity of char deposit, which we will assume to be 0.

B. Realization in ANSYS-FLUENT

In ANSYS-FLUENT, we defined two User-Defined-Scalars (UDS) for the particle concentration in gas and the density of particle captured in filter respectively. Then by using User-Defined-Functions (UDF), we gave the source terms for these two scalars' governing equations, namely equations (1) and (2). Also we used an UDF to adjust the filter porosity according to equation (17).

C. Results

C.1. Boundary conditions

We simulated a case with gas inflow speed 30m/s, which corresponds to a flow rate 619 slpm, close to the experimental setup 620 slpm. The inlet particle concentration is 2.7×10^{-6}. The filter is initially filled with granules of volume fraction 0.63. The gas outlet pressure is 1 atm. Except the gas inlet and outlet, all boundaries are walls.

C.2. Velocity field

Due to the fact that the gas inlet is located at one side of the outer cylinder, the gas flows in a spiral manner into the filter and some asymmetry should be expected in the flow field. These features can be observed from Fig. 10

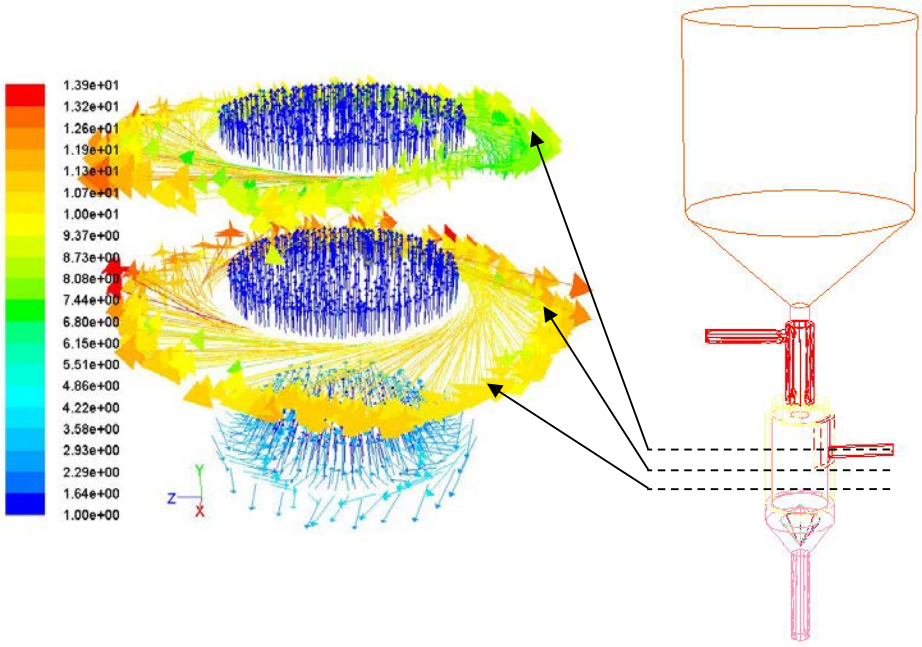

Fig. 10. Velocity field of gas at three selected cross-sections

C.3. Particle concentration

The particle (char) concentration at three cross-sections in the bed at time 60 seconds is shown in Fig. 11. Due to the asymmetry of flow field, the char concentration also shows asymmetry at the interface between gas and granules (the lowest cross-section in Fig. 11). This should cause the asymmetry in char collection, which is the case as shown in Section C.4. The char concentration at the axis cross-section at time 30 minutes is shown in Fig. 12.

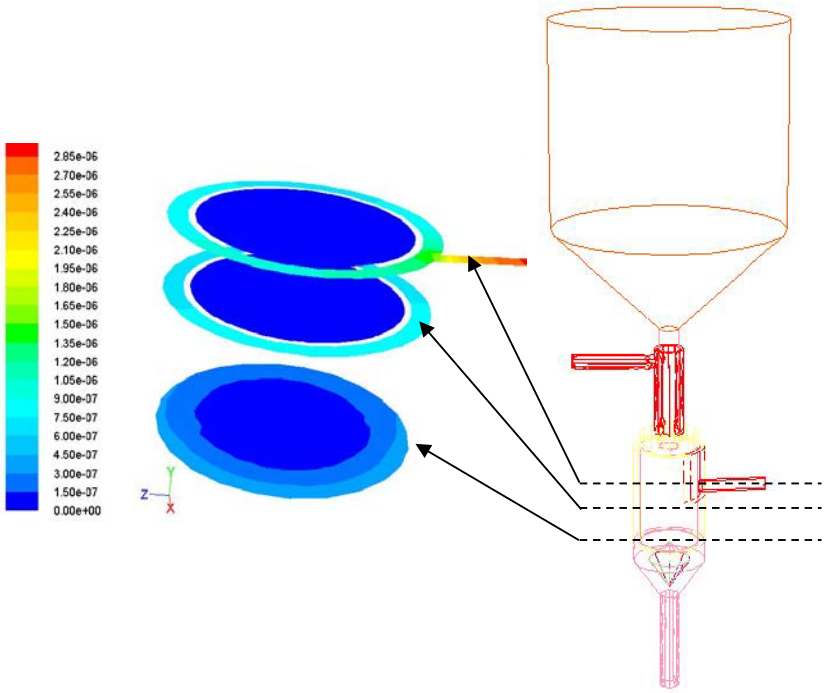

Fig.11. Char concentration at three selected cross-sections (t = 1 min)

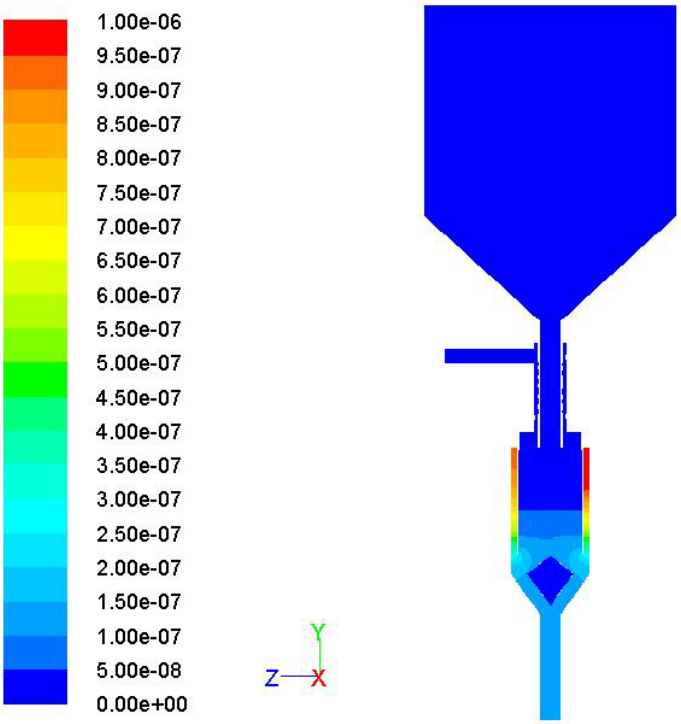

Fig.12. Char concentration at the axis cross-section (t = 30 min)

C.4. Char collection

The densities of char captured by the filter at three different times are shown in Figures 13, 14 and 15.

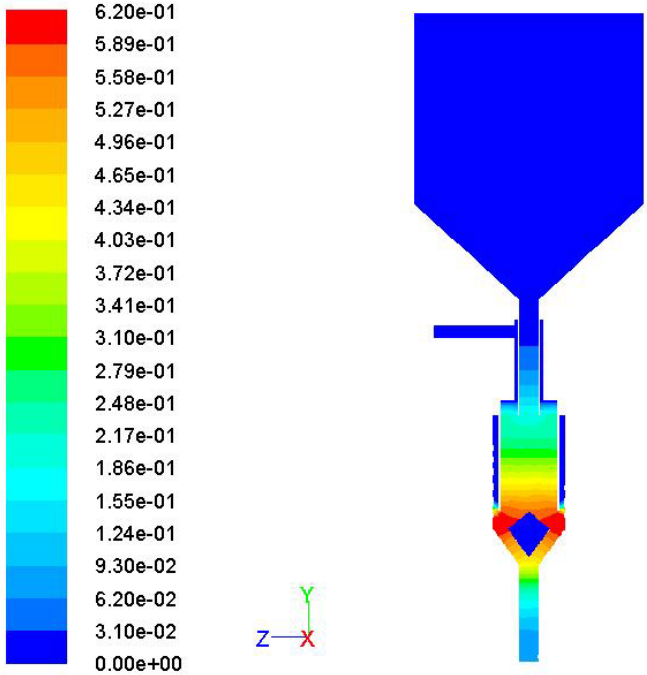

Fig. 13. Char collection density at the axis cross-section at t = 1 min

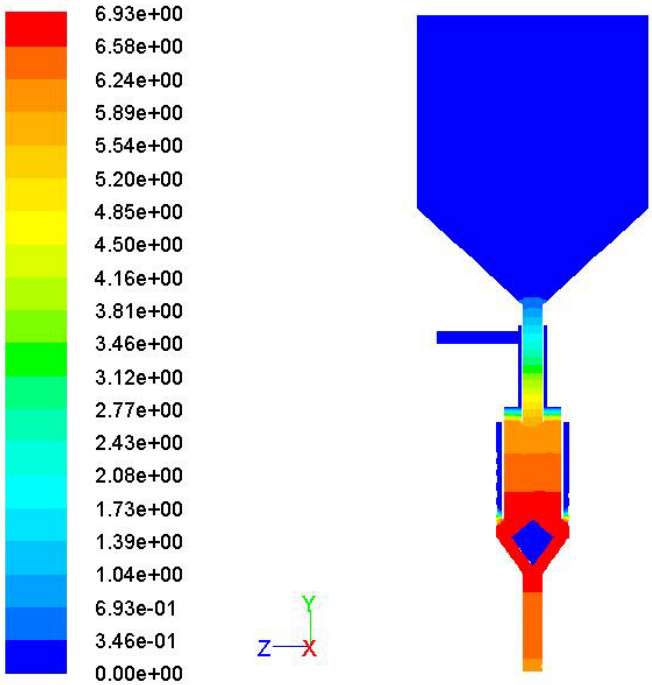

Fig. 14. Char collection density at the axis cross-section at t = 15 min

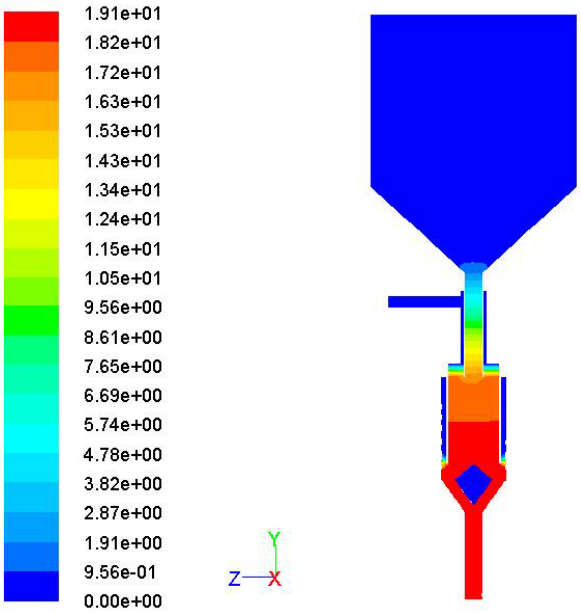

Fig. 15. Char collection density at the axis cross-section at t = 35 min

Most char is captured close to the interface of gas and granular solids at the early stage of filtration. As time goes on, more and more char is collected by the main body of filter. As indicated in Section C.4, the char density also shows asymmetry, as shown in Fig. 16.

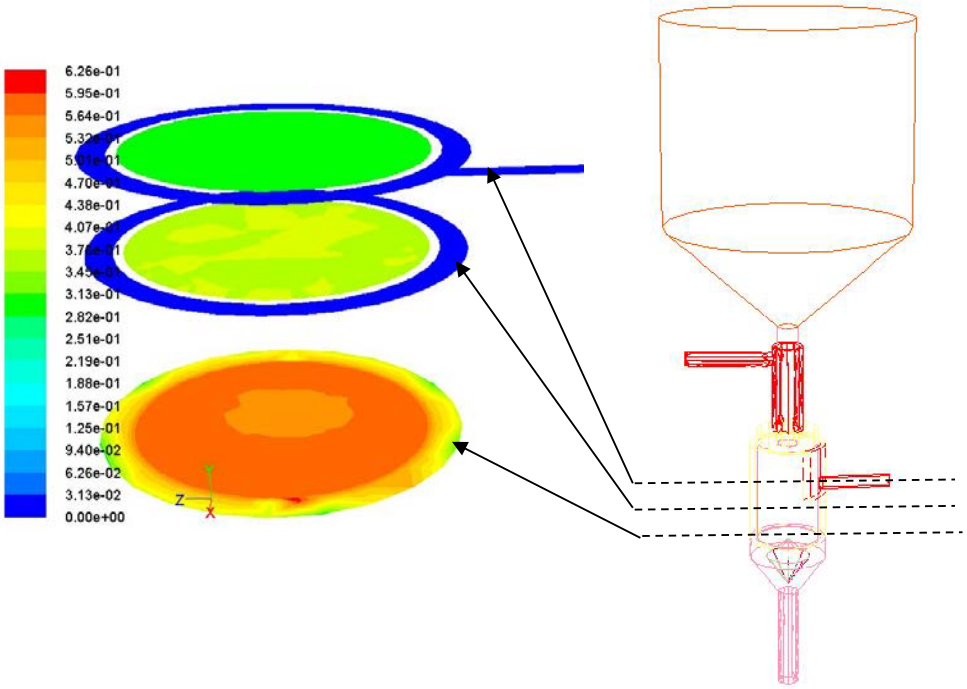

Fig. 16. Char density at three selected cross-sections at t = 1 min

C.5. Filter efficiency

As time goes on, the filter efficiency gradually decreases due to the enhanced bouncing-off rate caused by the decreasing bed porosity, which in turn is resulted in by char deposition. Fig. 17 shows the filter efficiency variation with time.

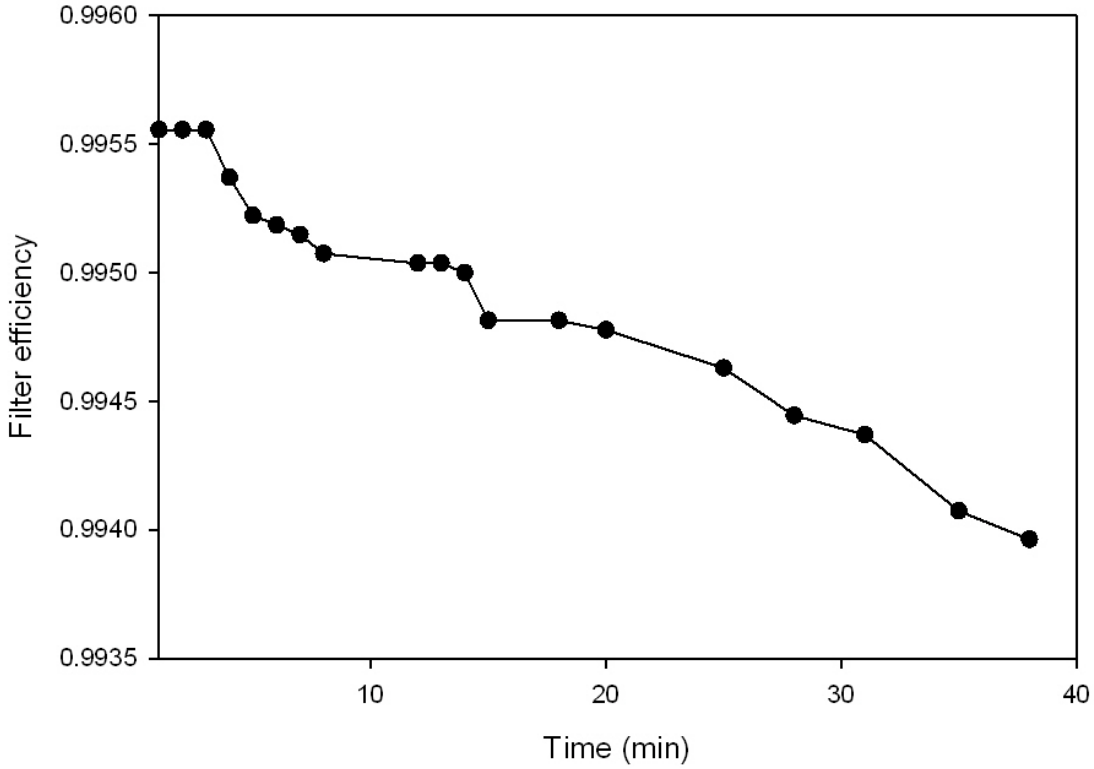

Fig. 17. Filter efficiency with time (minutes)

2. DNS-LPT char trapping model:

i. Dispersed phase governing equations:

In the DNS approach used here, the dispersed-phase consisting of fine particles are represented in a Lagrangian frame at time t by

$$\frac{d\mathbf{X}^{*(i)}(t)}{dt} = \mathbf{V}^{*(i)} \tag{18}$$

$$\frac{d\mathbf{V}^{*(i)}(t)}{dt} = \frac{\mathbf{f}^{*(i)}}{m_p^{(i)}} = \mathbf{A}^{(i)} \tag{19}$$

where $\mathbf{X}^{*(i)}(t), \mathbf{V}^{*(i)}(t), m_p^{(i)}$ denotes the i^{th} particle's position, velocity and mass, $\mathbf{f}^{*(i)}$ and $\mathbf{A}^{(i)}$ are the instantaneous force and acceleration experienced by the i^{th} physical particle. The particle force model that subsumes different drag force correlations is:

$$\mathbf{f}^{(i)}t = f(\mathbf{U}^f(\mathbf{X}^{*(i)}(t),t), \mathbf{V}^{*(i)}, \rho_f, \mu_f, \rho_p, D_p), \tag{20}$$

where ρ_f, μ_f and $\mathbf{U}^f(\mathbf{X}^{*(i)}(t),t)$ are the fluid phase density, kinematic viscosity and the velocity of the fluid at the particle location. In this study only the drag force is considered. In the case of finite mass loading of the particles in the flow, the momentum equation is augmented by an interphase momentum transfer term $\mathbf{F}^{fp}$, which accounts for the coupling of the dispersed-phase momentum with the fluid phase. To calculate the mean interphase momentum term from the LE solution, the mean fluid velocity field $\mathbf{U}^f(\mathbf{x},t)$, and the position and velocity of the computational particles are $\mathbf{X}^{*(i)}(t), \mathbf{V}^{*(i)}(t), i = 1,....,N_c$. The calculation of particle forces $\mathbf{f}^{*(i)}$. This mainly requires the fluid velocity in the particle location $\mathbf{U}^f(\mathbf{X}^{*(i)},t)$ from the fluid velocity at Eulerian grid nodes. The numerical estimation of the fluid velocity field $\mathbf{U}^f(\mathbf{x},t)$ at the particle location $\mathbf{X}^{*(i)}$ at M grid nodes is denoted as $(\mathbf{U}^f(\mathbf{X}^{*(i)},t))_M$ and is obtained through forward interpolation

$$(\mathbf{U}^f(\mathbf{X}^{*(i)},t))_M = \Re(\mathbf{U}_m^f, m = 1,...,M; \mathbf{X}^{*(i)}) \tag{21}$$

where $\mathbf{U}_m^f$ is the fluid velocity at the m^{th} Eulerian grid node and $\Re$ is a generic interpolation operation. The particle force $\mathbf{f}^{*(i)}$ is then obtained by substituting Eqn.21 in Eqn.20.

ii. Fluid phase governing equations:

The fine particles or dispersed phase are tracked in flow field through granules obtained from particle-resolved DNS methodology called Particle-resolved Uncontaminated-fluid Reconcilable Immersed Boundary Method (PUReIBM). PUReIBM is a Navier-Stokes solver which is spectral in y and z direction and finite difference in x direction, PUReIBM is a numerically convergent and accurate particle-resolved DNS method for gas-solid flows and it has been extensively validated for a comprehensive suite of test cases (Tenneti et al., 2011). The governing equations of the PUReIBM are

$$\frac{\partial u_i}{\partial x_i} = 0 \tag{22}$$

$$\rho_f \frac{\partial u_i}{\partial t} + \rho_f S_i = -g_{IBM,i} + \mu_f \frac{\partial^2 u_i}{\partial x_j \partial x_j} + f_{u,i} \tag{23}$$

Where g_{IBM} is the pressure gradient, S_i is the convective term, $f_{u,i}$ is the immersed boundary force term that accounts for the solid particles in the fluid phase by ensuring zero slip and zero penetration boundary condition at the particle-fluid interface. and ρ_f and μ_f are the thermodynamic density and dynamic viscosity of the fluid-phase respectively. The immersed boundary force is computed only at points lying inside the solid particles. At these points, the fluid velocity field is forced in a manner similar to the ghost cell approach. In addition to the forcing the velocity field, the Immersed boundary forcing term also cancels the remaining terms in the conservation and, at the $(n+1)_{th}$ time-step as given by

$$f_{u,i}^{n+1} = \rho_f \frac{u_i^d - u_i^n}{\Delta t} - \rho_f S_i^n + g_i^n - \mu_f \frac{\partial^2 u_i^n}{\partial x_j \partial x_j} \tag{24}$$

where u_i^d is the desired velocity at that location. The immersed boundary force's effect on the pressure field is obtained by solving a modified pressure Poisson equation given by

$$\mathbf{u}(\mathbf{x},t) = \langle \mathbf{u}(t) \rangle_v + \mathbf{u}'(\mathbf{x},t) \tag{25}$$

In the same way the non-linear term S, pressure gradient g_{IBM} and immersed boundary forcing f_u terms can be decomposed and substituting the decomposed terms in the mass and momentum equations and volume averaging yields the mean momentum conservation equation

$$\rho_f \frac{\partial \langle u_i \rangle_v}{\partial t} = \langle g_{IBM,i} \rangle_v + \langle f_{u,i} \rangle_v \tag{26}$$

The conservation equation for the fluctuating momentum can be obtained by subtracting Eqn.23 from Eqn.20. This is given below

$$\rho_f \frac{\partial u_i'}{\partial t} + \rho_f S_i' = -g'_{IBM,i} + \mu_f \frac{\partial^2 u_i'}{\partial x_j \partial x_j} + f'_{u,i} \tag{27}$$

$$\frac{\partial u_i}{\partial x_i} = 0 \tag{28}$$

Taking divergence of Eqn.27 and using Eqn.28 the modified pressure Poisson equation for the fluctuating pressure gradient can be obtained

$$\frac{\partial g'_{IBM,i}}{\partial x_i} = \frac{\partial f'_{u,i}}{\partial x_i} - \rho_f \frac{\partial S_i'}{\partial x_i} \tag{29}$$

The above given equations are numerically solved to yield the flow field around the granules.

In granular filtration, the fine particles stick on the granules as it flow through the granular bed due to the inertial impaction and interception, which are the filtration mechanisms considered in this study. In order to compute the particles sticking on the granule and also to find the concentration of the fine particles along the granular bed, a statistical description of the particle ensemble is needed over all possible fine particle configurations, fine particle radius and velocities. The statistical description at the single particle level is given by the single-particle distribution function *f*(**x**, **v**, r, t) also known as droplet distribution function in spray literature (Williams, 1958). The *f*(**x**, **v**, r, t) is related to the position, velocity and radius of the physical particles as

$$f(\mathbf{x},\mathbf{v},r,t) = \left\langle f'(\mathbf{x},\mathbf{v},r,t) \right\rangle = \left\langle \sum_{i=1}^{N(t)} f_i'(\mathbf{x},\mathbf{v},r,t) \right\rangle = \left\langle \sum_{i=1}^{N(t)} \delta_{\mathbf{X}^{(i)}} \delta_{\mathbf{V}^{(i)}} \delta_{R^{(i)}} \right\rangle \tag{30}$$

Where, f' is the fine-grained density functions and f_i' is the fine-grained density function for the i[th] particle and the expectation in Eq. 30 is over all possible particle configurations and velocities. The *f*(**x**, **v**, r, t) is an unnormalized density function and integrates to the expected total number of particles and *f*(**x**, **v**, r, t) is evolved as (Subramaniam, 2001, 2000)

$$\frac{\partial f}{\partial x_k} + \frac{\partial}{\partial x_k}(v_k f) + \frac{\partial}{\partial v_k}(\langle A_k \,|\mathbf{x}, \mathbf{v}, r; t\rangle\, f) = f_{source} \tag{31}$$

In Eq. 31 f_{source} is the particle sticking on the granules, and $\langle A_k \,|\mathbf{x}, \mathbf{v}, r; t\rangle$ is the expected acceleration conditional on the location [**x**, **v**, r] in phase space and is defined as

$$\langle A_k \,|\mathbf{x}, \mathbf{v}, r; t\rangle = \frac{1}{f(\mathbf{x}, \mathbf{v}, r, t)} \left[\sum_{i=1}^{N(t)} A_k^{(i)} f_i^{'}(\mathbf{x}, \mathbf{v}, r, t)\right] \tag{32}$$

In this study, only the drag force is needed to model this conditional acceleration term. The particle distribution function can be decomposed as the particle number density n(**x**, r, t), and the a joint probability density function f^C_{VR}(**x**, **v**, r, t) (Subramaniam, 2001)

$$f(\mathbf{x}, \mathbf{v}, r, t) = n(\mathbf{x}, t)\, f^C_{\mathbf{VR}}(\mathbf{v}, r \,|\, \mathbf{x}; t) \tag{33}$$

$$f^C_{\mathbf{VR}}(\mathbf{x}, r \,|\, \mathbf{x}; t) = f^C_{\mathbf{VR}}(\mathbf{v} \,|\, r, \mathbf{x}; t)\; f(r \,|\, \mathbf{x}; t) \tag{34}$$

where $f(r \,|\, \mathbf{x}; t)$ is a continuous size distribution function for the radius of the fine particles. The particle position distribution manifests in the particle number density n(**x**, r, t), which evolves by integrating Eq. 31 over all the velocity spaces (Subramaniam, 2001) as

$$\frac{\partial n(\mathbf{x}, r, t)}{\partial t} + \frac{\partial}{\partial x_k}(\langle V_k n(\mathbf{x}, r, t)\rangle) = S(\mathbf{x}, r, t) \tag{35}$$

The fine particle number density and the particles filtered in the computational domain can also be analytically obtained by solving the number density equation with properly modeling the source term in the right-hand side of Eq 35.

iii. Computational approach

In this DNS approach, fine particles are tracked in Lagrangian frame through a steady velocity field which is obtained from granule-resolved direct numerical simulation of flow through a homogeneous random assembly of granules. In order to obtain the flow fields from PUReIBM through a homogeneous random assembly of granules, first the granules are initialized in a lattice arrangement with a Maxwellian velocity distribution corresponding to a volume fraction of the granules ε_s and then a random equilibrium configuration is attained following an elastic collisions without the presence of the ambient fluid. Then a steady flow is established by imposing a pressure gradient that corresponds to mean flow Reynolds number Re_m that is based on the magnitude of mean slip velocity between the granules and fluid and is defined as

$$Re_m = \frac{|\langle \mathbf{W} \rangle|\,(1-\grave{o}_s)D_g}{\nu_f} \tag{36}$$

where $\langle \mathbf{W} \rangle = \langle \mathbf{u}^{(s)} \rangle - \langle \mathbf{u}^{(f)} \rangle$ is the mean slip velocity between the granule phase and the fluid phase, $\langle \mathbf{u}^{(s)} \rangle$ is mean granules velocity, $\langle \mathbf{u}^{(f)} \rangle$ is mean fluid velocity and D_g is the granule diameter. The mean pressure gradient evolves in time until it attains a value required to drive the desired flow rate.

The single cell models based on simple geometry used for obtaining the flow fields crudely approximate the randomly packed structure of a granular bed and chaotic and complex flow structure. Hence, statistically homogeneous randomly distributed granules in a computational domain with Navier-Stokes equation solved can represent the complex flow structure in a granular bed. To represent a granular bed, a computational domain with homogeneous randomly distributed granules with periodic steady flow field in all three directions, where mean flow is in *x* direction. The computational approach used in this study has mean flow in *x* direction, due to which the fine particles mainly flow in the *x* direction and there is a reduction in the concentration of particles as it flow along *x* direction due to the filtration of the fine particles by the granules. The fine particles are taken to be homogeneously distributed along the *yz* plane due to the absence of any mean flow in *y* and *z* direction.

The simulation is initiated by randomly distributed fine particles homogeneously on the *yz* plane at $x = 0$ with the velocity of the fluid at the initialized random position of the particles. The fine particles are continuously injected into the computational domain on *yz* plane at $x = 0$ and are removed from the simulation at the outlet plane $x = L$, where L is the length of the computational domain. Fig. 18 shows a pictorial representation of the simulation setup. After the initialization of the simulation the fine particles are continuously injected into the computation domain after each computational time step. The simulations are considered to reach steady state, when the filtration rate of the fine particles reach steady state in the domain that is the total filtered fine particles will become constant at each time step.

The boundary conditions for fine particles are inflow and outflow in *x* direction and periodic in the *y* and *z* directions. A fine particle is assumed to be trapped by the granular assembly, when the distance between the center of the granule and the fine particle is less than $(r_p + r_g)$, where the r_p radius of the fine particle and r_g is the radius of the granule.

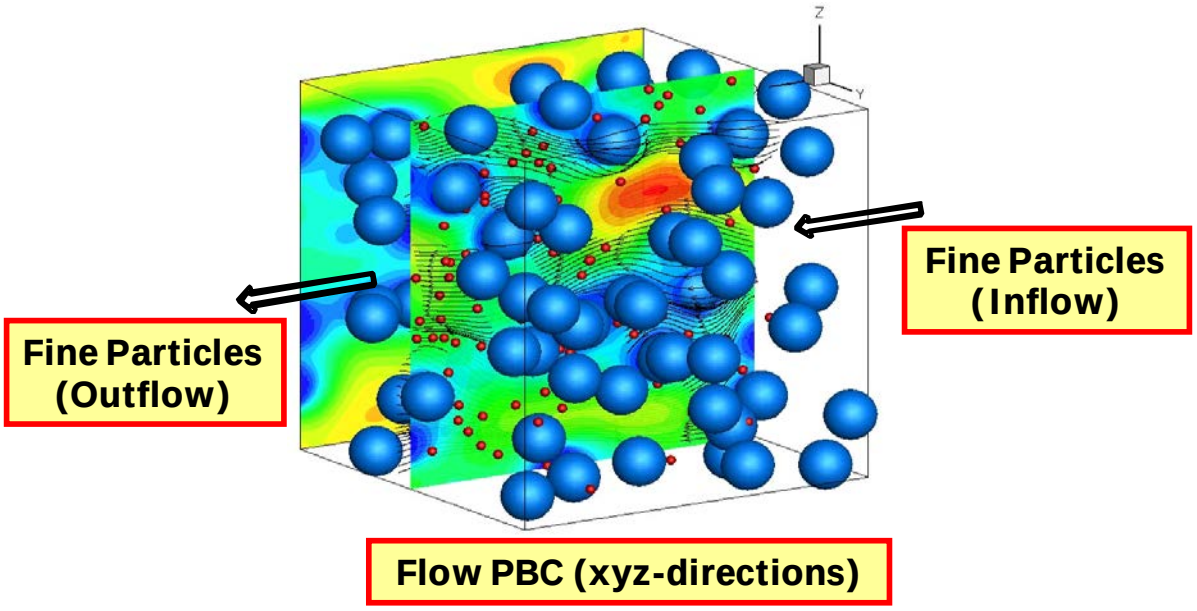

Fig. 18: Trapping of fine particles in a random assembly of granules using DNS. Contours of the streamwise component of velocity are shown for a granule volume fraction of 0.1 and mean slip Reynolds number of 0.01. The Stokes number of the fine particles in this simulation is 4x10-3.

iv. DNS-LPT Results :

1. Study of filtration of particles in a granular bed

To understand the filtration of the fine particles in the granular bed and the effect of the particle Stokes number on it, we studied the filtration of the fine particles in a granular bed using the computational approach discussed in the previous section.

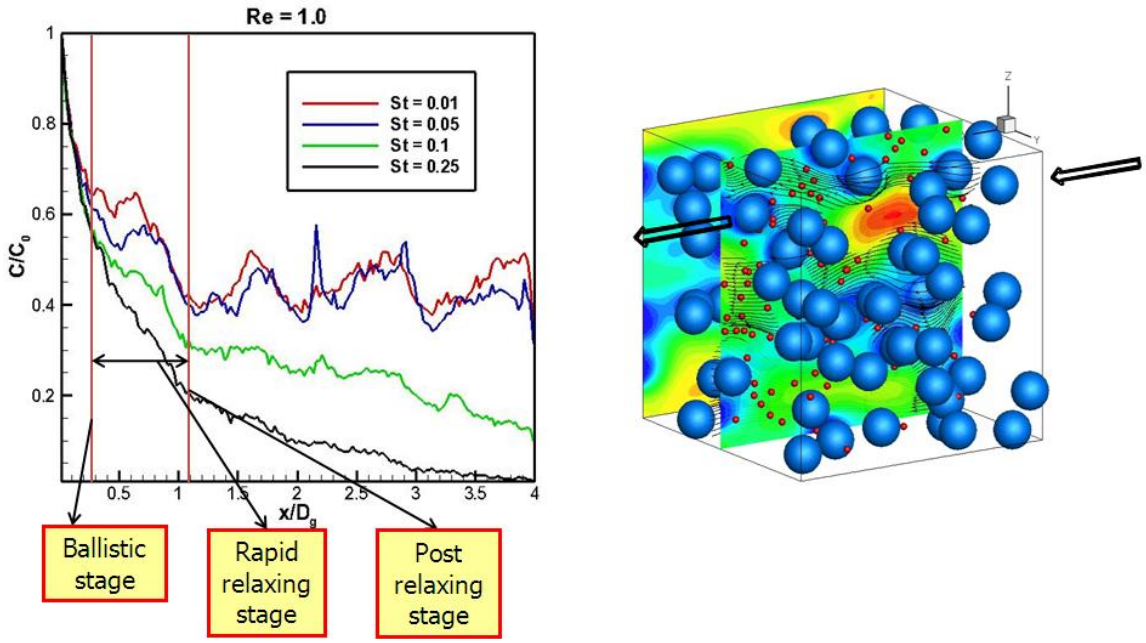

Fig.19: Steady state normalized number density C/C_0 along the flow domain for different Stokes numbers at volume fraction 0.5 and Reynolds number 1.0

The direct numerical simulations provide valuable information concerning the details of the particle trapping or filtration by granules that are not available from correlations or experimental data. Steady state normalized number density C/C_0 of the fine particles along the flow domain for low Reynolds number (*Re=1.0*) is presented in Figure 19. In the case of low Reynolds number flow, the plot of concentration with axial distance (Figure 19) into the bed suggest that there are three stages associated with the trapping of fine particles based on distance from the injection plane. We need to understand these stages as a competition between particle trapping by granules and their ability to escape the granules on fluid streamline by rapidly relaxing of a particle's velocity to the local fluid velocity $\mathbf{u}_f$. In the initial stage (x/D_g <= 0.50), the trapping of the fine particles takes place before their velocities have relaxed to the local fluid velocity for all the Stokes number, which is called the ballistic stage. In the intermediate stage ($0.50 < x/D_g <= 1.0$), the concentration profiles for higher Stokes number (St>= 0.1) drop more rapidly than for the lower Stokes number. This is because of the rapid relaxing of higher Stokes number particles that are unable to follow the fluid streamlines results in increased impaction and interception by the granules. In the final stage ($x/D_g > 1.0$), only the higher Stokes number particles continue to be trapped, while the lower Stokes number particles escape having relaxed onto the fluid streamlines. This manifests as a constant C/C_0 for $x/D_g > 1.0$ for $St < 0.1$ and the final stage is also called post relaxing stage. Note that the particles that are on streamlines sufficiently far from the particle surface will always escape filtration.

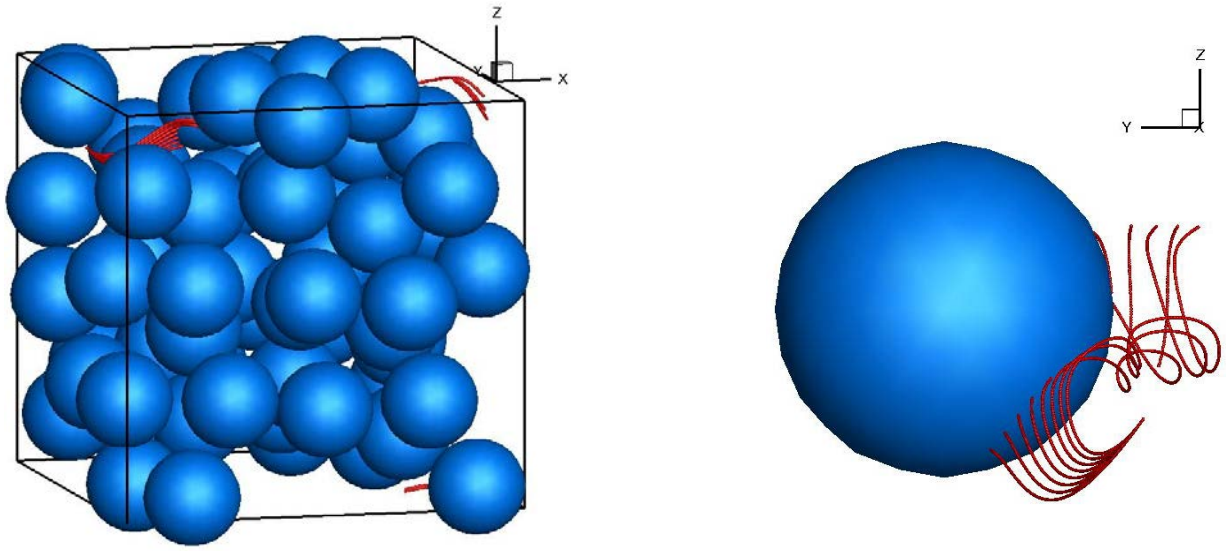

(a) **(b)**

Fig.20: Particles path lines for Stokes numbers 0.01 to 0.25 at volume fractions 0.5 and Reynolds number 1.0 that are initiated the same position on the yz plane. (a) shows the paths of all the fine particles as they travel through the domain and (b) shows the zoomed view in positive x-direction of (a).

To further understand the effect of the Stokes number on the particle trajectory in a random configuration of granules, simulations are done with different fine particle Stokes number initiated on the same fluid streamline. It can be seen in Figure 20 that even with the fine particles with different Stokes number initiated from the same location or on the same fluid streamline, the dispersion length that characterizes the deviation of the particle trajectory from the fluid streamline is different for different particle Stokes number. The relaxing distance of particles to the fluid velocity is proportional to the dispersion length and hence the trapping of these particles takes place at different *x* locations along the computational domain for different particle Stokes number. The more dispersion or deviation from the streamline makes the particles to get deposited on the granule early. The different regimes of filtration can be understood more clearly by seeing the particle pathlines in Figure 20 and observation of the dispersion length which varies with the Stokes number.

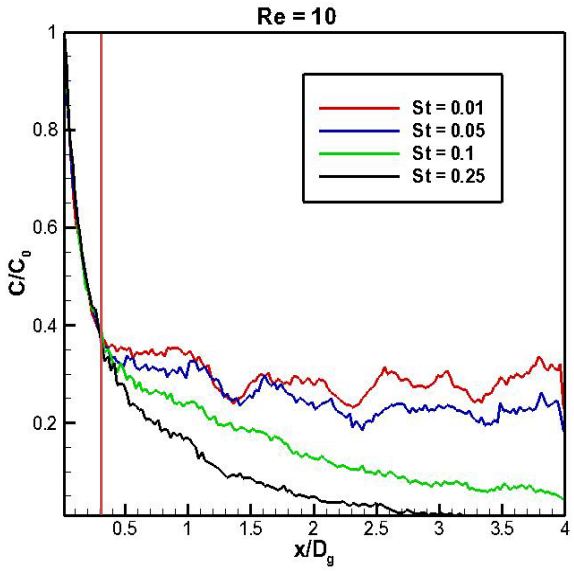

Fig.21: Steady state normalized number density C/C_0 along the flow domain for different Stokes numbers at volume fraction 0.5 and Reynolds number 10

For the case of moderate Reynolds number flow (*Re=10*), the plot of concentration with axial distance into the bed is shown in Figure 21. The DNS results suggest that there are only two stages of particle trajectory at higher *Re* instead of three stages as observed for low Reynolds number associated with the trapping of fine particles. In the first stage, the trapping of fine particles for all Stokes number takes place by $x/D_g < 0.50$ indicating that particle trapping dominates particle relaxation to local fluid velocity due to the ballistic trajectories of the particles and this is more like the combination of first and second stage in *Re=1.0* case. The second stage ($x/D_g < 0.50$) is more like the third stage in the *Re = 1.0* case and only particles with *St>0.1* get trapped due the inertia of higher Stokes number deviates from streamlines and deposit on the granule.

In conclusion, we found from DNS-LPT simulations that fine particles at different stages of granular bed filter at different filtration rates. The interfacial region has higher filtration rate than the downcomer region which was also observed in experimental data (I. El-Hedok 2009). Hence, CFD models should be used with appropriate filtration coefficients in different regions of granular bed.

f. Whether or not the theory and mathematical algorithms were peer reviewed, and, if so, include a summary of theoretical strengths and weaknesses;

N/A

g. Hardware requirements; and

The computing facilities used for running DNS calculations are lightning and Vajra

Lightning: Lightning is an AMD Opteron cluster with 592 processor cores (148 nodes) with each node having 8 GBytes of memory (1182 GB total memory on the cluster). Nodes are interconnected with a high performance InfiniPath HTX communication network for MPI communication and a Gigabit Ethernet switch for I/O, management, and PBS communication. 15 Terabytes of RAID-5 storage are integrated into the cluster.

Lightningsmp: Lightningsmp is an AMD Opteron cluster currently with 512 processor cores (32 nodes) with each node having 64 GBytes of memory (2048 GB total memory on the cluster). Nodes are interconnected with an Infiniband communication network for low latency/high bandwidth MPI communication and a Gigabit Ethernet switch for I/O, management, and PBS communication. Lightningsmp shares fileservers with Lightning for a combined 18.2 TB of RAID-6 storage are integrated into the cluster.

h. Documentation (e.g., user's guide, model code).

N/A